Monte Carlo Simulations for Multicomponent Phase Equilibria and Thermophysical Properties of Near-Critical Fluids

A THESIS
SUBMITTED TO THE FACULTY OF THE GRADUATE SCHOOL
OF THE UNIVERSITY OF MINNESOTA
BY

Ángel David Cortés Morales

IN PARTIAL FULFILLMENT OF THE REQUIREMENTS
FOR THE DEGREE OF
DOCTOR OF PHILOSOPHY

J. Ilja Siepmann

September, 2014

Acknowledgements

First, I would like to express my gratitude towards my advisor, Prof. J. Ilja Siepmann. His encouragement, support, and scientific expertise have been invaluable to my graduate education and to my career. It has truly been an honor to have worked under his guidance.

I owe an immense debt of gratitude to the members of the Siepmann Group for their continuous support over the past five years, which has been invaluable to the progress of my research. I am especially grateful for all the group lunches, game nights, recruiting weekends, BBQ's, and many other events that brought out the best in our group.

I would also like to thank Prof. Ioannis Economou and Dr. Nikolaos Diamantonis, with whom I had the privilege to collaborate with during the past several years. I am very grateful for their hospitality during my visit to Abu Dhabi and for the impact they have made on my professional development.

On a personal note, I would like to express my deepest gratitude to my wife, Verónica Díaz Rodríguez, for her unconditional support and patience these past five years as we worked together towards fulfilling our professional goals. I am also very grateful for my family and friends, old and new, for making my graduate experience outside the research world so much more enjoyable.

Finally, I gratefully acknowledge the National Science Foundation and the Abu Dhabi – Minnesota Institute for Research Excellence (ADMIRE) for their financial support, as well as the Minnesota Supercomputing Institute for providing computing resources.

Abstract

Understanding phase equilibria and thermophysical properties of complex fluid mixtures is crucial to the oil and gas industry, particularly for exploration and production process design. Crude oil and natural gases in such processes are subjected to a very broad range of conditions, under which experimental measurement of physical properties can be quite challenging. To overcome this, the industry has made extensive use of traditional thermodynamic models, such as equations of state and activity coefficient models. However, these conventional tools often lack the necessary predictive power to accurately model fluid properties across the entire range of relevant conditions, especially at extreme conditions where experimental data is often limited. Hence, Monte Carlo simulations have been employed to determine the microscopic features required for improving current PVT modeling methods. Results have shown that these simulations provide remarkably accurate descriptions of phase equilibria and thermophysical properties of fluids relevant to petroleum processing across a wide range of conditions, showing the versatility of molecular simulations as a predictive modeling tool and for developing new modeling methods.

Contents

List of Tables

List of Figures

Chapter 1

Introduction

1.1 Fluid Properties in the Oil and Gas Industry

Although there has been much progress made in identifying and developing alternative energy sources, such as liquid biofuels[1] and photovoltaic solar cells,[2] fossil fuels continue to provide an overwhelming majority of the world's energy supply. Specifically, fossil fuels accounted for 86% of the world's primary energy consumption in 2001,[3] with a roughly equal distribution between oil, coal, and natural gas. Because these fuels are non-renewable, there is great concern regarding the viability of fossil fuels to meet future energy demands, which is undeniably on a rise. The US Energy Information Administration projects that fossil fuels will continue to supply at least 80% of the world's energy usage through 2040.[4] Yet whether the time scale for relying on existing fossil fuel resources is on the order of decades, centuries, or millenias[3] is an enduring topic of debate, particularly with the advent of shale oil and other unconventional oil and gas resources.[5,6] Hence, the majority of oil companies today are focusing on maximizing the recovery factor (RF) from their oilfields, which currently stands somewhere between 20% and 40%.[7] This means that roughly 70% of the original oil in place (OOIP) is left stranded when production ceases and oilfields are abandoned.[8] Advances in enhanced oil recovery (EOR) technologies will be crucial for meeting the demands of our increasingly energy-hungry world, providing additional time to develop alternative energy resources.[3,7] Furthermore, an increase in hydrocarbon fuel consumption inevitably leads to a proportional increase in anthropogenic

carbon dioxide emissions. Thus, developing carbon capture and sequestration (CCS) technologies[9–11] will also play an important role in offsetting greenhouse gas emissions for prolonged fossil fuel usage. In order to develop these promising technologies, it is important to improve our fundamental understanding of the chemical systems at hand.

Crude oil and natural gas are inherently complicated fluid mixtures, typically comprising of a very large number of different chemical components. As such, their fluid properties vary greatly between production and refinery sites, and can be quite challenging to quantify properly. This poses a serious concern for the oil and gas industry because of the wide range of conditions required to process these complicated fluids into desired products, such as gasoline and liquified natural gas (LNG). Understanding fluid properties, such as solubility limits and transport constants, is therefore necessary for designing safe and reliable processes. For example, asphaltene molecules are considered among the largest species found in crude oil and they are known to contribute significantly to the viscosity of bitumen.[12] Despite the current understanding of asphaltene chemistry, their solubility in crude oil still places constraints on petroleum processing because pipeline fouling from asphaltene precipitation continues to compromise flow assurance.[13] Similarly, pipeline blocking is a substantial concern for natural gas production and transport due to formation of ice-like clathrate structures commonly known as gas hydrates[5] . In this case, understanding fluid-hydrate interactions is crucial to control and minimize gas hydrate growth within transmission lines. Hence, there is a need in the oil and gas industry to better understand fluid properties at a fundamental level for a large variety of compounds and processing conditions.

Fluid properties fundamentally influence all three operational sectors of petroleum processing: upstream, midstream, and downstream. The upstream sector is concerned with oil and gas extraction from geologic sources, while midstream and downstream focuses on transporting and refining processes, respectively. Hence, the weight of improving oilfield recovery factors rests largely on technological advances in the upstream sector. Advanced technologies in this sector are largely focused towards miscible and immiscible fluid injection for EOR.[14,15] Recovery strategies, such as water-alternating-gas (WAG)[16] and surfactant/polymer flooding,[17] aim at recovering stranded oil and gas condensates by improving microscopic oil displacements to achieve greater macroscopic sweep efficiencies. Designing EOR processes therefore requires detailed knowledge of fluid PVT properties at relevant reservoir conditions, yet attaining experimental data for this purpose is not always feasible. Despite the large amount of experiments found in the literature, there are many

cases where obtaining experimental measurments for EOR process design is difficult, such as for:[18]

- systems containing substantial amounts of hazardous or corrosive compounds, like hydrogen sulfide
- heavy hydrocarbons that may not be commercially available in pure form for experimental measurements
- system instabilities at relevant temperatures
- systems at extreme pressures

To extend beyond measurement limitations, the oil and gas industry has traditionally made use of classical macroscopic models to extrapolate available experimental data to desired conditions and systems. For thermodynamic properties of fluids, such as phase equilibrium and thermophysical properties, this approach is the industry standard in chemical process design, primarily due to its straightforward integration with traditional process modeling software. Hence, designing efficient recovery processes relies strongly on the use of advanced modeling methods capable of providing reliable representations and predictions of thermodynamic fluid properties. An overview of thermodynamic models commonly employed in the oil and gas industry is provided in the following sections.

1.2 Thermodynamic Models

Expressing thermodynamic properties in terms of analytical expressions has traditionally provided a convenient way of modeling and representing bulk behavior of fluids for many applications. Since Robert Boyle's work on the fluid properties of air in the 17th century, analytical expressions have been progressively developed to represent PVT properties as a representation of microscopic interactions. Many empirical equations of state (EoS) have also been developed for the purpose of correlating known experimental data, and some are often regarded as equivalent to experimental data when applied within valid temperature and pressure limits. For chemical process design, analytically solvable EoS have been frequently used to estimate phase equilibria and PVT properties for common compounds and standard operating conditions. One example is the well-known Span-Wagner EoS,[19–21] an empirical multiparameter model that expresses the specific

Helmholtz free energy as:

$$\frac{a(T,\rho)}{RT} = \frac{a^o(T,\rho)}{RT} + \frac{a^r(T,\rho)}{RT} = \alpha^o(\tau,\delta) + \alpha^r(\tau,\delta) \tag{1.1}$$

where the total free energy is split into ideal and residual contributions, denoted by "o" and "r" superscripts, respectively. Here, R is the gas constant, T is temperature, ρ is density, τ = T_r/T, and δ = ρ/ρ_r. While the ideal component is determined from expressions based on an ideal gas heat capacity correlation, the residual part is parametrized against substance-specific measurements, and takes the form:

$$\alpha^r(\tau,\delta) = \sum_{i=0}^{I_\mathrm{Pol}} n_i \tau^{t_i} \delta^{d_i} + \sum_{i=I_\mathrm{Pol}+1}^{I_\mathrm{Pol}+I_\mathrm{Exp}} n_i \tau^{t_i} \delta^{d_i} \exp(-\gamma_i \delta^{p_i}) \tag{1.2}$$

where the parameters n_i, t_i, p_i, d_i, γ_i, I_Pol, and I_Exp are generated to reproduce multiple sets of experimental data simultaneously. One advantage of this type of formulation is that many thermodynamic properties can be expressed as analytical expressions from first- and second-order derivatives of the reduced Helmholtz free energy. For example, using the thermodynamic relation $u = a - Ts$, the internal energy $u(T,\rho)$ for this EoS is given by:

$$\frac{u(T,\rho)}{RT} = \frac{a + Ts}{RT} = \tau(\alpha^o_\tau + \alpha^r_\tau) \tag{1.3}$$

where

$$\alpha^r_\tau = \left(\frac{\partial \alpha^r}{\partial \tau}\right)_\delta, \alpha^o_\tau = \left(\frac{\partial \alpha^o}{\partial \tau}\right)_\delta \tag{1.4}$$

Based on equation 1.3, the isochoric heat capacity is determined by:

$$\frac{c_v(T,\rho)}{R} = \frac{1}{R}\left(\frac{\partial u}{\partial T}\right)_v = -\tau^2(\alpha^o_{\tau\tau} + \alpha^r_{\tau\tau}) \tag{1.5}$$

where $\alpha^o_{\tau\tau}$ and $\alpha^r_{\tau\tau}$ denote second-order derivatives with respect to τ. Other thermodynamic quantities, such as pressures, enthalpies, and vapor-liquid equilibrium (VLE) properties, can be expressed in a similar manner. Therefore, from a process design perspective, using an empirical EoS such as this one is a convenient choice because its analytical formulation allows for straightforward implementation into process modeling software at a low computational expense. Despite their convenience, empirical models have limited applicability beyond the range of experimental conditions to which they are fitted. For example, activity coefficient models are commonly used to compute thermodynamic properties of liquids at low to moderate temperatures and pressures, yet their accuracy deteriorates as conditions approach the critical point. This limited performance is often due to inaccurate

descriptions of important molecular interactions, particularly as deviations from ideal behavior become more pronounced. Therfore, accurate descriptions of microscopic behavior are necessary to achieve greater applicability.

1.2.1 Cubic Equations of State

One of the most fruitful EoS is the equation proposed by van der Waals in his celebrated thesis in 1873,[22] which was the first to give a satisfactory description of vapor-to-liquid condensation and to predict a critical point.[23] The pressure-explicit form of the van der Waals EoS is expressed as:

$$\left(p + \frac{a}{V^2}\right)(V - b) = RT \tag{1.6}$$

where a is called the attraction parameter and b the effective molecular volume and are given by:

$$\begin{aligned} a &= 3p_cV_c^2 = 27R^2T_c^2/64p_c \\ b &= V_c/3 = RT_c/8p_c \end{aligned} \tag{1.7}$$

where T_c and p_c denote critical temperature and pressure, respectively. This EoS incorporates simple yet fundamental modifications to the ideal gas law, allowing for improved performance due to a better representation of molecular volume exclusion and attractive interactions. Although the universal value of R is used to evaluate the parameters a and b, the van der Waals analysis leads to an expression of the gas constant that is numerically different for each substance, and is given by:

$$R = 8p_cV_c/3T_c \tag{1.8}$$

Equation 1.6 can also be expressed as a third-order polynomial of the compressibility factor z:

$$z^3 - \left(\frac{bp}{RT} + 1\right)z^2 + \frac{ap}{(RT)^2}z - \frac{abp^2}{(RT)^3} = 0 \tag{1.9}$$

This cubic form is convenient from a computing perspective, since its roots can be determined by standard iterative methods, such as the Newton-Raphson method.[24] For VLE calculations, the root finding procedure for a given isotherm yields three real roots for a cubic EoS, the largest interpreted as the vapor compressibility factor, the smallest as the liquid compressibility factor, and the intermediate as physically meaningless. At conditions outside the phase envelope, such as for supercritical fluids, convergence to one root is obtained due to the existence of a single phase.

While the van der Waals EoS, along with his principle of corresponding states, established a precedent for the development of modern cubic EoS, it is now essentially obsolete with the exception of serving as an example of a simple model that incorporates physics-based corrections to the ideal gas law. From a quantitative standpoint, it is seldom better than moderately accurate, whereas other current EoS of not much greater complexity are far superior.[24] Examples of these improved two-parameter cubic EoS include Redlich-Kwong[25] (RK), Soave[26] (SRK), and Peng-Robinson[27] (PR). The SRK and PR EoS are the most popular cubic equations currently used in research and optimizations in which thermodynamic and VLE properties are required.[28] In particular, they have attained wide reception in industry due to their performance in describing phase equilibria for binary and multicomponent systems with little computing effort. In particular, the PR EoS has shown slightly better performance for VLE of non-polar and weakly polar substances at high pressures and, hence, has been used extensively in the oil and gas industry.[29] The PR EoS has the form:

$$p = \frac{RT}{V-b} - \frac{a\alpha(T)}{V(V+b)+b(V-b)} \tag{1.10}$$

where R is the gas constant, a and b are component specific constants that account for attractive intermolecular interactions and hard-core volume of the fluid, respectively, and are calculated as a function of T_{c}, and P_{c}. The constants a and b are given by:

$$\begin{aligned} a =& 0.45724\frac{R^2T_{\mathrm{c}}^2}{p_{\mathrm{c}}} \\ b =& 0.07780\frac{RT_{\mathrm{c}}}{p_{\mathrm{c}}} \end{aligned} \tag{1.11}$$

Moreover, $\alpha(T)$ is a temperature dependent function introduced to provide a better agreement with experimental data from low temperature up to the critical point. This function is component specific, since it includes a function of acentric factor. While significant work has been devoted to developing accurate expressions for $\alpha(T)$ for different types of fluids,[28,30] the original expression proposed by Peng and Robinson is given by:

$$\alpha(T) = [1 + (0.37464 + 1.54226\omega - 0.26992\omega^2)(1 - \sqrt{T_r})]^2 \tag{1.12}$$

For mixture calculations, the standard one-fluid van der Waals mixing rules are often used, given by Equation 1.13. A single temperature independent binary interaction parameter, k_{ij}, can be regressed against experimental data for greater accuracy within fitting boundaries. A non-zero k_{ij} is used for correlating experimental data, whereas setting $k_{\mathrm{ij}} = 0$ provides predictive estimates based on experimental critical properties.

$$\begin{aligned} a\alpha(T) &= \sum_{i=1}^{c}\sum_{j=1}^{c} x_i x_j \sqrt{(a\alpha)_i (a\alpha)_j}(1-k_{ij}) \\ b &= \sum_{i=1}^{c} x_i b_i \end{aligned} \tag{1.13}$$

For VLE calculations, such as in flash calculations at fixed T, p, and overall composition, the PR EoS is most commonly applied in its cubic polynomial form, similar to Equation 1.9. The cubic expression for the PR EoS takes the form:

$$z^3 - (1-B)z^2 + (A - 3B^2 - 2B)z - (AB - B^2 - B^3) = 0 \tag{1.14}$$

where

$$\begin{aligned} A &= a\alpha(T)\frac{p}{R^2T^2} \\ B &= \frac{bp}{RT} \end{aligned} \tag{1.15}$$

At extreme T and p, or in the critical region, activity coefficient models tend to deteriorate due to strong deviations from ideality. This departure yields unreliable flash calculation procedures because activity coefficient models do not account for molecular interactions in the liquid phase properly at these extreme conditions. Instead, the ϕ-ϕ formulation[24] needs to be applied in order to determine partitioning between coexisting phases. Here, phase equilibrium requires that fugacities f_i of all components are equal in both coexisting phases, such that:[31]

$$\begin{aligned} f_i^L &= f_i^V \\ x_i^L \hat{\phi}_i^L &= x_i^V \hat{\phi}_i^V \end{aligned} \tag{1.16}$$

where $\hat{\phi}_i^L$ and $\hat{\phi}_i^V$ denote fugacity coefficients of component i in liquid and vapor phases, respectively, and x_i denotes composition. Partition coefficients (K-values) are therefore directly given by:

$$K_i = \frac{\hat{\phi}_i^L}{\hat{\phi}_i^V} = \frac{x_i^V}{x_i^L} \tag{1.17}$$

The fugacity coefficients for the PR EoS are obtained from the roots of Equation 1.14, and are given by:

$$\ln\hat{\phi}_i = \frac{B_i}{B}(z-1) - \ln(z-B) + \frac{A}{4.828B}\left[\frac{B_i}{B} - \frac{2}{a\alpha(T)}\sum_j x_i (a\alpha(T))_{ij}\right]\ln\left[\frac{z+2.414B}{z-0.414B}\right] \tag{1.18}$$

Hence, by using an objective function, such as the well-known function of Rachford and Rice,[32] K-values can be obtained from an iterative procedure, where convergence yields the compositions of coexisting phases. Moreover, the PR EoS is similarly applicable to calculations involving multiple coexisting phases, such as in VLLE calculations.

For practical purposes, cubic EoS have gained wide reception as a correlation tool for many substances. However, because of the relatively crude description of molecular interactions in these EoS, many physical features are disregarded. For example, hydrogen bonding and strong electrostatic interactions are not explicitly described by PR EoS, making it highly unsuitable for modeling VLE in brines and surfactant mixtures, which are ubiquitous in enhanced oil recovery. Hence, current EoS development has mostly shifted towards models that explicitly account for such physical features.

1.2.2 Molecular-based Equations of State

Describing molecular interactions beyond simple hard sphere repulsion and dispersive attraction has been the major focus of EoS development since the 1980s, providing a greater statistical mechanical basis in molecuar-based models.[33] An EoS that has gained considerable popularity in academic and industrial communities is the statistical associating fluid theory, commonly known as SAFT. It was first developed by Chapman, Gubbins, Radosz, Huang, and co-workers[34,35] based on the thermodynamic perturbation theory (TPT) of Wertheim,[36–39] and has been parametrized for a large number of substances, including aromatic hydrocarbons, polymers, and water. Mathematically, SAFT is expressed as a function of the residual Helmoholtz free energy:

$$\begin{aligned}\frac{A^{res}(T,\rho)}{NRT} = \frac{a^{res}(T,\rho)}{RT} =& \frac{a(T,\rho)}{RT} - \frac{a^{ideal}(T,\rho)}{RT} = \frac{a^{ref}(T,\rho)}{RT} + \frac{a^{disp}(T,\rho)}{RT} \\ =& \frac{a^{hs}(T,\rho)}{RT} + \frac{a^{chain}(T,\rho)}{RT} + \frac{a^{disp}(T,\rho)}{RT} + \frac{a^{assoc}(T,\rho)}{RT}\end{aligned} \tag{1.19}$$

where the superscripts $ideal, ref, disp, hs, chain,$ and $assoc$ denote ideal gas, reference fluid, dispersion, hard sphere, chain formation, and association contributions to the residual Helmholtz free energy. SAFT uses a hard sphere reference fluid, to which perturbations are applied. In contrast to cubic EoS, fugacity coefficients can be derived from the Helmholtz free energy for use in VLE calculations by applying classical thermodynamic relations. This free energy dependence allows the flexibility to improve VLE calculations by modifying the perturbation terms such that additional molecular contributions are accounted for.

The SAFT framework provides a fundamental basis from which numerous EoS have been developed, where the residual free energy terms are modified on the basis of TPT. A popular variation of SAFT is the perturbed-chain SAFT (PC-SAFT[40]), which uses a functional form similar to Equation 1.19, with the exception that thermodynamic perturbations are applied to a hard-chain reference fluid. Hence, the functional form of reference and dispersive perturbation terms differ from the original SAFT formulation. The complete EoS is given in terms of compressibility factors:

$$Z = Z^{id} + Z^{hc} + Z^{disp} + Z^{assoc} \tag{1.20}$$

where the superscript hc denotes the hard chain contribution, $Z = pV/RT$ and $Z^{id} = 1$. Each of these contributions take into account physical features at a molecular level. For example, the perturbation contribution to the compressibility factor for the reference fluid is given by:

$$\begin{aligned} Z^{hc} &= \bar{m} Z^{hs} - \sum_i x_i (m_i - 1) \rho \frac{\partial \ln g_{ii}^{hs}}{\partial \rho} \\ \bar{m} &= \sum_i x_i m_i \end{aligned} \tag{1.21}$$

where x_i is the mole fraction of chains of component i, m_i is the number of segments in a chain of component i, ρ is the total number density of molecules, and g_{ii}^{hs} is the radial pair distribution function (RDF) for segments of component i in the hard sphere system. The hard-chain reference fluid also leads to a dispersion term that better accounts for its dependence on the chain length of a molecule, whereas other SAFT models only account for chainlike shape in the repulsive contribution term. As a consequence, PC-SAFT has shown an improved performance over SAFT for VLE of chain molecules.

The SAFT family has grown significantly since its inception, providing thermodynamic models for a variety of substances by incorporating different molecular contributions within its perturbation terms. For example, the soft-SAFT EoS[41–43] and SAFT-LJ EoS[44,45] both use the Lennard-Jones (LJ) sphere as their reference fluid, where chains are composed of bonded LJ segments which account for both repulsive and attractive interactions of the monomers. The chain perturbation term therefore includes a term for the RDF of LJ segments, as opposed to that of hard spheres in PC-SAFT (see Equation 1.21). Another example is PC-PSAFT,[46,47] an extension of PC-SAFT that was developed to explicitly account for polar and induced polar interactions, such as for quadrupole-quadrupole interactions in CO_2. Many more SAFT variations have now been described in the literature,[48–52]

with variable performance. While the performance in correlating experimental data has been greatly improved over traditional empirical models, predictive thermodynamic modeling using these models is still not sufficiently reliable for most practical applications. Hence, much research is still ongoing to improve predictive modeling capabilities within the framework of molecular-based EoS.

1.3 Molecular Simulations

In contrast to EoS modeling, molecular simulation presents the advantage of a theoretical framework founded upon the priciples of statistical mechanics, where knowledge of explicit interactions at the molecular scale allows for predictive modeling of fluid properties. Advances in simulation algorithms, force fields and computer speed have enabled computer experiments based on molecular simulations that can now predict fluid property data with high precision and accuracy, in some cases more reliably and cost-efficiently than physical experiments.[53] From the perspective of phase equilibria and thermophysical properties, Monte Carlo (MC) simulations provide an alternative for predictive modeling, offering wider range of applicability in comparison to EoS. Moreover, MC simulations yield direct insight into molecular-level details that influence phase equilibria and thermophysical properties, which are much needed to develop advanced EoS. An overview of MC simulation is provided in the following sections.

1.3.1 Metropolis Monte Carlo

Among the Monte Carlo methods available, Metropolis Monte Carlo[54] remains the most widely used technique. To illustrate this method, let's consider the partition function of a system in the canonical (constant N, V, and T) ensemble, which is given by:

$$Q(N,V,T) = \sum_j e^{-E_j/k_\mathrm{B}T} \tag{1.22}$$

where E_j is the energy of the j^{th} eigenstate, and k_B is the Boltzmann constant. We can further consider the system to be composed of N indistinguishable particles, and the summation term can be expressed as a multidimensional integral over the entire set of $3N$ coordinates ($\mathbf{q}^N$) and $3N$ momenta ($\mathbf{p}^N$), that is, over the $6N$ dimensions of phase space. The classical expression for this partition function is given by

$$Q_\mathrm{class} = \frac{c}{N!}\int \cdots \int e^{-H(\mathbf{q}^N,\mathbf{p}^N)/k_\mathrm{B}T}\mathrm{d}\mathbf{p}^N\mathbf{q}^N \tag{1.23}$$

where $H(\mathbf{q}^N, \mathbf{p}^N)$ denotes the classical Hamiltonian $\mathbf{q}^N = q_1, q_2, \cdots, q_N$ is the set of all positions, and $\mathbf{p}^N = p_1, p_2, \cdots, p_N$ is the set of all momenta. The term $1/N!$ is included to account for particles that are indistinguishable, and c is a constant that ensures Q_{class} and Q are equal. Separating the Hamiltonian into kinetic and potential energy (U) terms, and assuming only translational degrees of freedom apply, we obtain

$$H(\mathbf{p}^N, \mathbf{q}^N) = \frac{1}{2m} \sum_{j=1}^{N} \left(p_{xj}^2 + p_{yj}^2 + p_{zj}^2\right) + U\left(\mathbf{q}^N\right) \tag{1.24}$$

By substituting Equation 1.24 into Equation 1.23 and integrating over momenta, we obtain

$$Q_{\text{class}} = \frac{1}{N!} \left(\frac{2\pi m k_{\text{B}} T}{h^2}\right)^{3N/2} Z_N \tag{1.25}$$

where

$$Z_N = \int \cdots \int e^{-U(\mathbf{q}^N)/k_{\text{B}}T} \mathrm{d}\mathbf{q}^N \tag{1.26}$$

is called the configurational integral and $e^{-U(\mathbf{q}^N)/k_{\text{B}}T}$ is known as the Boltzmann weight. With this expression, ensemble averages of mechanical properties M that do not depend on momenta are given by

$$\langle M \rangle = \frac{1}{Z_N} \int \cdots \int M(\mathbf{q}^N) e^{-U(\mathbf{q}^N)/k_{\text{B}}T} \mathrm{d}\mathbf{q}^N \tag{1.27}$$

In general, the goal of a MC simulation is not to evaluate the configuational integral but rather to compute averages of the form given in Equation 1.27. In other words, we are interested in computing the $ratio$ of two multidensional integrals. The Metropolis MC method provides an efficent scheme to sample this ratio based on importance sampling. Here, instead of choosing configurations randomly, then weighing them with exp($-E/kT$), configurations are selected with probability exp($-E/kT$) and weighted evenly.[55] In this way, configurations with a larger Boltzmann weight are selected more frequently, avoiding the need to generate an excessive amount of configurations with low Boltzmann weights. To determine these configurations, a Markov chain of events is generated. In this series of trials, the outcome of each trial depends only upon the trial that immediately precedes it, becoming part of a finite series of outcomes called configurational space.

Trial moves in Metropolis MC are accepted or rejected based on their probability density, which is given by

$$\rho(\mathbf{q}^N) = \frac{e^{-U(\mathbf{q}^N)/k_{\text{B}}T}}{Q} \tag{1.28}$$

The condition of detailed balance requires that, in equilibrium, the average number of accepted trial moves that result in the system leaving state o must be exactly equal to those from all other state n to state o. This condition is given by:

$$K(o \rightarrow n) = K(n \rightarrow o) \tag{1.29}$$

where $K(o \rightarrow n)$ is the flow of configuration o to n and is equal to the product of the probability of being in configuration o, the probability of generating configuration n, and the acceptance probability:

$$K(o \rightarrow n) = \rho(o) \times \alpha(o \rightarrow n) \times \text{acc}(o \rightarrow n) \tag{1.30}$$

From Equation 1.29 it follows that

$$\frac{\text{acc}(o \rightarrow n)}{\text{acc}(n \rightarrow o)} = \frac{\rho(n)}{\rho(o)} = e^{-\beta[U(n)-U(o)]} \tag{1.31}$$

From this expression, the acceptance rule for trial moves is given by:

$$\text{acc}(o \rightarrow n) = \text{min}[1, \frac{\rho(n)}{\rho(o)} \tag{1.32}$$

To decide upon acceptance or rejection of a trial move, a random number r is generated from a uniform distribution within the interval [0,1] and compared to the acceptance probability. Since the probability that r is less than acc$(o \rightarrow n)$ is equal to acc$(o \rightarrow n)$, moves can be accepted if $r <$ acc$(o \rightarrow n)$. A uniform distribution is required for unbiased MC sampling.

1.3.2 Gibbs Ensemble Monte Carlo

Although several molecular simulation methods for the calculation of fluid phase equilibria have emerged over time, the Gibbs ensemble Monte Carlo (GEMC) method introduced by Panagiotopoulos[56,57] shines through conceptual simplicity and has sparked widespread use of molecular simulation for the prediction of fluid phase equilibria. A major advantage of the GEMC method is that it utilizes separate, but thermodynamically connected simulations boxes for the coexisting phases, and avoids the need for explicit interfaces where fluid properties deviate considerably from bulk behavior. For simplicity, we can consider the simulation of vapor-liquid equilibrium (VLE) of neat systems with the canonical version of the Gibbs ensemble, which separates the coexisting phases into two subsystems denoted as boxes 1 and 2. Here, the total number of particles N, total volume V, and temperature

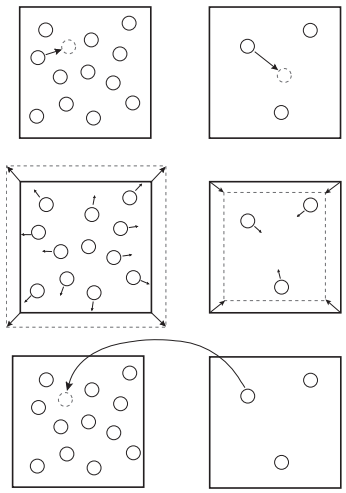

Figure 1.1: Schematic of NVT-Gibbs ensemble moves for two-box setup: particle displacement, volume rearrangement, and particle interchange.[58]

T are maintained constant. Three fundamental move types are used in the Gibbs ensemble: particle displacement, correlated particle insertion/deletion, and correlated volume rearrangements. Figure 1.1 shows these move types for the two-box setup.

By a correlated move we refer to one which upon acceptance has an effect on one box and the opposite effect on the other. For example, if a particle is inserted into box 1, another particle must be deleted in box 2 to maintain N constant. The probability of accepting these moves in the NVT-Gibbs ensemble is founded upon its partition function, which has the form:[58,59]

$$Q(N,V,T) = \int_{V_1=0}^{V} dV_1 \sum_{N_1=0}^{N} Q_1(N_1,V_1,T)\, Q_2(N_2,V_2,T) \tag{1.33}$$

where Q_1 and Q_2 are the canonical partition function for subsystems 1 and 2. Considering the thermodynamic connection between both subsystems (i.e. constraining $N = N_1 + N_2$ and $V = V_1 + V_2$), the partition function can be expressed as

$$\begin{aligned} Q(N,V,T) = \sum_{N_1=0}^{N} \frac{1}{\Lambda^{3N} N_1!(N-N_1)!} \int_0^V \mathrm{d}V_1 V_1^{N_1} (V-V_1)^{N-N_1} \\ \times \int \mathrm{d}\mathbf{s}_1^{N_1} e^{-\beta U(\mathbf{s}_1^{N_1})} \int \mathrm{d}\mathbf{s}_2^{N-N_1} e^{-\beta U(\mathbf{s}_2^{N-N_1})} \end{aligned} \tag{1.34}$$

Here, **s** denotes a scaled coordinate, U denotes potential energy, $\beta = -1/k_{\mathrm{B}}T$, and Λ is the de Broglie thermal wavelength. From this expression it follows that the probability

density of finding some configuration with N_1 particles in box 1 with with a volume V_1 and coordinates $\mathbf{s}_1^{N_1}$ and $\mathbf{s}_2^{N-N_1}$ is given by

$$\rho(N_1, V_1, \mathbf{s}_1^{N_1}, \mathbf{s}_2^{N-N_1}) \propto \frac{V_1^{N_1}(V-V_1)^{N-N_1}}{N_1!(N-N_1)!}\exp\{-\beta[\mathcal{U}(\mathbf{s}_1^{N_1}) + \mathcal{U}(\mathbf{s}_2^{N-N_1}) \tag{1.35}$$

Combining equation 1.35 with the condition of detailed balance form the basis for the acceptance rules of the three main trial moves in GEMC simulations, as explained in the previous section. First, let's consider the particle displacement move. The ratio of statistical weights of these two configurations is given by

$$\frac{\rho(n)}{\rho(o)} = \frac{\exp[-\beta\mathcal{U}(\mathbf{s}_n^{N_1})]}{\exp[-\beta\mathcal{U}(\mathbf{s}_o^{N_1})]} \tag{1.36}$$

Substituting this into the condition of detailed balance yields the acceptance rule

$$\text{acc}(o \to n) = \min[1, \exp\{-\beta[\mathcal{U}(\mathbf{s}_n^{N_1}) - \mathcal{U}(\mathbf{s}_o^{N_1})]\}] \tag{1.37}$$

Now let's consider the volume rearrangement move. Since this move is correlated, when the volume in box 1 is increased by ΔV, the volume in box 2 is decreased by the same amount. The ratio of statistical weights is now given by

$$\frac{\rho(n)}{\rho(o)} = \frac{(V_1^n)^{N_1}(V-V_1^n)^{N-N_1}}{(V_1^o)^{N_1}(V-V_1^o)^{N-N_1}}\frac{\exp[-\beta\mathcal{U}(\mathbf{s}_n^N)]}{\exp[-\beta\mathcal{U}(\mathbf{s}_o^N)]} \tag{1.38}$$

In accordance to the condition of detailed balance, the acceptance rule for volume change is given by

$$\text{acc}(o \to n) = \min\left[1, \frac{(V_1^n)^{N_1}(V-V_1^n)^{N-N_1}}{(V_1^o)^{N_1}(V-V_1^o)^{N-N_1}}\exp\{-\beta[\mathcal{U}(\mathbf{s}_n^N) - \mathcal{U}(\mathbf{s}_o^N)]\}\right] \tag{1.39}$$

Now let's consider a particle insertion into box 1. Upon acceptance of this move, an analogous particle deletion must occur in box 2 so as to maintain the total number of particles N constant. The ratio of statistical weights of the configurations is then given by

$$\frac{\rho(n)}{\rho(o)} = \frac{N_1!(N-N_1)!V_1^{N_1}(V-V_1)^{N-(N_1-1)}}{(N_1-1)!(N-(N_1-1))!V_1^{N_1}(V-V_1)^{N-N_1}}\exp\{-\beta[\mathcal{U}(\mathbf{s}_n^N) - \mathcal{U}(\mathbf{s}_o^N)]\} \tag{1.40}$$

Once more, by imposing detailed balance for this move yields the acceptance rule:

$$\text{acc}(o \to n) = \min\left[1, \frac{N_1(V-V_1)}{(N-N_1+1)V_1}\exp\{-\beta[\mathcal{U}(\mathbf{s}_n^N) - \mathcal{U}(\mathbf{s}_o^N)]\}\right] \tag{1.41}$$

This set of moves is required for all GEMC simulations. Particle displacement moves are necessary to ensure that the system has reached thermal equilibrium. Likewise, volume

moves ensure that the pressure is equilibrated between both boxes, reaching mechanical equilibrium. Particle insertion/deletion moves are likewise necessary to equilibrate the chemical potential and establish chemical equilibrium. On his original derivation, Panagiotopolous considered the Gibbs ensemble as a combination of various other ensembles. The particle displacement moves considered a system in the NVT ensemble, the volume rearrangements considered the system to be in the NpT ensemble, and the particle insertion/deletion moves considered the system to be in the μVT ensemble. While the derivation based on these assumptions paved the way for the currently accepted method, a system cannot be in multiple ensembles at the same time.

The GEMC method has been illustrated for simple molecules without any consideration for internal degrees of freedom, such as bond bending and bond stretching. However, these important molecular features must not be overlooked, as they strongly influence fluid properties and are widely incorporated into most molecular mechanics force fields.

1.3.3 Configurational-Bias Monte Carlo

The standard move types detailed in the previous sections have shown to be useful by themselves for relatively simple systems. As one moves to more complex systems, such as chain molecules, their performance are not enough to ensure efficient simulation of phase equilibria. For example, particle insertions into a dense system in the Gibbs ensemble are likely to encounter particle overlap for chain molecules, as their conformation in space is not being altered during a standard insertion/deletion move. Considering a chain molecule to be modeled as a chain of beads, the probability of inserting a bead into a liquid box of common density is close to 1 in 200. Extending this to chains of n beads leads to probabilities of insertion in the order of 1 in 200^n. This would make many ordinary simulations, such as for VLE of conformationally flexible alkanes, essentially impossible and would require excessively large amounts of computer time. For this reason, incorporating configurational-bias Monte Carlo[60–62] (CBMC) moves into such simulations has a huge influence on these acceptance rates.

The CBMC algorithm was derived as an extension of the self-avoiding random walk scheme of Rosenbluth and Rosenbluth[63] for the simulation of polymers on a lattice. This method is built up in a stepwise manner such that, at every stage, the next monomeric unit or bead is preferentially added in a direction that has a large Boltzmann weight (more

favorable configurations) in contrast to those with low Boltzmann weights (unfavorable conformations, i.e. overlaps). Before a bead is inserted, the Boltzmann weight for each of the generated trial sites is computed, allowing the system to sample various possible conformations.

When using CBMC moves in a simulation, it is often convenient to separate the potential energy into two parts, the bonded (internal) potential (U^{int}) and the non-bonded (external) potential (U^{ext}). The bonded potential is necessary to generate possible trial sites, since accounting for the molecular mechanics of torsions, bends, and stretches influences where new sites can be generated. The non-bonded potential, however, influences which of these trial sites is most energetically favorable, hence allowing the molecules to be grown with greater energetic "comfort". Note that this process takes into account the regrowth of one monomeric unit or bead at a time. This means that, without further modification, this algorithm would spend a considerable amount of computer time on "dead end" configurations for large or heavily branched molecules, though not as much as without it. Hence, this method works best when tuned to the specific needs of the simulation or application of interest.

To explore this method in detail, let's consider a molecule to be regrown into a new configuration in a step-by-step manner. If the entire molecule is being regrown, then f trial sites are generated at random positions within the simulation box, where one of these (site i) is chosen with probability of

$$P_{1i}^{\mathrm{selecting}}(\mathbf{b}_i) = \frac{e^{-\beta U_{1i}^{\mathrm{ext}}}}{w_1(n)} \tag{1.42}$$

where

$$w_1(\mathrm{n}) = \sum_{j=1}^{f} e^{-\beta U_{1j}^{\mathrm{ext}}} \tag{1.43}$$

Equation 1.43 is the Rosenbluth weight of the first segment in the new configuration. For the remainder of the l segments, k trial orientations $\mathbf{b}_{\mathrm{i}}$ are generated and the molecule can be regrown according to the Boltzmann weight of the internal potential for each segment:

$$P_{li}^{\mathrm{generating}}(\mathbf{b}_i)\mathrm{d}\mathbf{b} = \frac{e^{-\beta U_{li}^{\mathrm{int}}}\mathrm{d}\mathbf{b}}{\int e^{-\beta U_{l}^{\mathrm{int}}}\mathrm{d}\mathbf{b}} = Ce^{-\beta U_{li}^{\mathrm{int}}}\mathrm{d}\mathbf{b} \tag{1.44}$$

where C is just an integration constant. From the k trial orientations that were generated, one is chosen according to the Boltzmann weight of its external potential

$$P_{li}^{\mathrm{selecting}}(\mathbf{b}_i) = \frac{e^{-\beta U_{li}^{\mathrm{ext}}}}{w_l(\mathrm{n})} \tag{1.45}$$

where again the denominator on the right hand side denotes the Rosenbluth weight of segment l. This procedure is repeated until the entire molecule has been grown. The Rosenbluth weight for all s segments in the new configuration is given by

$$W(\mathrm{n}) = \prod_{l=1}^{s} w_l(\mathrm{n}) \tag{1.46}$$

The probability of growing the new chain is given by the product of the probability of generating a trial orientation and the probability of selecting this orientation. For all monomers or beads, this gives

$$P(\mathrm{n}) = \prod_{l=1}^{s} P_{li}^{\mathrm{selecting}} P_{li}^{\mathrm{generating}} \tag{1.47}$$

Here, i denotes the specific trial site that was selected for growth. Substituting equations 1.44 and 1.45 and considering that $U = U^{\mathrm{ext}} + U^{\mathrm{int}}$ yields

$$P(\mathrm{n}) = \prod_{l=1}^{s} \frac{Ce^{-\beta U(\mathrm{n})}}{w_l(\mathrm{n})} \tag{1.48}$$

Having established how to grow a molecule into a new conformation, we now turn to the rules governing the acceptance of these moves during simulation. To do so will require calculating the Rosenbluth weight of the old configuration in order to consequently accept or reject this move. This old configuration is retraced in a similar fashion, except that now $f-1$ trial orientations are generated for the first monomer or bead, and $k-1$ for all other segments. The f^{th} and k^{th} orientations represent the analogous old configurations. For the first monomer or bead, the Rosenbluth weight of the old configuration is given by

$$w_1(\mathrm{o}) = \sum_{j=1}^{f-1} e^{\beta U_{1j}^{\mathrm{ext}}} + e^{-\beta U_{1f}^{\mathrm{ext}}} \tag{1.49}$$

where $e^{-\beta U_{1f}^{\mathrm{ext}}}$ is the current external potential being weighted against the other $f-1$ generated orientations. Hence, the probability of this site being selected to grow the first bead or monomer is given by

$$P_{1f}^{\mathrm{selecting}}(\mathbf{b}_f) = \frac{e^{-\beta U_{1f}^{\mathrm{ext}}}}{w_1(\mathrm{o})} \tag{1.50}$$

Likewise, k^{th} (old) orientation is weighted against the other $k-1$ trial orientations generated for the rest of the segments in the chain, and thus the probability that this old configuration would be chosen is given by

$$P_{lk}^{\mathrm{generating}}(\mathbf{b}_k)\mathrm{d}\mathbf{b} = \frac{e^{-\beta U_{lk}^{\mathrm{int}}}\mathrm{d}\mathbf{b}}{\int e^{-\beta U_{l}^{\mathrm{int}}}\mathrm{d}\mathbf{b}} = Ce^{-\beta U_{lk}^{\mathrm{int}}}\mathrm{d}\mathbf{b} \tag{1.51}$$

Similar to the new trial configurations, the probability of selecting each of the k^{th} segment in the old configurations is given by

$$P_{lk}^{\text{selecting}}(\mathbf{b}_k) = \frac{e^{-\beta U_{lk}^{\text{ext}}}}{w_l(o)} \tag{1.52}$$

where, analogous to equation 1.49, the Rosenbluth weight for the l^{th} segment is given by

$$w_l(\text{o}) = \sum_{j=1}^{k-1} e^{\beta U_{lj}^{\text{ext}}} + e^{-\beta U_{lk}^{\text{ext}}} \tag{1.53}$$

and again the last term is the current external potential being weighted agains the other $k-1$ generated orientations. Having this we can determine the Rosenbluth weight for the old configuration of the entire molecule or chain, given by

$$W(\text{o}) = \prod_{l=1}^{s} w_l(\text{o}) \tag{1.54}$$

The overall probability of growing the old molecule or chain is therefore given by

$$P(\text{o}) = \prod_{l=1}^{s} P_{lk}^{\text{selecting}} P_{lk}^{\text{generating}} \tag{1.55}$$

Inserting the previously determined expressions for $P_{lk}^{\text{selecting}}$ and $P_{lk}^{\text{generating}}$ into equation 1.55, and again taking into account that $U = U^{\text{ext}} + U^{\text{int}}$, the expression for $P(\text{o})$ reduces to

$$P(\text{o}) = \prod_{l=1}^{s} \frac{C e^{-\beta U(\text{o})}}{w_l(\text{o})} \tag{1.56}$$

In going from the old configuration to the new one, it follows from equation 1.30 that

$$K(\text{o} \to \text{n}) = \frac{e^{-\beta U(\text{o})}}{Q} \frac{C e^{-\beta U(\text{n})}}{w_l(\text{n})} \text{acc}(\text{o} \to \text{n}) \tag{1.57}$$

In order to maintain the detailed balance condition, equation 1.29 must apply. Therefore, it follows that

$$\frac{K(\text{o} \to \text{n})}{K(\text{n} \to \text{o})} = \frac{\text{acc}(\text{o} \to \text{n})\ w_l(\text{o})}{\text{acc}(\text{n} \to \text{o})\ w_l(\text{n})} = 1 \tag{1.58}$$

We can now determine the corresponding acceptance probabilities without any prior knowledge of the partition function nor the integration constant, which in practice is highly favorable. The probability that the trial configuration is accepted for the new segment is given by

$$\text{acc}(\text{o} \to \text{n}) = \text{min}\left\{1, \frac{w_l(\text{n})}{w_l(\text{o})}\right\} \tag{1.59}$$

Similarly, the acceptance probability for the whole chain or molecule is obtain by taking the product over all segments:

$$\text{acc}(\text{o} \rightarrow \text{n}) = \prod_{l=1}^{s} \text{min}\left\{1, \frac{w_l(\text{n})}{w_l(\text{o})}\right\} = \text{min}\left\{1, \frac{W(\text{n})}{W(\text{o})}\right\} \tag{1.60}$$

Incorporating CBMC into a GEMC simulation greatly improves its performance and allows one to efficiently simulate systems with conformational degrees of freedom. This is particularly important for challenging simulations of dense systems, such as those shown in Chapters 5 and 6 where long-chain alkanes require many insertions into dense liquid phases. Morever, efficient simulation is necessary for systems that require long equilibration periods or can potentially become trapped in metastable states. With these tools at hand, a variety of complex chemical systems can be explored. In the following chapters, these advanced modeling strategies were used to determine phase equilibria and thermophysical properties for a variety of fluid systems.

Chapter 2

Influence of Simulation Protocols on the Efficiency of Gibbs Ensemble Monte Carlo Simulations

2.1 Introduction

As explained in Section 1.3.2, GEMC simulations provide an elegant formalism to directly compute VLE properties. However, simulations of challenging systems often require additional considerations by the user. For example, VLE of near-critical systems suffer from density fluctuations as the coexisting phases become increasingly similar, often rendering the simulations unstable. As shown in Chapters 3, 4, and 5, large system sizes are introduced at the expense of increased computational effort to supress fluctuations. For such cases, it is highly desirable to reduce the expense by selecting simulation protocols that yield efficient computational performance. Therefore, it is necessary to assess computing expenses within GEMC simulations.

The computational effort for particle swap and volume moves is considerably greater than for conventional particle displacements. The volume move is intrinsically expensive because, for molecules represented by multi-site models, it involves the calculation of the total energy of each subsystem, whereas only the energy of the displaced particle is required for translational and rotational moves. The effort for a particle swap move is large because special tricks are needed to achieve a reasonable acceptance rate at low reduced temperature and/or for complex molecules with conformational flexibility or the ability to

form hydrogen bonds. Configurational-bias Monte Carlo strategies can greatly boost the acceptance rates for particle swap moves[61,62,64–66] but are more expensive than unbiased particle swap moves.

Given that the GEMC partition function involves an outer integration over volume and summation over particle number with the inner terms being a product of canonical partition functions for the two subsystems (see Equation 1.33), it is not clear how the computational effort should be distributed between volume and swap moves necessary for the sampling of the outer integration/summation and particle displacement moves necessary for the sampling of the microstates within the canonical terms. For systems with the interactions described by molecular mechanics force fields, the cost of an energy calculation depends mostly on the number of particles in a given subsystem and the fraction of particles contained within the potential truncation distance. Thus, the cost of computing the liquid-phase energy is much higher than that for the vapor phase. Given the constraint that the box length for each subsystem should be larger than twice the distance used to truncate molecular mechanics interactions, the smallest overall system size for a GEMC simulation can be achieved by distributing the volume about evenly between the vapor and liquid phases; a set-up used by most early GEMC simulations.[53,57,59,67] (This also holds for recent GEMC simulations using Kohn-Sham density functional theory with a plane wave basis set to describe the intermolecular interactions because empty space in the vapor phase also contributes significantly to the cost.[68]) At low reduced temperatures and for typical system sizes, however, a phase ratio near unity results in a vapor phase containing on average less than one particle which leads to large statistical uncertainties for the determination of the saturated vapor density and pressure. Thus, more recent Gibbs ensemble simulations[66,69] have used a larger total volume to shift the phase ratio toward the vapor side, so that a suitable number of particles is found on average in the vapor phase.

For a GEMC simulation of a specific single-component system (N molecules of a given type) at a specific state point (temperature T), the user needs to specify the frequencies with which particle swap and volume moves are attempted and the total volume that controls the phase ratio. Judicious choices of these simulation parameters may lead to improved computational efficiency for a GEMC simulation. Different research groups have over time used rather different protocols,[53,66,67,69–71] In this work, several simulation protocols are explored covering the range of GEMC simulation parameters commonly used. Specifically, the total volumes were adjusted to yield either about equal volumes for both

phases or a phase ratio with the vapor phase containing about 10 or 20% of the total particles (these three phase ratios are labeled here as `EQ`, `10`, and `20`) and the frequencies for attempted special moves were adjusted to yield about 0.1, 1, and 10 accepted swap and volume moves per MC cycle consisting of N randomly selected moves (these three move frequencies are labeled here as `Lo`, `Me`, and `Hi`.

To assess whether different molecule types would benefit from different protocols, simulations were carried out for water and n-octane, i.e., prototypical examples of hydrogen-bonding and articulated molecules. In addition, three different reduced temperatures ranging from near the triple point to near the critical point were investigated. The computational efficiency is measured by the relative standard error of the mean for the orthobaric liquid density and saturated vapor pressure achieved for a given amount of CPU time. Comparison of the large number of simulations provides guidance on suitable simulation protocols for GEMC simulations. It should be noted here that other advanced Monte Carlo approaches for the determination of coexistence curves also require setting a large number of control parameters governing the efficiency and a comparison to recent transition matrix Monte Carlo simulations[72] is beyond the scope of this work.

2.2 Simulation Details

The interactions of n-octane and water were described by the TraPPE–UA force field[69] and the TIP4P model,[73] respectively. For the alkane, the Lennard-Jones potential is used for the nonbonded interactions of CH_x pseudo-atoms and the intramolecular degrees of freedom are governed by a fixed C–C bond length, a harmonic angle bending potential, and a cosine series torsional potential. The TIP4P model uses a rigid internal structure and the nonbonded interactions are described by a combination of Lennard-Jones and Coulomb potentials.

The MCCCS–MN program[74] was used for all NVT-GEMC simulations. For both compounds, simulation were carried out at three reduced temperatures: 0.6, 0.75, and 0.9 (with the values of $T_{\mathrm{c}} =$ 568 K for n-octane and 583 K for water taken from previous simulations[69,75]). System sizes of 200 and 500 molecules (i.e., 1600 and 2000 interactions sites, respectively) were used for the n-octane and water simulations, respectively. These systems sizes are typical for these two compounds and allow for use of potential truncation distances consistent with those used in the force field development. In the n-octane simulations with the TraPPE force field, a spherical potential truncation with $r_{\mathrm{cut}} =$ 1.4 nm

and analytical tail corrections[54] was used for the nonbonded Lennard-Jones interactions. For the TIP4P water simulations, the Lennard-Jones and Coulomb interactions in the liquid phase were truncated at 1.0 nm, whereas a larger truncation distance close to 40% of the average box length was used for the vapor phase, and analytical tail corrections for the Lennard-Jones interactions and an Ewald summation with the convergence parameter set at $3.2/r_{\mathrm{cut}}$ were employed to account for the long-range interactions.[54] When the Ewald method is used, then adjusting r_{cut} to reflect the box length greatly reduces the number of reciprocal space vectors and leads to a reduction in the computational effort.[76]

As mentioned in Section 2.1, three different phase ratios (`Eq`, `10`, and `20`) and three different sets of swap and volume move frequencies (`Lo`, `Me`, and `Hi`) were explored. However, an upper bound of 50% was applied for the fraction, f_{swap}, of particle swap moves to ensure an adequate fraction of the conventional moves. Since acceptance rates for particle swaps can become extremely low at low reduced temperatures and for large molecules, this upper bound restricted the use of the simulations protocols with the higher acceptance frequencies. The remaining fraction of MC moves was divided equally among translational and rotational moves for water and among translational, rotational, and CBMC conformational moves for n-octane. Maximum displacements for translational and rotational moves were adjusted to yield acceptance probabilities close to 50%. The CBMC parameters for insertion of the first bead (the oxygen site and a methyl group for water and n-octane, respectively) in a swap move and for subsequent beads in swap and conformational moves were set to 10 and 8 for n-octane and 32 and 8 for water. Given the adjustable maximum volume displacement (set to yield an acceptance rate of 40%), the fraction of volume moves required for a specific number, N_V, of accepted volume moves per cycle is given by $f_{\mathrm{vol}} = N_V/0.4N$. In these GEMC simulations, the instantaneous pressure is evaluated only after every five MC cycles (because of the expense of the pressure calculation), whereas the instantaneous density is known at every MC step. The short names of the GEMC simulation protocols and the numerical values for their control parameters are summarized in Table 2.1.

To provide reliable estimates of the statistical uncertainties, 16 independent simulations were performed for every setup that was tested, where the production period in each of these consisted of 2.5×10^5 MC cycles. The relative standard error of the mean for vapor pressures and liquid densities were computed to assess the efficiency of each simulation protocol. Values of the running averages were stored every 2500 MC cycles, yielding 100 evenly-spaced data points from which the standard error of the mean, σ_{m}, can be

Table 2.1: Total volume and fraction of swap moves for different GEMC protocols.

		V [nm^3]			f_{swap} [%]		
T_{r}	compound	Eq	10	20	Lo	Me	Hi
0.60	water	31	3800	7500	1.3	13	—
	n-octane	110	4200	8300	25	—	—
0.75	water	35	280	530	0.45	4.5	45
	n-octane	130	460	860	1.5	15	—
0.90	water	42	52	83	0.25	2.5	25
	n-octane	140	150	230	0.33	3.3	33

computed. At any point p along the progress of the $n = 16$ independent simulations, σ_{m} of a particular property can be computed as follows

$$\sigma_{\mathrm{m}}(p) = \left\{ \frac{1}{n(n-1)} \sum_{i=1}^{n} \left[x_i(p) - \overline{x(p)} \right]^2 \right\}^{1/2} \tag{2.1}$$

where $x_i(p)$ is the running average of independent simulation i at point p, and $\overline{x(p)}$ is the mean of the running averages over all independent simulations at point p.

To allow for comparison of different GEMC simulation protocols that require different amounts of computational effort per MC cycle, the evolution of the relative standard error of the mean is plotted here as function of the total CPU time, $t_{\mathrm{CPU}}(p)$ (on four quad-core 2.66 GHz Intel Xeon processors), for all 16 independent simulations. The efficiency of a protocol is then given by the term A determined from a least-squares fit to a log-log plot as follows

$$\log \left[\sigma_{\mathrm{m}}(p) / \overline{x(p)} \right] = \log A - 0.5 \log \left[t_{\mathrm{CPU}}(p) \right] \tag{2.2}$$

The relative efficiency, R_{eff}, of two simulation protocols α and β is given by

$$R_{\mathrm{eff}} = \left(A_\alpha / A_\beta \right)^{-2} \tag{2.3}$$

That is, when, for a given amount of CPU time, protocol α yields a σ_{m} that is three times smaller than for protocol β, then protocol α is nine times as efficient because it would take nine times longer for protocol β to reach the same lower value of σ_{rm}. Here, R_{eff} is given with respect to the most efficient protocol for a given property, compound, and reduced temperature.

2.3 Results and Discussion

2.3.1 Verification and Precision of Simulation Protocols

While assessing the efficiency of different simulation protocols is key to this work, it is also important to verify that these protocols yield the correct answer. For any protocol at a given state point, all independent simulations are expected to converge to the same value within statistical uncertainty. Figure 2.1 shows the convergent nature of the n-octane and water simulations carried out at $T_\mathrm{r} = 0.75$ using one of the protocols (`20-Me`). After about 200 total CPU hours (i.e., about 12 CPU hours per independent simulation), the spreads among the different simulations have reduced to about 0.004 and 0.01 g/ml for the liquid densities of n-octane and water, respectively, and to about 20 and 100 kPa for the saturated vapor pressures of n-octane and water, respectively. Accounting for the differences in the absolute values of these properties, the relative deviations are quite similar for the two compounds despite the larger system size used for water. For the compounds and system sizes used here, a single simulation run lasting for about 12 CPU hours yields a liquid density and saturated vapor pressure that should fall within about 1% and 10% of the mean values that would be obtained using longer runs and/or multiple independent simulations.

Figure 2.2 illustrates the convergence of the mean values obtained by averaging over the 16 independent simulations. It is evident that the different simulation protocols converge to the same mean values. As should be expected, the spread between these mean values is about a factor of 4 smaller than the spread between the independent simulations. After a total of 200 CPU hours, the spread is only about 0.001 g/ml (0.2%) and 5 kPa (2%) for the liquid density and saturated vapor pressure of n-octane. Spreads of this (relative) magnitude are already much smaller than the accuracy of almost all molecular mechanics force fields. To investigate whether the lower frequency of the pressure calculation causes its larger relative error, the evolution of the vapor density was also assessed (not shown). However, it was found that the relative spread for the mean values of the vapor density yields values that are very close to those for the vapor pressure; hence, the lower frequency of the pressure calculation is not responsible for the larger spread in the vapor-phase properties.

The data presented so far illustrate that (i) independent simulations with the same simulation protocol converge to the same property values and (ii) the simulations for the different protocols converge to the same property values. However, neither of these tests rules out mistakes in the simulation algorithm and its implementation into a computer program

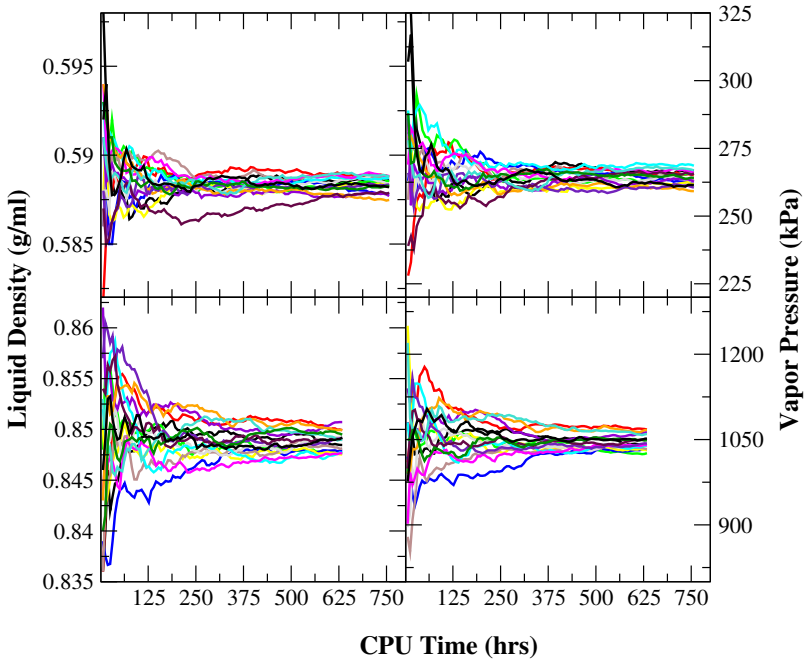

Figure 2.1: Running averages of the liquid densities (left) and vapor pressures (right) for n-octane (top) and water (bottom) obtained for 16 independent simulations as function of CPU time at $T_\mathrm{r} = 0.75$ using protocol `20-Me`.

because such mistakes might lead to reproducible and converging but incorrect property values. To check for the correctness of the simulation algorithm and its implementation, the present simulation data are compared with literature data.[69,72,77,78] As can be seen from the data presented in Figures 2.3 and 2.4, the coexistence densities and saturated vapour pressures obtained for protocol 10–Lo (available at all three state points) are in excellent agreement with other simulations using the transition matrix MC method,[72] the reaction GEMC method,[78] and molecular dynamics simulations for a liquid slab with explicit interfaces.[77]

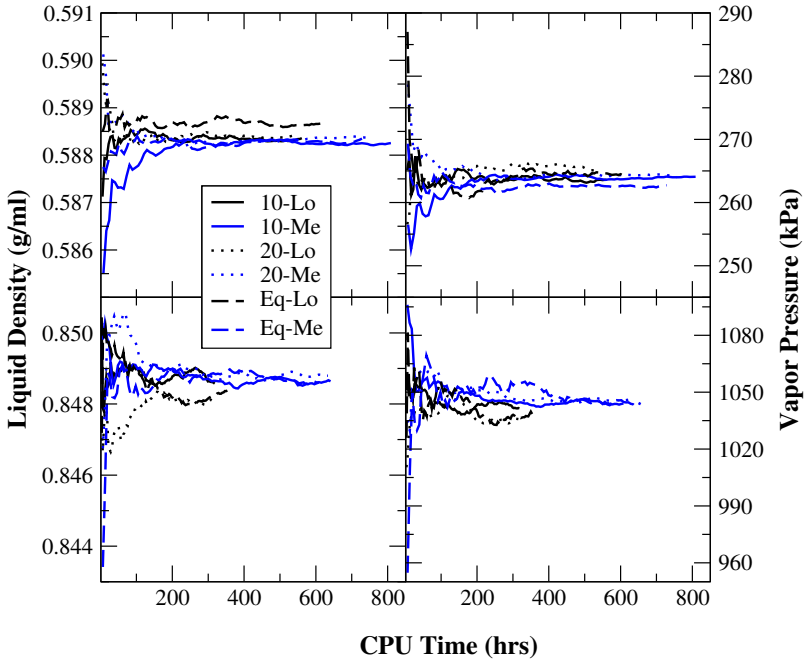

Figure 2.2: Mean values of the liquid densities (left) and vapor pressures (right) for n-octane (top) and water (bottom) obtained by averaging over the 16 independent simulations for each protocol as function of CPU time. Results are shown for six different protocols at $T_{\mathrm{r}} = 0.75$.

2.3.2 Effects of Phase Ratio and Frequency of Accepted Swap and Volume Moves

Here it needs to be mentioned again that the acceptance rate for swap moves decreases significantly as the temperature is decreased. With the CBMC parameters used in this work, the decrease is much more severe for n-octane (close to a factor of 5 as T_{r} is lowered from 0.9 to 0.75) than for water (only about a factor of 2 for the same change in T_{r}). Thus, protocols yielding the higher acceptance frequencies cannot be achieved at the lower temperatures (see Table 2.1).

Figures 2.5 and 2.6 show the evolution of the relative standard error of the mean for the liquid density and the vapor pressure, respectively, and Table 2.2 provides numerical values for the relative efficiencies of the different protocols. Although the log-log plots indicate that

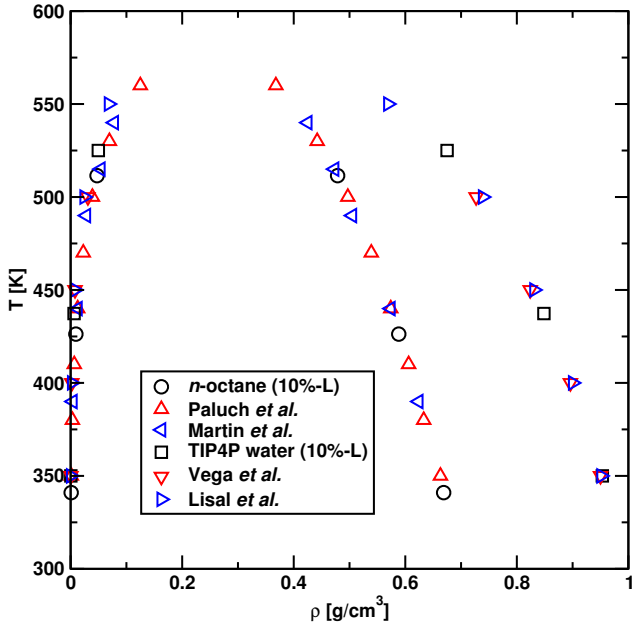

Figure 2.3: Vapor–liquid coexistence curves for n-octane and water showing a comparison of data obtained for protocol 10–Lo with previous simulation data for the same models.[69,72,77,78]

the present simulations follow the expected decrease in the relative $\sigma_{\rm m}$ as the CPU time increases and yield a slope close to –0.5 in all cases, the noise in the data is pronounced and the decrease is non-monotonic. Thus, the precision of the uncertainty estimate is low (using 16 independent simulations). In contrast, the precision of the vapor–liquid coexistence data is very high. For GEMC simulations taking approximately 1000 CPU hours, the relative $\sigma_{\rm m}$ in the liquid density and vapor pressure are smaller than 0.1% and 0.6%, respectively, at all temperatures and for both compounds. These levels of precision exceed by far the accuracy of molecular mechanics force fields.

The data in Figures 2.5 and 2.6 show that, for a given protocol, the relative $\sigma_{\rm m}$ for the liquid density increases with increasing temperature (by about a factor of 4 for $T_{\rm r}$ increasing from 0.6 to 0.9), whereas the relative $\sigma_{\rm m}$ for the vapor pressure does not appear to change significantly over this $T_{\rm r}$ range. For both properties, the relative $\sigma_{\rm m}$ is somewhat smaller for n-octane than for water at the same $T_{\rm r}$.

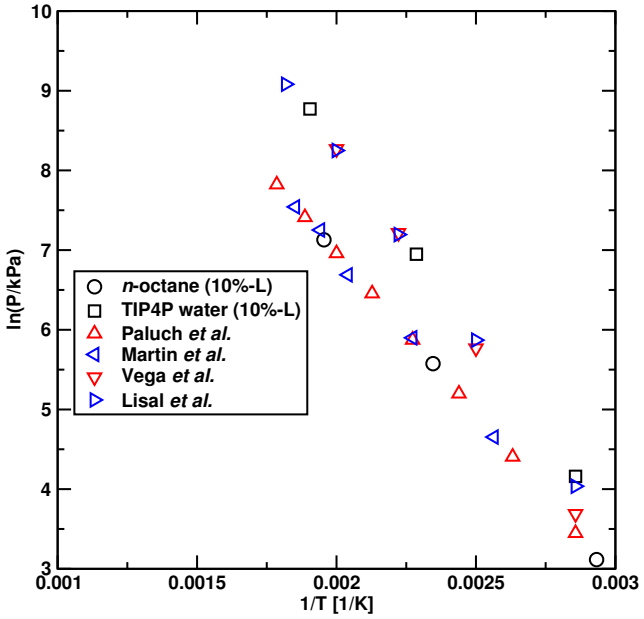

Figure 2.4: Clausius–Clapeyron plot of the saturated vapor pressures for n-octane and water showing a comparison of data obtained for protocol 10–Lo with previous simulation data for the same models.[69,72,77,78]

With respect to the frequency of accepted swap and volume moves, the data for n-octane indicate that protocols yielding about one accepted move of each type per MC cycle (shown by the blue lines in Figures 2.5 and 2.6) are more efficient than those yielding lower or higher acceptance frequencies. For water, protocols with the low and intermediate acceptance frequencies (black and blue lines) are found to perform better than those with the high acceptance frequency, and the numerical data in Table 2.2 show somewhat higher efficiencies for the low acceptance frequency protocols. The higher relative cost of the CBMC swap moves for water (a larger number of choices needs to be explored for the first step due to the smaller fraction of free volume) is likely the reason that the `Lo` protocols are slightly preferable for water.

With respect to the phase ratio, the data indicate that protocols yielding about equal volume (dashed lines) predict vapor pressures with the least precision particularly at lower temperatures. This is not surprising because with this set-up the average number of molecules in the vapor phase becomes very small due to the large density difference

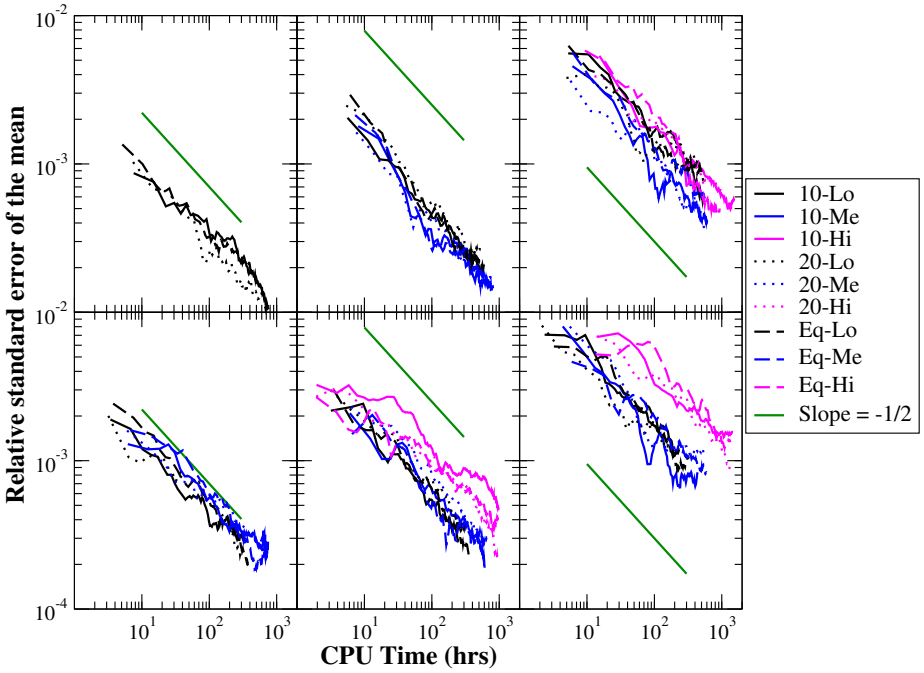

Figure 2.5: Log-log plots of the relative standard error of the mean for the liquid densities as a function of CPU time for n-octane (top) and water (bottom) and $T_{\mathrm{r}} = 0.6$ (left), 0.75 (middle), and 0.9 (right). The green line indicates a slope of –0.5.

between liquid and vapor phases. However, despite that the liquid phase contains the largest number of particles for the `Eq` protocols, these protocols also do not perform well for the prediction of the liquid density. Even at $T_{\mathrm{r}} = 0.9$, the performance of protocols using approximately equal volumes for both phases lags behind in efficiency, but the difference is smaller than at the lower temperatures. For n-octane, a phase ratio with 20% of the molecules in the vapor phase yields the highest precision for both vapor pressure and liquid density. This is also the case for the prediction of the vapor pressure of water, but there is little difference between the `10` and `20` protocols for the relative efficiency of predicting the liquid density. The larger total number of molecules (500 versus 200 molecules) and the larger expense of the computation of the vapor-phase energy (a larger cut-off is needed to reduce the cost of the Ewald summation) is likely the reason that protocols with a smaller fraction of molecules in the vapor phase are competitive for water.

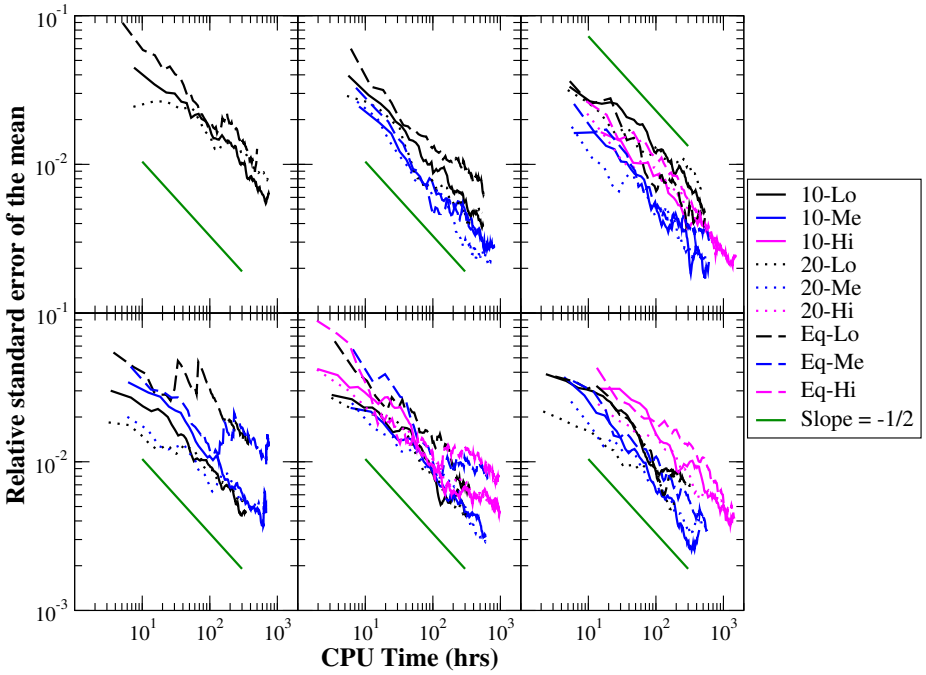

Figure 2.6: Log-log plots of the relative standard error of the mean for the vapor pressure as a function of CPU time. Layout as Figure 2.5.

Considering the data for all nine protocols together (see Table 2.2), protocol `20-Me` is the best choice for n-octane at $T_\mathrm{r} = 0.75$ and 0.9, but due to the pronounced decrease in the acceptance rate at lower temperature the user needs to go for the lower acceptance frequency at $T_\mathrm{r} = 0.6$. For water, protocol `20-Lo` gives the best overall performance when considering both the vapor- and liquid-phase properties.

2.4 Conclusions

A large number of NVT-GEMC simulations was carried out for n-octane and water to assess the influence of the phase ratio and the acceptance frequency for volume and swap moves on the efficiency of predicting vapor- and liquid-phase properties at reduced temperatures ranging from 0.6 to 0.9. The data show that using suitable protocols, GEMC simulations of a duration of 100 hours are sufficient to yield data with a precision of 0.1%

Table 2.2: Relative efficiency, R_{eff}, for different GEMC protocols. The protocols with the highest efficiency for a given property, compound, and reduced temperature are highlighted in bold font.

		liquid density		vapor pressure		
	T_{r}	C_8H_{18}	H_2O	C_8H_{18}	H_2O	average
Eq-Lo	0.60	0.6	0.7	0.5	0.1	0.5
10-Lo	0.60	0.6	**1.0**	0.9	0.6	0.8
20-Lo	0.60	**1.0**	**1.0**	**1.0**	**1.0**	1.0
Eq-Me	0.60	—	0.5	—	0.1	0.3
10-Me	0.60	—	0.6	—	0.3	0.5
20-Me	0.60	—	0.7	—	0.7	0.7
Eq-Lo	0.75	0.6	0.9	0.2	0.3	0.5
10-Lo	0.75	0.8	**1.0**	0.4	0.9	0.8
20-Lo	0.75	0.5	0.7	0.6	**1.0**	0.7
Eq-Me	0.75	0.8	0.9	0.7	0.3	0.7
10-Me	0.75	**1.0**	0.8	0.8	0.9	0.9
20-Me	0.75	**1.0**	0.5	**1.0**	0.9	0.9
Eq-Hi	0.75	—	0.5	—	0.3	0.4
10-Hi	0.75	—	0.3	—	0.6	0.4
20-Hi	0.75	—	0.5	—	0.7	0.6
Eq-Lo	0.90	0.4	0.7	0.3	0.3	0.4
10-Lo	0.90	0.4	0.7	0.2	0.4	0.4
20-Lo	0.90	0.5	**1.0**	0.2	**1.0**	0.7
Eq-Me	0.90	0.6	0.7	0.5	0.4	0.5
10-Me	0.90	0.9	0.8	0.8	0.5	0.7
20-Me	0.90	**1.0**	0.5	**1.0**	0.7	0.8
Eq-Hi	0.90	0.3	0.1	0.2	0.1	0.2
10-Hi	0.90	0.3	0.1	0.4	0.1	0.2
20-Hi	0.90	0.4	0.2	0.4	0.2	0.3

and 1% for the liquid density and vapor pressure, respectively, for n-octane and water with system sizes of 200 and 500 molecules, respectively.

Comparing different simulation protocols, the influence of the phase ratio and the acceptance frequency is larger than the differences between the two compounds (small, rigid, polar, and hydrogen-bonding versus large, articulated, and non-polar). Considering both vapor- and liquid-phase properties, a total volume resulting in a phase ratio with about 20% of the molecules in the vapor phase provides the best performance. With respect to the acceptance frequency, a protocol with about 0.1 accepted volume and one accepted

swap move per MC cycle yields the best performance for water over the entire temperature range and for n-octane at $T_{\mathrm{r}} = 0.6$, but a higher acceptance frequency of about one move per cycle performs slightly better at the higher temperatures for n-octane. Based on this study, a general guideline for GEMC simulations is to adjust the phase ratio to yield approximately 20% of the molecule in the vapor phase and the frequencies of swap and volume moves to yield between 0.1 to 1 accepted move of each type per MC cycle.

Chapter 3

Thermodynamic Derivative Properties of Supercritical Fluids

3.1 Introduction

Modeling the phase behavior and thermophysical properties of reservoir fluids is essential for designing recovery, refinery, and transport processes. For example, heat capacities are often required as input in engineering calculations for designing high-pressure gas pipelines and long-term carbon storage processes.[79] In such processes, fluid properties need to be modeled accurately across a very wide range of conditions, from sub-ambient to high temperatures and pressures. The oil and gas industry has traditionally relied on empirical and semi-empirical equations of state (EoS), such as the SRK[26] and Peng-Robinson[27] EoS, to model PVT fluid properties. These models have found widespread use in the industry due to their simplicity and performance in modeling thermodynamic properties for non-polar and weakly polar substances far from the critical point. However, their reliance on physical measurements limits their predictive capabilities in the absence of experimental data.[18,80] Moreover, their limited performance in describing thermodynamic properties of fluids in the vicinity of critical points is has been known for more than a century.[81] Cubic equations of state, for example, are based on mean field theory, which does not take into account the long-range density and composition fluctuations[82–84] that appear in the vicinity of the critical point. Unless special treatment is applied, such as incorporation of a crossover treatment using valid scaling laws,[85,86] this deficiency in describing long-range

fluctuations constrains EoS performance at near-critical conditions. Higher-order thermodynamic models are therefore necessary to overcome these performance deficiencies.

To improve EoS performance, molecular-based thermodynamic models have been developed to better account for microscopic details, improving physical foundations of traditional models. For example, among the most successful models is the Statistical Associating Fluid Theory (SAFT) family,[34,35,40] which has been used to model thermodynamic properties of complex fluids, such as polymers, surfactants, asphaltenes, and electrolyte solutions, among others.[33] SAFT explicitly takes into account molecular shape and directional interactions (such as hydrogen bonding) within the framework of the thermodynamic perturbation theory of Wertheim,[36–39] allowing for an improvement over classical models in describing phase behavior and thermophysical properties of complex fluids. Nonetheless, the performance of SAFT in the critical region also demonstrates limitations similar to classical equations of state and other mean field methods. The SAFT formulation is based on a repulsive reference fluid, where long-range density fluctuations are not accounted for, while the perturbation terms for attractive interactions are formulated as an expansion around the radial distribution function of the repulsive fluid.[87,88] In this regard, only short-range correlations are explicitly taken into account. Therefore, much effort has been dedicated to improve the formulation of SAFT models in order to overcome these limitations and improve predictive performace. Examples of modifications to SAFT include reassessing the interactions of the reference fluid,[43,44,89] application of crossover treatments based on renormalization-group theory,[48,90] and inclusion of additional perturbation terms that explicitly account for multipolar interactions.[46]

Accurate prediction of second-order thermodynamic derivative properties is widely considered one of the most demanding tests for new EoS development.[79,91] For conditions near the critical point, it is well known that thermodynamic derivative properties exhibit non-monotonic and asymptotic behavior.[92] For example, the isobaric heat capacities of n-alkanes in coexisting vapor and liquid phases become divergent as the critical point is approached,[93] whereas a maximum[41] exists at slightly supercritical conditions and diminishes with increasing temperature. From a modeling perspective, accurately describing this non-linear behavior in derivative properties is challenging for both classical and molecular-based EoS. Recent studies[79,94] have shown that SAFT, perturbed-chain SAFT (PC-SAFT) and the cubic-plus-association (CPA) EoS fail to predict isochoric heat capacity maximas near the critical point for n-alkanes and other compounds of industrial relevance. Nonetheless, maxima in isobaric heat capacities were obtained despite the absence of isochoric

heat capacity maximas. Hence, there is a need for improving the internal thermodynamic consistency in advanced EoS, where different fluid properties can be modeled simultaneously.[95]

In addition to their technological importance, it is also of scientific interest to advance the development of thermodynamic models capable of reliably predicting near-critical derivative properties. To achieve this, the microscopic features that directly influence non-monotonic behavior of thermophysical properties in near-critical fluids must be well understood. In this regard, molecular simulations are well suited for investigating these fundamental features, such as fluid structure and molecular interactions. Molecular simulations can be used to predict derivative properties for a variety of substances,[93,96] where properties can be determined from fluctuation analysis. Moreover, Monte Carlo (MC) simulations have been shown to predict non-monotonic behavior in derivative properties of near-critical fluids.[97] Therefore, the goal of this work is to explore the influence of molecular interactions, model architecture, and fluid structure on thermodynamic derivative properties of supercritical fluids using a Monte Carlo simulations. Emphasis is given to derivative properties at near-critical conditions, which are often the most challenging to model using equations of state. The molecular models tested in this work were fitted to the critical point of n-butane, which allows for exploring the influence of internal degrees of freedom on derivative properties by employing multisite butane-like models. The simulations provide direct insight into molecular-level details and a straightforward approach to predicting thermodynamic derivative properties.

3.2 Simulation Details

3.2.1 Molecular Models

Thermodynamic derivative properties were determined for various molecular models, where different molecular structures and intermolecular potentials were investigated. These models can be categrorized into three main groups: one-site models (OS), tangential-bead models (TAN), and modifications to n-butane models taken from the transferable potentials for phase equilibria force field[69,98] (TraPPE). Table 3.1 lists the values of σ and ϵ parameters for models used in this work.

The united atom version of the TraPPE force field[66,69] uses standard Lennard-Jones and Coulomb potentials for the nonbonded interactions between pseudoatoms:

$$U\left(r_{ij}\right) = 4\epsilon_{ij}\left[\left(\frac{\sigma_{ij}}{r_{ij}}\right)^{12} - \left(\frac{\sigma_{ij}}{r_{ij}}\right)^{6}\right] + \frac{q_i q_j}{4\pi\epsilon r_{ij}} \tag{3.1}$$

Interactions between unlike pseudoatoms are determined using Lorentz-Berthelot combining rules.[99] Intramolecular degrees of freedom are governed by a fixed C–C bond length, a harmonic angle bending potential, and a cosine series torsional potential. The functional form of the torsional potential is given by:

$$U_{\text{tors}} = c_1[1 + \cos\phi] + c_2[1 - \cos(2\phi)] + c_3[1 + \cos(3\phi)] \tag{3.2}$$

The original TraPPE–UA n-butane model was modified by altering its internal degrees of freedom. Three models were used where the motion of dihedral angles was modified to allow for torsions of varying flexibility. For this, the coefficients in Equation 3.2 were scaled up and down by a factor of 5 with respect to those TraPPE–UA n-alkanes, as well as setting all coefficients equal to zero to allow for fully flexible torsions. TraPPE–UA n-butane was also modeled as rigid multisite particles, where all molecules in the system were "frozen" in either *cis* or *trans* configurations. A rigid all-*trans* model of the explicit-hydrogen version of the TraPPE force field[98] was also investigated, where the influence of the number of interaction sites was assessed without a large increase in computing effort due to limitated intramolecular degrees of freedom. In addition, the original TraPPE-UA model was used in conjuction with a harmonic C–C bond stretching potential, where the force constant ($k_{\text{b}} = 235.5$ kcal/mol/Å) was taken from the CHARMM[100] force field for linear alkanes, similar to the approach taken by Tobias and co-workers.[101]

Force field parameters for one-site models were fitted for three different pair potentials: Mie (OS n-m), Buckingham exponential-6 (EXP-6), and square well (SW) potentials. The Mie potential has the form:

$$U\left(r_{ij}\right) = \left(\frac{n}{n-m}\right)\left(\frac{n}{m}\right)^{m/(n-m)}\epsilon_{ij}\left[\left(\frac{\sigma_{ij}}{r_{ij}}\right)^{n} - \left(\frac{\sigma_{ij}}{r_{ij}}\right)^{m}\right] \tag{3.3}$$

where n and m denote repulsive and attractive exponents, respectively. The standard Lennard-Jones potential is recovered from Equation 3.3 when $n = 12$ and $m = 6$. The influence of repulsive steepness was investigated using OS models interacting via Mie potentials, where the attractive exponent was kept constant at $m = 6$ and the repulsive exponent n was set to either 9, 12, 15, or 32. For the OS 12-6 model, σ and ϵ were obtained from the result of a finite-size scaling study of Potoff and Panagiotopoulos for

Lennard-Jonesium.[102] Initial estimates for the parameter fitting procedure of the remaining OS n-m models were based on the results of Okumura and Yonezawa.[103] For the EXP-6 model, the functional form of the pair potential is given by:

$$U\left(r_{ij}\right) = \frac{\epsilon}{1-6/\alpha}\left[\frac{6}{\alpha}\left(\alpha\left[1-\frac{r_{ij}}{r_{\mathrm{m},ij}}\right]\right) - C\left(\frac{r_{\mathrm{m},ij}}{r_{ij}}\right)^{6}\right] \tag{3.4}$$

where $r_{\mathrm{m},ij} = 2^{1/6}\sigma_{ij}$. Because the parameters for any given model were fit to the critical temperature and critical density of n-butane as opposed to the full vapor-liquid coexistence curve, the values of σ and ϵ were used as adjustable parameters while the other two parameters in Equation 3.4 were fixed to $C = 1$ and and $\alpha = 14$, in accordance with the equation of state of Dodd and Sandler.[104] Initial estimates for ϵ and σ were based on the results of Errington and Panagiotopoulos.[105] The EXP-6 model provides an additional model to assess repulsive interactions, given that the repulsive part of the Buckingham potential is meant to describe the interpenetration of the closed electron shells between interacting pairs. To provide a model with hard-repulsion, an OS model interaction via a square well potential was investigated. This pair potential is given by:

$$U\left(r_{ij}\right) = \begin{cases} +\infty, & \text{if } r < \sigma_{ij} \\ -\epsilon, & \text{if } \sigma \leq r < \lambda\sigma_{ij} \\ 0, & \text{if } r \geq \lambda\sigma_{ij} \end{cases} \tag{3.5}$$

where λ denotes the well range. Initial estimates for ϵ and σ were based on the results of a phase equilibria study using GEMC simulations for square well fluids by Vega and coworkers,[106] from which critical properties for fluids of range $\lambda = 1.25$ were taken. This model was primarily used to assess the influence of hard repulsion in isochoric heat capacities, given that previous studies suggest repulsive interactions play a role in the behavior of this property at near-critical conditions.[107,108]

Molecules in tangential-bead models consist of 4 identical interaction sites where the bond length is set equal to σ. Two variations were investigated: a rigid model in a linear configuration and a flexible model, where angle bending and torsional potentials were to those of TraPPE–UA for linear alkanes. To fit σ and ϵ for these models, the parameters used for inital estimates were taken from a freely-jointed chain model used by Martin and coworkers for n-octane.[109]

Table 3.1: Non-bonded interaction parameters for one-site (OS), tangential-bead (TAN), and TraPPE n-butane models. TraPPE-UA parameters given here apply to all TraPPE-UA modifications in this work. Parameters for C–H bond sites and for methyl ([C]H_3) and methylene ([C]H_2) carbon atoms were taken from Chen and Siepmann.[98] For OS models, m–n ($m = 9, 12, 15, 32$, $n = 6$) notation indicates repulsive and attractive exponents, respectively. OS models interacting via square well and Buckingham exponential-6 potentials are labeled SW and EXP-6, respectively. Tangential-bead models indicated with TAN label.

Interaction Site	σ [Å]	ϵ/k_B [K]
TraPPE-UA CH_3	3.75	98.00
TraPPE-UA CH_2	3.95	46.00
TraPPE-EH Trans [C]H_3	3.30	4.00
TraPPE-EH Trans [C]H_2	3.65	5.00
TraPPE-EH Trans C–H	3.31	15.30
OS 9–6	5.08	272.00
OS 12–6	5.11	323.90
OS 15–6	5.12	366.21
OS 32–6	5.24	475.83
SW	5.39	556.28
EXP-6	5.14	342.00
TAN–Linear	2.98	747.20
TAN–Flexible	3.00	772.00

3.2.2 Monte Carlo Simulations

Monte Carlo (MC) simulations offer a sophisticated approach for predicting phase equilibria and thermophysical properties of fluids that is applicable to a wide variety of molecular structures. In this work, the MCCCS–MN program[74] was used to obtain thermodynamic derivative properties from MC simulations. The approach taken follows a three step procedure for any given molecular model. First, Gibbs ensemble Monte Carlo (GEMC) simulations[57,59,67] were carried out to compute the vapor-liquid coexistence curve for the molecular model of interest, were force field parameters were fitted to the critical point of n-butane. The system size for all simulations consisted of 1000 molecules, and a spherical cutoff of 1.4 nm was used to truncate non-bonded interactions. Except for the SW model, analytical tail corrections were employed.[54] Production periods of 100,000 MC cycles were used for these simulations, where 1 MC cycle consists of N steps and N is given by to the total

number of particles in the system. Simulation averages were determined using 8 independent runs. Volume and swap moves were adjusted to yield an acceptance frequency on the order of 1 accepted move of each type per MC cycle[110] to optimize computing efficiency. The remaining fraction of moves were evenly distributed among translations, rotations for multisite models, and CBMC conformational moves[61,62,64–66] for flexible molecules. Critical temperatures and densities were computed using the saturated density scaling law[111] and the law of rectilinear diameters[112] with a scaling exponent $\beta^* = 0.326$.[59]

For the second step, MC simulations in the canonical (NVT) ensemble are carried out at a temperature of 467.5 K. This corresponds to a temperature that is 10% above the experimetnal critical temperature of n-butane.[113] For this compound and other light hydrocarbons, $T_\mathrm{r} = 1.1$ is sufficiently close to the critical point such that non-monotonic behavior in thermodynamic derivative properties is observed.[114] NVT simulations were carried out for a series of reduced densities in the range of 0.25–3.00, where the corresponding density is reduced with respect to the experimental critical density. Production periods of 200,000 MC cycles were used for a system size of 1000 molecules. As for GEMC simulations, averages were computed from 8 independent runs, where a 1.4 nm spherical cutoff was used and analytical tail corrections were employed, with the exception of simulations with the SW model. From this set of simulations, pressures were estimated for each reduced density. Additionally, the isochoric heat capacity (C_V) was estimated using fluctuation analysis. By definition, C_V is given by:

$$C_V = \left(\frac{\partial U}{\partial T}\right)_V \tag{3.6}$$

where $U = U_\mathrm{excess} + U_\mathrm{ideal} + \mathrm{KE}$ is the total potential energy and KE denotes kinetic energy. Given that the KE term is not available from a Monte Carlo simulation, C_V is required to be split into ideal and residual parts:

$$C_V(T,V) = C_{V,\mathrm{ideal}}(T) + C_{V,\mathrm{res}}(T,V) \tag{3.7}$$

where the ideal gas part is simply a function of temperature and can be determined from either physical measurements, experimental correlations,[31] or vibrational frequency analysis.[115] The residual part in Equation 3.7 was determined from fluctuations in the intermolecular part of the potential energy, given by:

$$C_{V,\mathrm{res}} = \frac{1}{k_B T^2}\left(\left\langle U_\mathrm{inter}^2\right\rangle - \left\langle U_\mathrm{inter}\right\rangle^2\right) \tag{3.8}$$

where k_B is the Boltzmann constant and $\langle X\rangle$ denotes the ensemble average for property X.

For the third and final step in this approach, MC simulations in the isobaric-isothermal (NpT) ensemble were carried out, where the pressure estimates from NVT simulations were used as input for NpT simulations at corresponding reduced densities. Similar to NVT simulations, production periods of 200,000 MC cycles were used for a system size of 1000 molecules. Averages were taken from 8 independent runs, where the spherical cutoff and tail correction setup used was equivalent to that of NVT simulations. In addition to providing an additional tool for determining C_V, five other thermodynamic derivative properties were computed using NpT simulations: isobaric heat capacity (C_p), volume expansivity (β_p), isothermal compressibilty (κ_T), Joule-Thomson coefficient (μ_{JT}), and speed of sound (ω). As was done for C_V, C_p can be split into ideal and residual parts:

$$C_p = C_{p,\mathrm{ideal}} + C_{p,\mathrm{res}} \tag{3.9}$$

where $C_{p,\mathrm{ideal}}$ is again determined from either experimental correlations,[31] vibrational frequency analysis,[115] or physical measurements. The residual part is determined from:

$$C_{p,\mathrm{res}} = \left(\frac{\partial H_{\mathrm{inter}}}{\partial T}\right)_p - Nk_B \tag{3.10}$$

where $H_{\mathrm{inter}} = U_{\mathrm{inter}} + pV$. Analogous to $C_{V,\mathrm{res}}$, this derivative may be calculated from fluctuations of the enthalpy in the isobaric-isothermal ensemble:[96]

$$\left(\frac{\partial H_{\mathrm{inter}}}{\partial T}\right)_p = \frac{1}{k_B T^2}\left(\left\langle H_{\mathrm{inter}}^2\right\rangle - \left\langle H_{\mathrm{inter}}\right\rangle^2\right) \tag{3.11}$$

NpT simulations were also used to directly compute β_p and κ_T using fluctuation analysis. These are given by:[93]

$$\beta_p = \frac{1}{\langle V\rangle}\left(\frac{\partial \langle V\rangle}{\partial T}\right)_p = -\frac{k_B\beta^2}{\langle V\rangle}\left(\langle V\rangle\langle H\rangle - \langle VH\rangle\right) \tag{3.12}$$

$$\kappa_T = -\frac{1}{\langle V\rangle}\left(\frac{\partial \langle V\rangle}{\partial p}\right)_p = \frac{-1}{k_B T\langle V\rangle}\left(\left\langle V^2\right) - \langle V\rangle^2\right) \tag{3.13}$$

where $H = U_{\mathrm{inter}} + U_{\mathrm{intra}} + pV$ is the configurational enthalpy (whereas the total enthalpy includes a KE term), U_{intra} is the intramolecular potential energy, and $\beta = 1/k_B T$. The remaining derivative properties can then be computed from C_p, β_p, and κ_T:[97]

$$C_V = C_p - T\langle V\rangle\frac{\beta_p^2}{\kappa_T} \tag{3.14}$$

$$\mu_{\mathrm{JT}} = \frac{1}{C_p}\left[T\left(\frac{\partial \langle V\rangle}{\partial T}\right)_p - \langle V\rangle\right] = \frac{\langle V\rangle}{C_p}[T\beta_p - 1] \tag{3.15}$$

$$\omega^2 = \frac{C_p}{C_v} \frac{\langle V \rangle}{\left(\frac{\partial \langle V \rangle}{\partial p}\right)_T} \frac{MN_A}{N} = \frac{C_p}{C_v} \frac{MN_A}{N} \frac{\langle V \rangle}{\kappa_T} \tag{3.16}$$

where M denotes molecular weight and N_A is Avogadro's number.

3.3 Results and Discussion

The procedure described in Section 3.2.2 for fitting force field parameters yields the vapor-liquid coexistence curves for each model. Figure 3.1 shows the coexistence curves obtained using the fitted parameters given in Table 3.1. These results show that there is minimal variation in the critical temperatures and pressures of these models. The largest deviations with respect to the experimental value ($T_c = 425.12$ K) correspond to the rigid *cis* and *trans* TraPPE–UA models, where critical temperature estimates were $T_c = 430.60$ K for the *cis* model and $T_c = 420.45$ K for the *trans* model. This slight deviation is not unexpected given that σ and ϵ parameters are the same as those of the original TraPPE–UA model, yet their torsional degrees of freedom are constrained to rigid configurations. Nonetheless, the

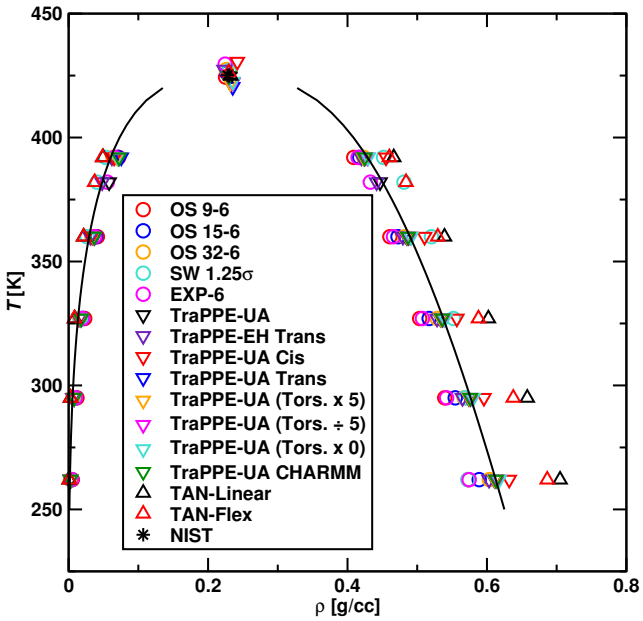

Figure 3.1: Vapor-liquid coexistence curves for each molecular model. Experimental values taken from NIST.[113]

slight deviation in critical temperature has negligible impact on the behavior of derivative properties at $T = 467.5$ K, as will be shown in the following sections. Since parameter fitting is carried out with respect to the critical point, liquid densities are directly influenced by molecular shape. OS models yield the smallest densities, while the TAN models yield the largest.

3.3.1 Isobaric Heat Capacity, Isothermal Compressibility, and Volume Expansivity

Residual isobaric heat capacities obtained directly from from fluctuations in the isobaric-isothermal ensemble are shown in Figure 3.2. Predicted values from MC simulations are compared with experimental values, where residual values were determined as $C_{p,\mathrm{res}} = C_p(\rho) - C_p(\rho = 0)$. The results show that each OS, TraPPE, and TAN model tested yields a peak around the critical density, consistent with experimental observations. The largest

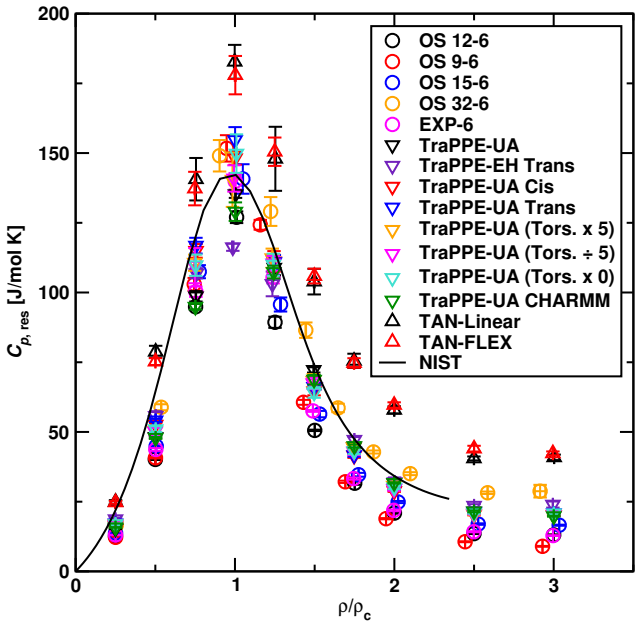

Figure 3.2: Residual isobaric heat capacities as a function of reduced density at $T = 467.5$ K. Experimental values taken from NIST.[113]

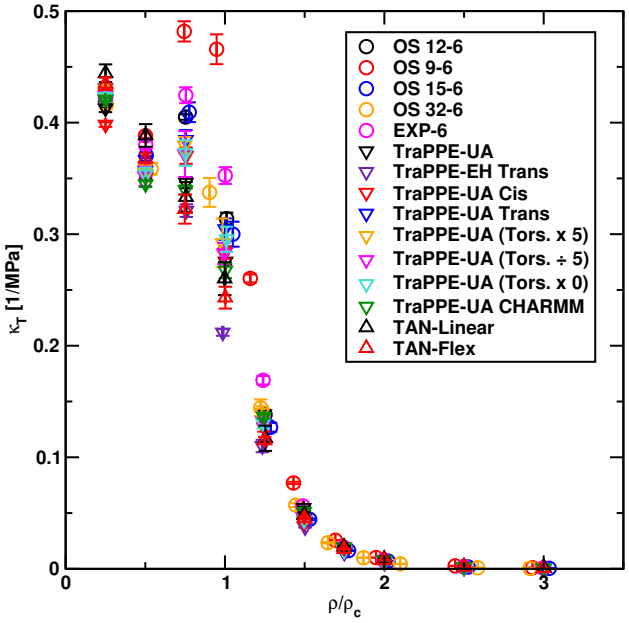

Figure 3.3: Isothermal compressibilities as a function of reduced density at $T = 467.5$ K.

differences are observed at densities near ρ_c, where fluctuations become larger. It is important to note that this property depends on enthalpy fluctuations, where volume moves contribute directly to the value of C_p due to fluctuations in the pV term. For this reason, the differences in heat capacities are relatively small at lower densities where volume moves have smaller effects on the interactions between molecule pairs, and become larger at higher densities. Around the critical density, the results show larger scattering due to increased fluctuations, where the TAN models show the largest deviations from experimental values. This overestimation is also observed at higher densities for TAN models, which exclude intramolecular repulsive interactions. Hence, any given pair of TAN molecules will experience a relatively large change in energy when an accepted move (*i.e.* translation, volume change, etc.) brings pseudoatoms from each molecule to a distance within the repulsive region of the pair potential. Because molecules pack tightly at high densities, the fluctuations are larger in this region for molecules where repulsive interactions are dominant. For example, this effect causes the value of C_p for OS models to increase with increasing steepness in the repulsion, where the OS 32-6 model yields the largest C_p of

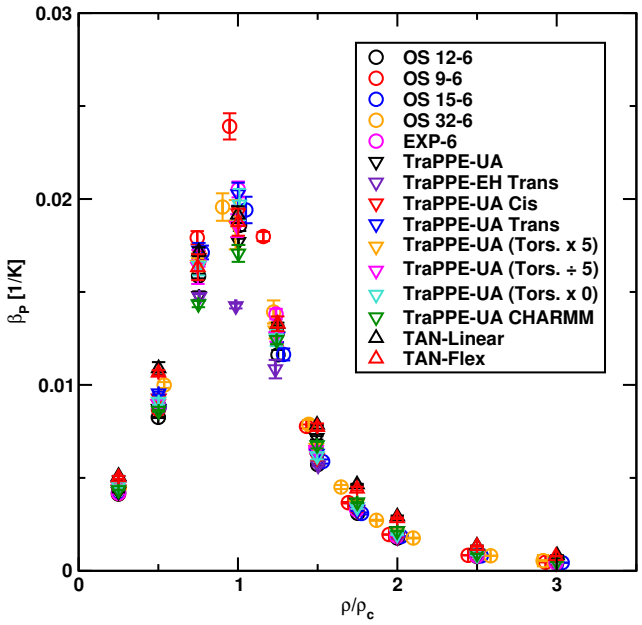

Figure 3.4: Volume expansivity as a function of reduced density at $T = 467.5$ K.

all OS models. In general, the TraPPE models seem to provide the most adequate descriptions of enthalpic fluctuations across the full range of densities, as these models show the best agreement with experimental values at low, intermediate, and high densities. All TraPPE–UA variations yielded similar results despite the conformational constraints applied.

This agreement in isobaric heat capacities between TraPPE–UA models with distinct conformational preferences may seem to contradict the work of Bessières $et\ al.$,[116] where they suggest that TraPPE–UA descriptions of n-alkanes yield temperature-dependent behavior in residual heat capacities that reflect changes in orientational ordering between alkane molecules. However, their work focused on n-alkanes of longer chain lengths across different temperatures, whereas the results found here were carried out at a fixed temperature ($T_\mathrm{r} = 1.1$) and with shorter alkane models. Moreover, angular distributions were verified for different multisite models to screen for orientational ordering, yet isotropic fluid behavior was obtained across the entire density range. While the constant aspect ratio of the TAN-Linear model might have allowed for liquid-crystalline orientations, this was not observed at any density (see Appendix A). The lack of long-range orientational ordering

for the TAN-Linear model is similar to the results of Vega $et\ al.$,[117] where they suggest that linear tangent hard sphere models with 4 monomer units do not exhibit liquid crystalline phases but rather directly transition from isotropic liquid phases to ordered solid phases. Galindo $et\ al.$[118] also reported a lack of long-range orientational ordering for tetramers of flexible and linear rigid chain molecules with tangential LJ monomers.

The isothermal compressibility is known to exhibit a peak near the critical point for supercritical fluids, similar to C_p. The results for this property are shown in Figure 3.3. Except for densities near ρ_{c}, the values for κ_T are very similar. This is because κ_T is determined from volume fluctuations (see Equation 3.13), where molecular pair interactions have a smaller weight in comparison to changes in volume. This does not imply that molecular interactions do not play a role in determining κ_T, but rather that the influence molecular interactions on volume fluctuations ultimately determines the behavior of this property. For example, the role of molecular interactions can be more clearly observed at $\rho_{\mathrm{r}} = 1$. At this density, the lower repulsive exponent of the OS 9-6 model allows it to yield a larger peak in κ_T, suggesting this model predicts a very highly compressible fluid at the critical density. In contrast, the OS 32-6 model yields smaller κ_T values near the critical density, comparable to those of TraPPE models. The spherical shape of the OS models allows for tight molecular packing in comparison to multisite models, which promotes the relatively high κ_T values observed at the critical density. Hence, repulsive interactions and molecular shape influence κ_T the most at densities near ρ_{c}.

The volume expansivity is dependent upon both volume and enthalpy fluctuations, as shown in Equation 3.12. Similar to κ_T and C_p, a peak is expected near the critical density. The results obtained for volume expansivity are given in Figure 3.4. These results show that each model indeed predicts the existence of a β_p maximum at the critical density. Since β_p has a strong dependence on volume changes, the differences between molecular models is most pronounced around the critical density, similar to the behavior observed for κ_T. The OS 9-6 model again shows the largest value at the peak position due to the relatively small repulsive interactions between molecule pairs. The results obtained for C_p, κ_T, and β_p suggest that NpT Monte Carlo simulations allow for very consistent predictions for this set of properties, where simulations with each model was capable of capturing the expected non-monotonic behavior.

3.3.2 Isochoric Heat Capacity, Joule-Thomson Coefficient, and Speed of Sound

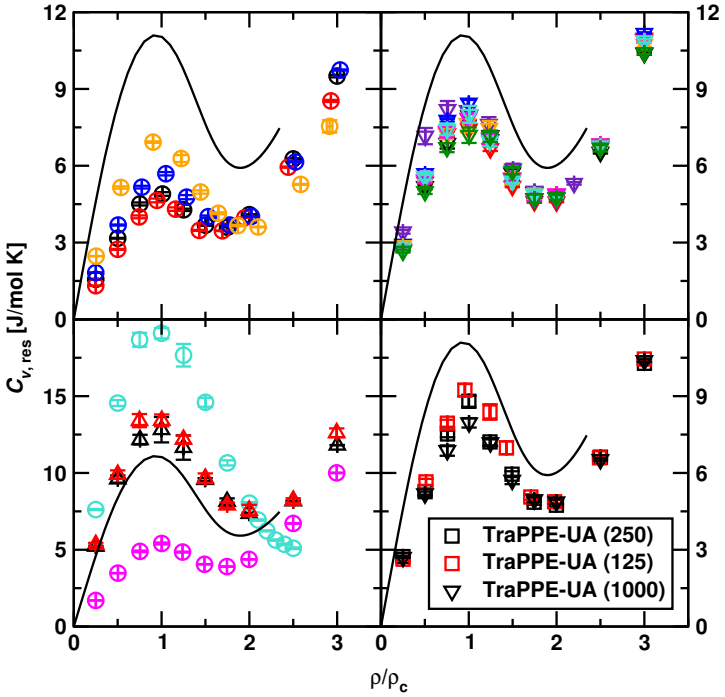

Figure 3.5: Residual isochoric heat capacities as a function of reduced densities at $T =$ 467.5 K. Symbols defined in Figure 3.1 for bottom left and top panels. For lower right panel, symbols denote simulation results using different system sizes.

In comparison to C_p, isochoric heat capacities have higher sensitivity to molecular interactions due to the direct dependence of C_V on potential energy fluctuations, as shown in Equation 3.8 for simulations in the canonical ensemble. For NpT simulations, terms that include contributions to C_p coming from volume fluctuations are subtracted to determine C_V, as shown Equation 3.14. Due to the additional contributions from volume fluctuations in C_p, fluids that exhibit a C_p maxima do not necessarily exhibit C_V maxima, yet the existence of a C_V maxima likely indicates that a C_p maxima also exists. While not universal to all fluids, the non-monotonic behavior in C_V is known to yield two specific extremas: a maximum at the critical density and a minimum at slightly higher densities. Experimental

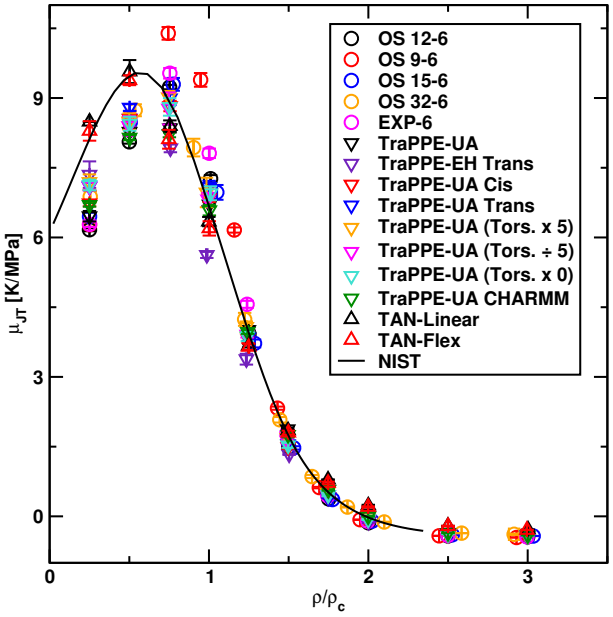

Figure 3.6: Joule-Thomson coefficient as a funtion of reduced densities at $T = 467.5$ K. Experimental values taken from NIST.[113]

data (black lines) in Figure 3.5 indicate that these two extremas exist for n-butane at 467.5 K.

To illustrate the influence of molecular interactions, the results for $C_{V,\mathrm{res}}$ are shown separately in Figure 3.5 for OS models (top left), TraPPE models (top right), and EXP-6, TAN, and SW models (bottom left). Simulation results show that all OS n-m models yield a C_V peak, yet the peak height becomes larger with repulsion steepness with a constant attractive exponent. In other words, higher repulsion exponents could be used to match predicted peaks to the experimental peak heights. However, as shown in Section 3.3.1, other fluid properties may respond unfavorably to the use of highly unphysical repulsive exponents. The behavior of the EXP-6 model very closely resembles that of the OS 12-6 model, suggesting both models provide similar descriptions of the balance between attractive and repulsive molecular interactions. Similarly all multisite models provide good qualitative agreement with experiment. The inclusion of multiple interaction sites seems to provide for an increase in the values of $C_{V,\mathrm{res}}$, particularly for lower densities up to the critical density. This is clearly observed when comparing $C_{V,\mathrm{res}}$ values for the OS 12-6

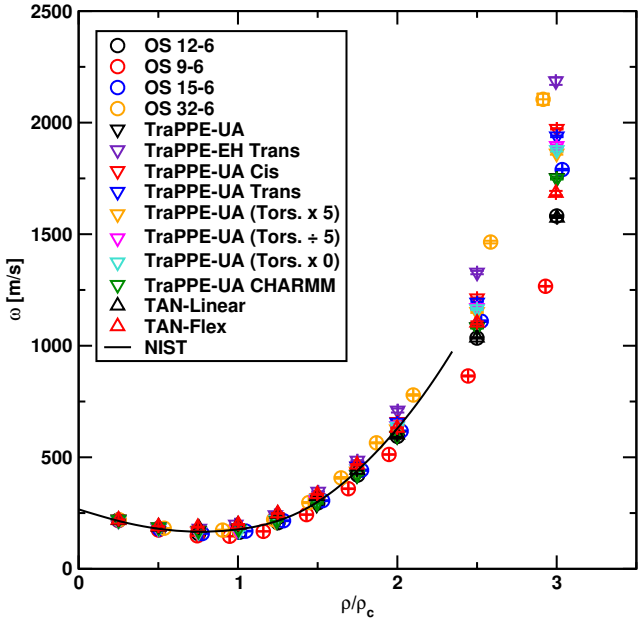

Figure 3.7: Speed of sound as a function of reduced densities at $T = 467.5$ K. Experimental values taken from NIST.[113]

model with any TraPPE model, given that the non-bonded potential is consistent among these models and they only differ in molecular shape. Given that pair interactions have greater influence on derivative properties in the low density limit where distances between molecule pairs are at their largest, a proper distribution of interaction sites favors accurate predictions at low densities. This is shown for the rigid TraPPE–EH model, which provides nearly quantitative agreement with experimental $C_{V,\mathrm{res}}$ values for densities lower than $\rho_\mathrm{r} = 0.75$. Both TAN models also provide good descriptions at low densities, yet slightly overestimate $C_{V,\mathrm{res}}$ values throughout most of the density range.

The largest $C_{V,\mathrm{res}}$ maximum was observed for the SW model, which greatly overpredicted $C_{V,\mathrm{res}}$ values near the critical density. This is due to its relatively short attractive range (1.25σ) used, as well as the discontinuous form of the potential. The potential energy undergoes a relatively large change when a MC move is accepted that brings molecule pairs from distances beyond 1.25σ to fall within the attractive well. A similar change in energy ocurrs for the reverse process. The energy fluctuations, and therefore $C_{V,\mathrm{res}}$, become large as the frequency of these sharp energy changes increases near the critical density.

The effect of well range was verified separately by increasing the range to 1.75σ (hence, predicting substantially different T_{c}). This test yielded similar qualitative behavior at the same reduced temperatures ($T_{\mathrm{r}} = 1.1$), yet the predicted peak height became lower for the larger well range (see Appendix A). The influence of system size was also verified by performing simulations for the original TraPPE–UA model using system sizes of 250 and 125 particles. The results are shown in the lower right panel of Figure 3.5. These results indicate that system size effects influence $C_{V,\mathrm{res}}$ values near the critical density for simulations with smaller amounts of particles. The effect has negligible impact on $C_{V,\mathrm{res}}$ values at the low- and high-density regions.

According to the work of Freasier $et\ at.$,[107] models that predict $C_{V,\mathrm{res}}$ maxima require intermolecular potentials that have an attractive well, whereas purely repulsive potentials do not predict C_V maxima. On the other hand, C_V minima were explained on the basis of soft-core penetration, where their results showed the minima were not predicted using models with hard repulsion potentials. Their interpretation for the overall behavior of C_V was based on the interplay between molecular aggregation, caging, and soft-core repulsion, and has been interpreted similarly in other studies.[119–121] The results shown in Figure 3.5 agree with the explanation that soft repulsion is required to observe the C_V minima, where the SW model is shown to fail in predicting this minima due to its hard core. Despite the large repulsive exponent in the OS 32-6 model, the fact that it includes both soft repulsion and an attractive well allows for qualitative agreement with experimental measurements, predicting both extremas at the correct reduced densities. While adjusting the attractive range of the SW model may allow for quantitative predictions at the critical density, the lack of soft repulsion hinders the predictive performance for this model because it is unable to properly describe fluctuations in potential energy coming from repulsive pair interactions for fluids at high densities.

In addition to properly describing heat capacities, accurately modeling Joule-Thomson coefficients is important process design because it describes the temperature change of a fluid when it undergoes a change in pressure. For example, determining the Joule-Thomson inversion curve is essential for the design of throttling processes.[122] Likewise, predictiing the speed of sound coefficient is regarded as one of the most demanding tests for new EoS development because of its greater sensitivity to deviations.[41] Simulation results for these two properties are provided Figures 3.6 and 3.7. The results show that all models are in good qualitative agreement for μ_{JT}, with the best agreement found for TAN models. At the maximum, the OS 9-6 model shows the largest overestimation, yet this

result is not surprising given the direct relationship between μ_{JT} and β_p. On the other hand, simulation results for ω are in excellent agreement with experimental data for all models, particularly at densities below $\rho_{\mathrm{r}} = 2.00$. This result shows the robustness of Monte Carlo simulations for predicting ω, where proper descriptions of both heat capacities allows for good agreement with experiment. Accurate description of the ratio of heat capacities is important to properly predict ω, which is the reason for the large deviations reported using EoS that only yield one of two heat capacity maximas (such as PC-SAFT[79]) at near-critical conditions.

3.3.3 Structural Analysis

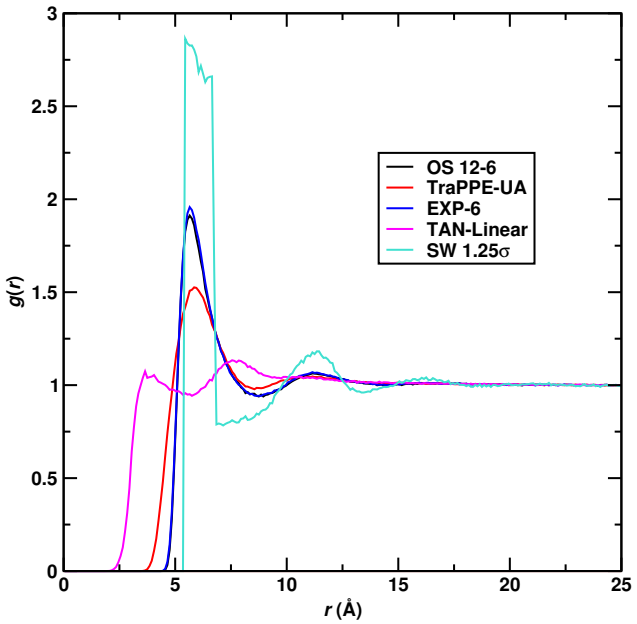

Figure 3.8: Center of mass radial distribution functions for various models at $\rho_{\mathrm{r}} = 1.00$

One of the most useful features of molecular simulations is their capability of providing a molecular-level view into system structure. To analyze the influence of molecular packing on thermodynamic derivative properties, center of mass radial distribution functions (RDF) were computed for different models across the full range of reduced densities. Figure 3.8 shows RDFs for five different models at the critical density. The shape of these RDFs

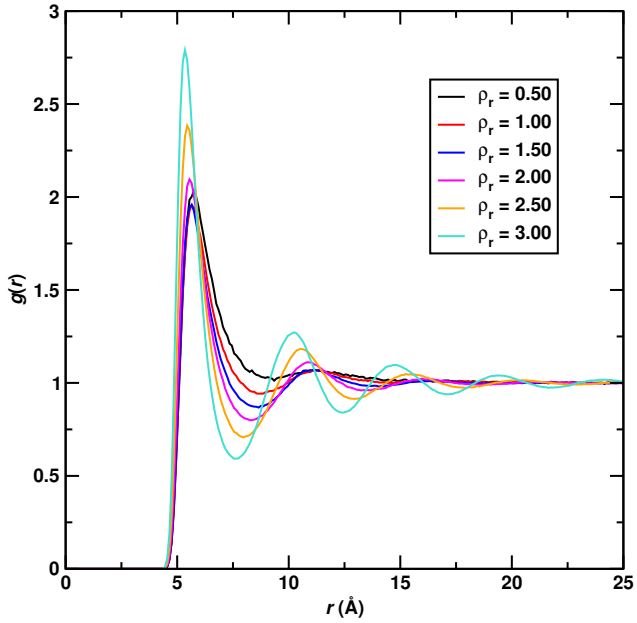

Figure 3.9: Center of mass radial distribution functions for EXP-6 pairs at different reduced densities.

clearly indicate that the molecular shape and pair potential of these models directly influence molecular packing arrangements. The rigid configuration of the TAN-Linear model allows molecules to pack in different configurations, where parallel configurations allow for closer packing than for other models as indicated by the peak position in the first solvation shell. On the other hand, the first solvation shell for OS 12-6 molecules is larger than that of TraPPE–UA and TAN-Linear models despite interacting via the same non-bonded pair potential, indicating that molecular shape influences the packing arrangements within the sphere of nearest neighbors. The EXP-6 and OS 12-6 models show very similar RDFs, yet both differ significantly from the packing behavior of the SW model despite molecules being modeled as one spherical interaction site in all three models. These results suggest that molecular packing behavior is directly influenced by the interplay of the pairwise interactions and molecular shape.

To investigate the relationship between molecular packing and derivative properties, it is important to examine RDFs across the entire density range. Figure 3.9 shows RDFs for

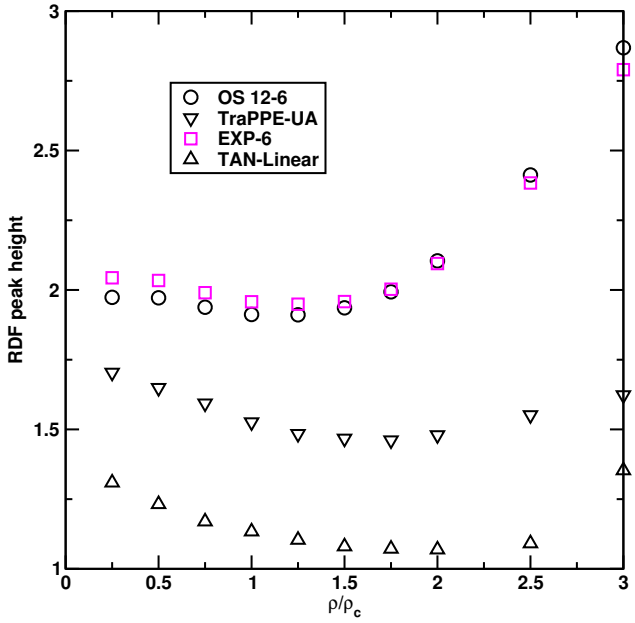

Figure 3.10: RDF peak heights as a function of reduced density for various models.

the EXP-6 model at diferent densities, where results show that the fluid exhibits a structural transition from a gas-like fluid at low densities to a liquid-like fluid at higher densities. Similar structural transitions have been observed previously for supercritical fluids in the near-critical regime,[123,124] where the transition coincides with the extrema found in the derivative properties. Other models also exhibit similar packing transitions as a function of fluid density. This result suggests that transitions in fluid structure are directly linked with non-linear behavior in derivative properties close to the critical point.

Structural transitions for other models were investigated by analyzing the height of the first RDF peak as a function of reduced density. Results are provided in Figure 3.10 for four considerably different models. The results indicate similar behavior for each model, where the peak for the first solvation shell becomes smaller with density between low and intermediate densities. However, the RDF peak becomes larger with density in the high-density region. The change in packing behavior of the first solvation shell closely resembles the results of Pfund $et\ al.$,[84] where they observed that the compressibility factor ($Z = p\hat{V}/RT$, where R is the universal gas constant and $\hat{V}$ is the molar volume) and the values of NMR specific shielding computed from $g(r)$ were simultaneously minimized at a

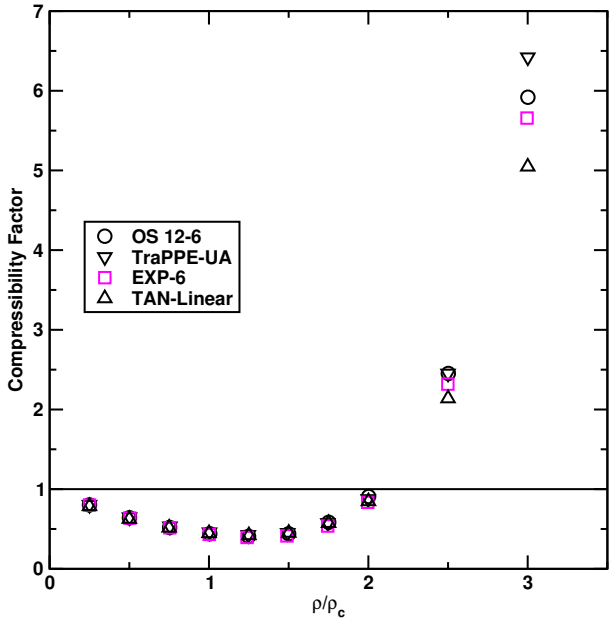

Figure 3.11: Compressibility factor for various models across the full density range. The solid line denotes the ideal gas compressibility factor ($Z = 1$).

density higher than that of maximum isothermal compressibility (*i.e.* near the critical density). Their experimental observations are similar to the simulation results obtained here for RDF peak heights and for compressibility factors, which are shown in Figure 3.11 for the same four models as in Figure 3.10. While the behavior of RDF peak heights varies slighly among different models, the values for Z are very similar, particularly for densities below $\rho_{\mathrm{r}} = 2.00$. Nonetheless, the peak in the first solvation shell is a decreasing function of density up to a density larger than ρ_{c} for all models, despite the increase in bulk density. Pfund $et\ al.$ interpreted this inverse proportionality to density as a structual degradation in the first solvation shell, where the interaction of coordination spheres surrounding each particle reduces the effective attraction between molecule pairs at low to intermediate densities. This loss of structure near the critical point is also observed for strongly associating fluids, such as in near-critical water.[125] Beyond the minimum in RDF peak heights, both Z and RDF peaks simultaneously increase, suggesting molecules in the first solvation shell become increasingly compressed with density. As molecules become compressed at high densities, fluctuations in potential energy, and therefore C_V, become larger because pair

distances fluctuate near the repulsive part of the pair potential, yielding a minima in C_V at around $\rho_{\mathrm{r}} = 2.00$. This density is near the limit of $Z = 1$, suggesting C_V minima is linked to a transition in compressibility factor from low compressibility ($Z < 1$) to high compressibility ($Z > 1$). Therefore, the maxima observed in derivative properties near the critical point exist as a consequence of molecular packing transitions from gas-like to liquid-like structures, consistent with the structural transition observed for supercritical fluids crossing the Widom line.[126] In contrast, the minimum in C_V is related to a change in fluid compressibility where molecules in the first solvation shell become compressed with density. From a molecular modeling standpoint, these results suggest that molecular packing transitions need to be described correctly in order to properly reproduce non-linear behavior in derivative properties close to the critical point.

3.3.4 Thermodynamic Derivative Properties at $T^* = 2.4$

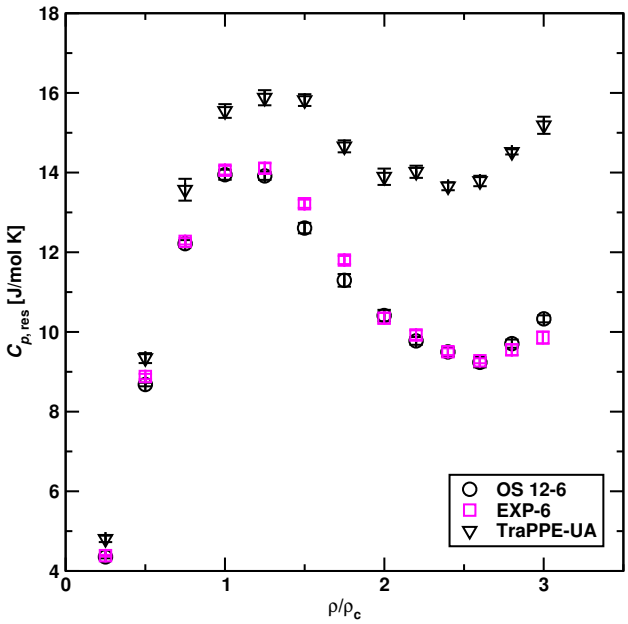

Figure 3.12: Residual isobaric heat capacities as a function of reduced density at $T =$ 777.5 K.

Recent studies[119,120] have found that both isochoric and isobaric heat capacities exhibit

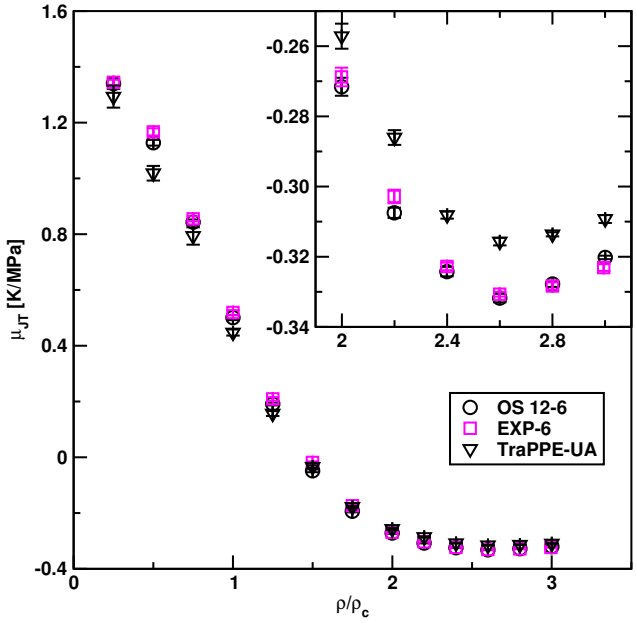

Figure 3.13: Joule-Thomson coefficient as a function of reduced density at $T = 777.5$ K. Inset shows a close-up view where a minimum is observed.

maxima and minima, where the loci exhibit the same power law behavior as vapor-liquid coexistence curves with an exponent of $\beta = 0.32$. While the minimum in C_V is well-known and commonly observed at near-critical conditions, the minimum in C_p is only observed at higher temperatures and is relatively shallow. Yigzawe[119] modeled this minima using molecular dynamics simulations of Lennard-Jonesium and the Johnson EoS.[127] To investigate the molecular details of this unusual minimum, NpT Monte Carlo simulations were performed at $T^* = 2.4$ (where $T^* = kT/\epsilon$) for reduced densities between 0.25 and 3.00, where a C_p minimum exists at approximately $\rho^* = \rho\sigma^3 = 0.74$ according to the results of Yigzawe. For Lennard-Jonesium n-butane, this temperature and density correspond to $T = 777.5$ K and $\rho = 0.5352$ g/cc (approximately $\rho_\mathrm{r} = 2.35$), respectively. Simulations were performed following a procedure analogous to the approach described in Section 3.2.2 for three different models: OS 12-6, EXP-6, and TraPPE–UA.

Results for $C_{p,\mathrm{res}}$ at 777.5 K are shown in Figure 3.12. Similar to the results in Figure 3.2, TraPPE–UA yields $C_{p,\mathrm{res}}$ values that are larger than those of EXP-6 and OS 12-6 models for densities larger than $\rho_\mathrm{r} = 2.00$. The similarity in behavior between EXP-6 and

OS 12-6 models at this elevated temperature is consistent with the results obtained for derivative properties at $T_\mathrm{r} = 1.1$. All three models predict maxima and minima in $C_{p,\mathrm{res}}$ at 777.5 K, suggesting that C_p minima are not unique to Lennard-Jonesium. Furthermore, the location of the three predicted minima are in good agreement with the results of Yigzawe, where the minima predicted in this work were found at densities between 2.4ρ_c and 2.6ρ_c.

Derivative properties other than C_p, such as C_V, do not exhibit maxima around the critial density at such high reduced temperatures. However, the extrema observed for C_p at 777.5 K indicates that other properties may also exhibit non-monotonic behavior. Properties determined from Equations 3.14,3.15, and 3.16 were examined for features associated with the predicted C_p minima. While C_V and ω yield monotonic behavior for all three models, the inset in Figure 3.13 shows that a minimum in μ_JT is predicted at $\rho_\mathrm{r} =$ 2.6. Similar to C_p minima, μ_JT minima are quite shallow and can be easily overlooked. The existence of μ_JT minima does not preclude a second sign inversion (crossing $\mu_\mathrm{JT} = 0$) at higher densities, yet it remains to be seen whether such an inversion may be possible either for other models or different conditions. Similar to $C_{p,\mathrm{res}}$, β_p was also found to exhibit a maximum near the critical density yet no minimum was found near $\rho_\mathrm{r} = 2.6$. Given the monotonic behavior found for μ_{JT} near the critical density and the form of Equation 3.15, it seems the peaks in C_p and β_p have a cancellation effect near ρ_c, whereas the existence of a minimum only in C_p allows for a minimum in μ_{JT}.

3.4 Conclusions

Thermodynamic derivative properties have been determined from Monte Carlo simulations in the canonical and the isobaric-isothermal ensembles for various n-butane models at $T =$ 467.5 K ($T/T_\mathrm{c} \approx 1.1$) over a wide range of densities and pressures, respectively. The simulations demonstrate that all models qualitatively predict the characteristic non-linear behavior in the vicinity of the critical point, such as a maximum in the heat capacities and a minimum in the speed of sound, whereas commonly used equations of state miss these features. Analysis of radial distribution functions reveals that a structural transition from a gas-like fluid at low densities to a liquid-like fluid at higher densities coincides with the extrema in derivative properties at near-critical densities, while features such as C_V minima coincide with the onset of fluid compression at high densities. Although most models yield the correct qualitative trends, the simulations indicate that quantitative agreement with experiment depends on an intricate interplay of molecular shape and steepness of the

repulsive interactions. This finding places significant constraints on adjustments that can be made in the repulsive part of equations of state.

Simulations have also been carried out at $T = 777.5$ K using the TraPPE–UA, OS 12-6, and EXP-6 models. At this elevated temperature, the simulation data confirm the existence of a minimum in C_p, which has been recently reported by Sadus and co-workers for Lennard-Jeonesium. Moreover, a minimum in the Joule-Thomson coefficient is found at precisely the same density, suggesting both minima share the same physical basis. In addition to providing new observations for derivative properties, these results demostrate the overall robustness and reliability of Monte Carlo simulations as a predictive modeling tool and as a guide for equation of state development.

Chapter 4

Modeling Double Retrograde Vaporization with Molecular Simulations and Equations of State

4.1 Introduction

Natural gas is currently one of the world's primary fossil fuel resources, and it is expected to continue its role as a premium fuel for the immediate future.[5,11,128] In comparison to oil or coal, natural gas burns cleanly, causing a lower impact on environmental pollution.[129] Furthermore, the use of natural gas fuels has substantially increased in recent years, particularly as more power plants and motor vehicles use them to replace their traditional fuel sources (i.e. coal and gasoline).[5] However, as depletion of readily accessible reserves continues to increase, the need to obtain natural gas from unconventional resources will become more and more prominent.[6] One example is shale gas, which has become a major source of natural gas in the US within the last decade, and is expected to provide over 45% of its natural gas supply by 2035.[4] Therefore, it is important to develop fundamental understanding of natural gas at unusual conditions.

Although the most abundant component in natural gas is methane, other hydrocarbons constitute a variable fraction of the mixture. These hydrocarbons include parrafins, olefins, and aromatics, among others.[130] Most of these hydrocarbons are valuable commodity petrochemicals, such as butanes and benzene derivatives.[131] Because of its composition, natural gas exists as an asymmetric supercritical mixture under typical reservoir

conditions.[132] Therefore, temperature or pressure drops during production can cross the vapor-liquid coexistence boundary, causing heavy components phase separate in the form of liquid droplets.[133] This liquid dropout is problematic because condensates may remain trapped within the geologic formations as a consequence of their low mobility, leading to productivity losses.[7] Furthermore, liquid droplets may accumulate within transmission lines, causing operational problems due to flow blockage.[134] Experimental PVT analyses of natural gas at reservoir conditions can be quite costly, and are often difficult to perform.[135] Hence, there is a need to reliably predict the condensation behavior of natural gases for efficient process design.

Development of thermodynamic models for prediction of phase behavior has been the focus of much research. While supercritical and near-critical fluids have been studied extensively for a multitude of applications,[136–138] the phenomenon of double retrograde vaporization (DRV) has been rarely observed. This phenomenon is characterized by a retrograde dew point curve at mixture compositions approaching nearly pure low-boiling compound for isotherms very close to its critical temperature, rendering an "S-shaped curve.[139,140] Chen $et\ al.$ showed this highly nonlinear behavior for mixtures of methane with n-butane[141] and n-pentane,[142] where triple- and quadruple-valued dew points were reported for a narrow concentration range. Although the phenomenon has since been studied experimentally for other near-critical mixtures, accurately modeling DRV has attracted attention for its potential applications in oil field operations and pipeline design. Modeling DRV also has potential applications in separations processes such as supercritical fluid extraction, where it has been proposed as a mechanism for increasing extraction efficiency by enhancing selectivity without the loss of yield.[143] To improve modeling performance, fundamental understanding of DRV also needs to be improved.

Computational studies on DRV have generally centered on using of equations of state (EoS) to obtain quantitative descriptions of phase equilibria, relying on volumetric property estimates for analysis. While they are fast and effective in correlating known experimental data, they are often unable to provide reliable predictions at high temperatures and pressures, and particularly at near-critical conditions. Molecular simulation, though relatively more computationally intensive, has proven to be an excellent tool for exploring complex systems at the molecular level. Among existing molecular simulation methods, the Gibbs ensemble Monte Carlo (GEMC) method introduced by Panagiotopoulos[57,67] has been widely used for the prediction of fluid phase equilibria. By making use of advances simulation strategies, such as Configurational-bias Monte Carlo[60,61,66] (CBMC), GEMC

simulation performance can be enhanced and simulations under challenging constraints, as is the case for DRV, can be feasibly carried out. Hence, the goal of this work is to investigate the performance GEMC simulations for predicting DRV. Emphasis is given to binary mixtures of methane + n-butane, which serve as a model for fluid mixtures in gas condensate reservoirs. This approach allows for exploration of the molecular level details inherent to DRV, providing much needed support for the development of advanced EoS.

4.2 Computational Details

4.2.1 Monte Carlo Simulations

The MCCCS-MN program[74] was used to perform GEMC simulations for binary mixtures methane and n-butane. The interactions of these alkanes were described using the united-atom version of the transferable potentials for phase equilibria (TraPPE–UA) force field,[69] which treats each CH_x unit as a single interaction site. Non-bonded interactions are described using Lennard-Jones (LJ) and Coulomb potentials:

$$U\left(r_{ij}\right) = 4\epsilon_{ij}\left[\left(\frac{\sigma_{ij}}{r_{ij}}\right)^{12} - \left(\frac{\sigma_{ij}}{r_{ij}}\right)^{6}\right] + \frac{q_i q_j}{4\pi\epsilon_0 r_{ij}} \tag{4.1}$$

where r_{ij}, σ_{ij}, ϵ_{ij}, q_i, q_j and ϵ_0 are the distance between interaction sites i and j, the LJ diameter and well depth, the partial charges on interaction sites i and j, and the permittivity of vacuum, respectively. Intramolecular degrees of freedom are governed by a fixed C–C bond length, a harmonic angle bending potential, and a cosine series torsional potential. Non-bonded interactions were truncated using a 1.4 nm spherical cutoff, and analytical tail corrections were employed.[54] Lorentz-Berthelot combining rules[99] were used to obtain the LJ parameters for interactions between different bead types:

$$\begin{aligned}\sigma_{\mathrm{ij}} &= \frac{1}{2}\left(\sigma_{\mathrm{i}} + \sigma_{\mathrm{j}}\right)\\ \epsilon_{\mathrm{ij}} &= \sqrt{\epsilon_{\mathrm{i}}\epsilon_{\mathrm{j}}}\end{aligned} \tag{4.2}$$

Vapor pressures of neat methane were computed at three different temperatures: 184.47 K, 192.24 K, and 193.20 K. These correspond to reduced temperatures of 0.95, 0.990, and 0.995, where the term “reduced” denotes a corresponding state with respect to the critical temperature of TraPPE–UA methane. This critical temperature and critical pressure of TraPPE–UA methane were obtained from the result of a finite-size scaling study of Potoff

and Panagiotopoulos for Lennard-Jonesium,[102] which yields $T_{\mathrm{c,\ CH4}} = 194.17$ K and $p_{\mathrm{c}} = 50.36$ bar at the infinite system size limit. The computed vapor pressures were used as the upper boundary for binary phase diagrams at temperatures below the critical point of methane. Vapor pressures were computed using NVT-GEMC simulations with a system size of 5000 methane molecules. In addition to overcoming system size effects, this relatively large number of molecules was chosen to suppress the strong fluctuations associated with proximity to the critical point. At each temperature, simulations were run for a production period of 200,000 MC cycles (1 MC cycle = N moves, where N is the total number of particles), and averages were computed using 8 independent simulations.

Pressure-composition ($p-x-y$) phase diagrams for the methane/n-butane binary system were generated using GEMC simulations in the isobaric-isothermal ensemble (NpT-GEMC). A total of six temperatures were simulated: 184.47 K, 192.24 K, 193.20 K, 195.15 K, 196.10 K, and 203.88 K. In reduced units, these temperatures cover a range between 0.95 and 1.05. The total number of molecules was fixed at 5500, where at least 5000 of these were methane molecules. The remaining number of molecules was adjusted so as to yield overall compositions within phase coexistence boundaries. Averages were taken from 8 independent simulations, each consisting of a production period of 50,000 MC cycles in length. To optimize sampling efficiency, volume change and particle transfer moves were adjusted so as to yield 1 accepted move of each type per MC cycle.[110] While particle translations were allowed for both molecules, CBMC regrowths and rotation moves were only applied to butane molecules.

A wealth of fluid properties are simultaneously generated in GEMC simulations for both coexising phases. Previous work on modeling DRV has focused on understanding the high degree of nonlinearity in volumetric properties. To assess these features, number densities were analyzed for each component in each phase as a function of the system pressure. This allows for a detailed view of the volumetric effects associated with DRV phase behavior. Based on this direct determination of partitioning between liquid and vapor phases,[144] Gibbs free energies of transfer (ΔG_t) were computed directly from the average number densities in each phase using Equation 4.3, where $\rho_{t,\mathrm{liq}}$ and $\rho_{t,\mathrm{vap}}$ denote number densities of molecule type t in liquid and vapor phases, respectively.

$$\Delta G_t = -RT \ln \left(\frac{\rho_{t,\mathrm{liq}}}{\rho_{t,\mathrm{vap}}} \right) \tag{4.3}$$

Free energies were analyzed as a function of system pressure, providing information on the driving forces of alkane partitioning across various state points. Structural features

were analyzed by computing center-of-mass radial distribution functions (RDF) and their respective number integrals for the liquid phase, allowing for direct insight into molecular packing variations.

4.2.2 Equations of State

Equations of state provide a mathematical formalism that interrelates temperature, pressure, volume, and composition of a fluid. Most of the EoS used in chemical thermodynamics are written as pressure explicit expressions. Once the EoS is solved for volume (or equivalently for density), primary and derivative thermodynamic properties can be calculated using simple analytic equations.[145] In this work, one of the most widespread EoS in industry and academia, the Peng-Robinson[27] equation of state (PR EoS), is used to calculate the phase equilibria of systems that exhibit retrograde condensation behavior. The pressure explicit expression for PR EoS is:

$$p = \frac{RT}{V-b} - \frac{a\alpha(T)}{V(V+b)+b(V-b)} \tag{4.4}$$

where R is the gas constant while a,b, and $\alpha(T)$ are component-specific constants that account for the attractive intermolecular interactions, hard core volume of the fluid, and the corresponding state of the system. These are calculated from pure fluid critical properties using:

$$\begin{aligned} a &= 0.45724\frac{R^2T_{\mathrm{c}}^2}{P_{\mathrm{c}}} \\ b &= 0.07780\frac{RT_{\mathrm{c}}}{P_{\mathrm{c}}} \\ \alpha(T) &= [1+(0.37464{+}1.54226\omega - 0.26992\omega^2)(1-\sqrt{T_r})]^2 \end{aligned} \tag{4.5}$$

Values for T_{c}, P_{c}, and acentric factor (ω) are given int Table 4.1 for the components studied in this work. For flash calculations, the standard one-fluid van der Waals mixing rules were used,[146] with a single temperature independent binary interaction parameter, k_{ij}:

$$\begin{aligned} a\alpha(T) &= \sum_{i=1}^{c}\sum_{j=1}^{c} x_i x_j \sqrt{(a\alpha)_i (a\alpha)_j}(1-k_{ij}) \\ b &= \sum_{i=1}^{c} x_i b_i \end{aligned} \tag{4.6}$$

Fitting the k_{ij} parameter against experimental data allows reliable extrapolation of the calculations within a wide temperature range. However, the focus of this work is to investigate DRV from a predictive modeling standpoint and, therefore, calculations using non-zero k_{ij} parameters were not emphasized. Predictive estimates from PR EoS were used to guide the set up of GEMC simulations at high pressures, providing appropriate values for overall compositions, volumes, and pressures to be used.

In addition to PR EoS, the performance of the perturbed-chain statistical associating fluid theory[40] (PC-SAFT) was investigated with respect to modeling DRV. The theoretical foundations of the SAFT[34,35,147,148] models lie on Wertheim's first order perturbation theory,[36–39] where free energy perturbations are applied to that of a simple reference fluid. Therefore, the PC-SAFT EoS is generally expressed as a summation of residual Helmholtz free energy terms, A^{res}, that account for different molecular interactions in the system under study. The residual Helmholtz free energy accounts for departure from the free energy of an ideal gas at the same temperature and density. This term is given by:

$$\begin{aligned}\frac{A^{res}(T,\rho)}{NRT} = \frac{a^{res}(T,\rho)}{RT} &= \frac{a(T,\rho)}{RT} - \frac{a^{ideal}(T,\rho)}{RT} = \frac{a^{ref}(T,\rho)}{RT} + \frac{a^{disp}(T,\rho)}{RT} \\ &= \frac{a^{hs}(T,\rho)}{RT} + \frac{a^{chain}(T,\rho)}{RT} + \frac{a^{disp}(T,\rho)}{RT} + \frac{a^{assoc}(T,\rho)}{RT}\end{aligned} \tag{4.7}$$

where the superscripts $res, ideal, ref, hs, chain, disp,$ and $assoc$ refer to residual, ideal, reference, hard sphere, chain, dispersion, and association terms, respectively. The exact formalism of PC-SAFT developed by Gross and Sadowski[40] was used in this work. In contrast to the original SAFT formulation, PC-SAFT uses a hard chain as its reference fluid, as opposed to the simple hard sphere fluid of SAFT. This modification allows for better description of the chain length dependence of the attractive and repulsive interactions between molecules.

For non-associating components, PC-SAFT requires three parameters for each pure component: the number of segments, m, in the chain molecule, the chain segment diameter, σ_{i}, and the energy of dispersion interactions between segments, ϵ_{i}. Two more parameters are included to account for association interactions for pure components: the association energy between sites of like molecules, $\epsilon^{A_{\mathrm{i}}B_{\mathrm{i}}}$, and the volume of association, $\kappa^{A_{\mathrm{i}}B_{\mathrm{i}}}$. These parameters are fitted to experimental vapor pressure and saturated liquid density from low temperature up to close to the critical point. Table 4.1 provides PC-SAFT parameter values for the components used in this work.

PC-SAFT is extended to mixtures by introducing σ_{mix} and ϵ_{mix} that are evaluated by the following mixing rules that are derived from van der Waals one-fluid theory:

Table 4.1: Pure component parameters for PR EoS[31] and PC-SAFT.[40]

	PC-SAFT			PR EoS		
Compound	m	σ [Å]	ϵ/k_{B} [K]	T_{c} [K]	P_{c} [MPa]	ω
Methane	1.0000	3.7039	150.03	190.56	4.599	0.0115
n-Butane	2.3316	3.7086	222.88	425.12	3.796	0.2002

$$\begin{aligned} \sigma_{\mathrm{mix}}^3 &= \frac{\sum_{i=1}^{c}\sum_{j=1}^{c} x_i x_j m_i m_j \sigma_{\mathrm{ij}}^3}{(\sum_{i=1}^{c} x_i m_i)^2} \\ \epsilon_{\mathrm{mix}}\sigma_{\mathrm{mix}}^3 &= \frac{\sum_{i=1}^{c}\sum_{j=1}^{c} x_i x_j m_i m_j \sigma_{\mathrm{ij}}^3 \epsilon_{\mathrm{ij}}}{(\sum_{i=1}^{c} x_i m_i)^2} \end{aligned} \tag{4.8}$$

Dispersion interaction parameters were calculated using Lorentz-Berthelot combining rules, where similar to PR EoS a temperature independent k_{ij} parameter is included:

$$\begin{aligned} \sigma_{\mathrm{ij}} &= \frac{1}{2}\left(\sigma_{\mathrm{i}} + \sigma_{\mathrm{j}}\right) \\ \epsilon_{\mathrm{ij}} &= \sqrt{\epsilon_{\mathrm{i}}\epsilon_{\mathrm{j}}}\left(1 - k_{\mathrm{ij}}\right) \end{aligned} \tag{4.9}$$

Similarly, fitting the k_{ij} parameter against experimental data is used for reliably correlating experimental data within valid temperature and pressure ranges, as opposed to predictive estimates where $k_{\mathrm{ij}} = 0$. Flash calculations based on robust algorithms[149,150] were performed in this work. EoS predictions are compared directly with GEMC simulations and with limited experimental data. Along with phase equilibria calculations, the number density of each component in both liquid and vapor phases, as well as the free energy of transfer are calculated and directly to compared with molecular simulation calculations.

4.3 Results and Discussion

4.3.1 Dew Curves

While the main focus of this work is based on investigating dew points around the critical point, it is important to first analyze the full phase diagram for all methods tested, including bubble point predictions from all models. Figure 4.1 shows the $p - x - y$ diagram for six isotherms near the critical point of methane($T_{\mathrm{c,\ CH4}}$). These results show that both EoS

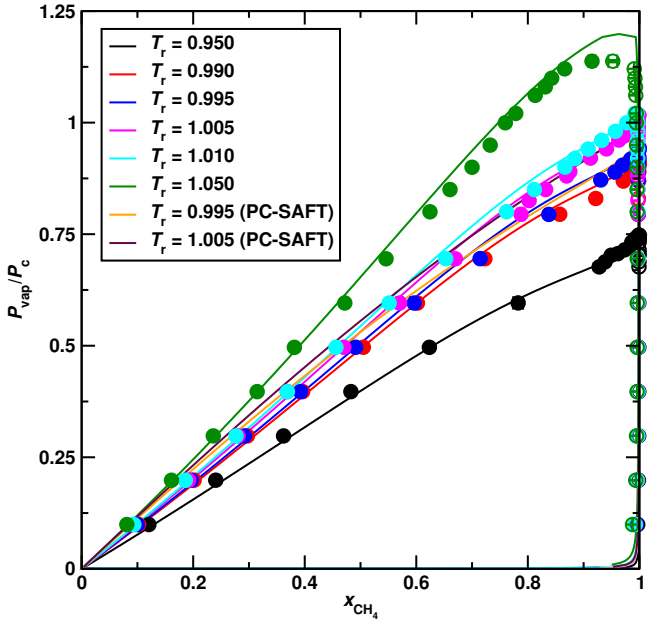

Figure 4.1: Pressure-composition diagram for the system methane + n-butane determined from GEMC simulations (circles) and EoS (solid lines). Solid lines and filled circles denote bubble points, dashed lines and open circles denote dew points. Color scheme is equivalent for PR EoS and GEMC. Error bars computed as the standard error of the mean.

and simulation methods yield very similar dew point and bubble point curves at the selected temperatures. More importantly, by projecting VLE data in reduced units (with respect to each models respective critical properties), such that all methods are properly compared at the same corresponding state, excellent agreement is attained. Such agreement suggests that other properties from simulations and EoS should likewise be directly compared in reduced units of temperature and pressure.

Due to the asymmetric nature of this system, the dew curves at the selected temperatures are very close to the pure methane axis for most of the pressure range. Therefore, to observe the expected retrograde behavior at these conditions, analyzing the phase diagram at nearly pure methane composition is required. This is shown in Figures 4.2 and 4.3. These plots indicate that both EoS and molecular simulations clearly capture DRV behavior of the methane/n-butane binary system, yielding dew curve shapes that very much resemble the experimental measurements of Chen $et\ al.$[141] At temperatures below $T_{\mathrm{c,\ CH4}}$

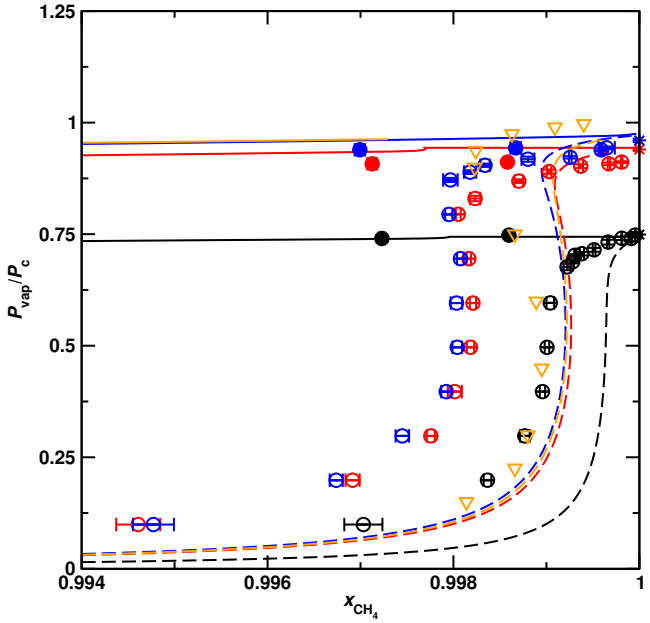

Figure 4.2: Subcritical isotherm dew curves at compositions approaching pure methane. Notation defined in Figure 4.1. Triangles denote experimental dew points[141] at T_r = 1.0001 and stars denote pure methane vapor pressures.

the calculated curves exhibit an "S-shape", similar to the experimental dew curve at $T_r = 1.0001$. At $T_r = 1.005$ and $T_r = 1.01$, which are just slightly above $T_{c,\,CH4}$, the calculated curves also show a double bend at high pressures, similar to double-domed dew curves previously reported by Raeissi and Peters,[139,151] where quadruple-valued dew points exist in a narrow range of dilute concentrations. For the GEMC curves, these high-pressure dew points show larger error bars than those at lower pressures due to their proximity to the mixtures critical point. In addition, the number of butane molecules at these conditions is very low and, therefore, a single particle transfer move causes a relatively large deviation from the equilibrium compositions in each phase. While previous studies have also used PC-SAFT[152] and PR EoS[153] to estimate DRV in methane-butane mixtures, Figures 4.2 and 4.3 provide evidence that GEMC simulations are capable of accurately predicting DRV as well. Moreover, both GEMC and EoS results also agree with the experimental data at $T_r = 1.05$, where the system exhibits a familiar supercritical behavior (inverted "C-shaped"

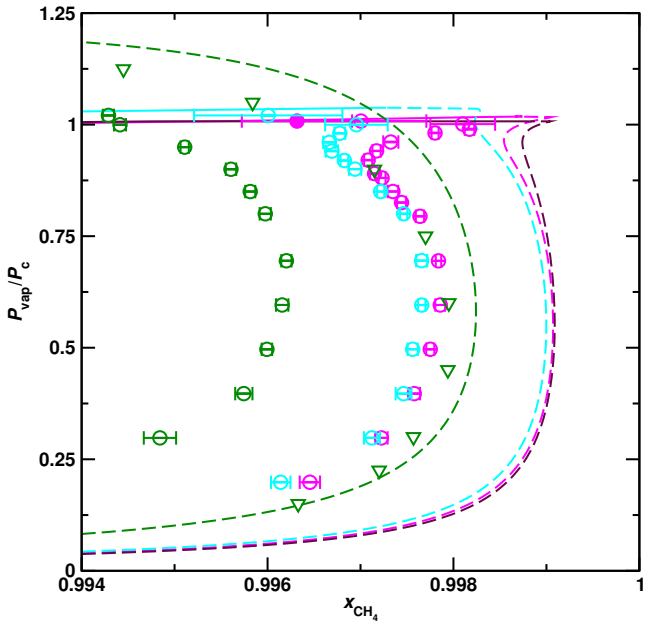

Figure 4.3: Supercritical isotherm dew curves at compositions approaching pure methane. Notation defined in Figure 4.1. Triangles denote experimental dew points[141] at T_r = 1.0489.

dew curves). This result indicates that GEMC simulations also correctly predict the continuous transition between subcritical and supercritical phase behavior. However, there are a few subtle differences between calculated and experimental results. The dew curves obtained from molecular simulations are slightly "shifted" towards higher butane concentrations with regards to the EoS and experimental dew curves, though only by a very small composition difference (note the scale of the composition axis). This shift in composition is addressed in Section 4.3.5. Both PC-SAFT and PR EoS also estimate dew curves with a less pronounced retrograde in comparison to experiment and GEMC simulation. Despite these slight differences, the results confirm that both GEMC simulations and EoS are capable of accurately capturing DRV behavior.

4.3.2 Number Densities

To investigate the influence of DRV on volumetric properties in this system, number densities from both GEMC and EoS were analyzed. As shown in Figures 4.4 and 4.5, the

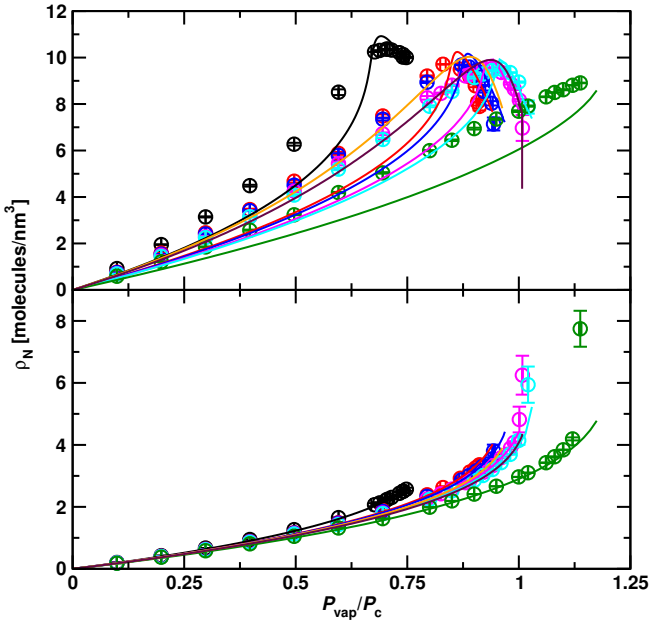

Figure 4.4: Number density of methane in liquid (top) and vapor (bottom) phases as a function of pressure. Notation defined in Figure 4.1.

number densities have considerably different trends for each component in each phase as pressure is increased. The number density of methane in the liquid phase shows substantial increases at temperatures where DRV occurs. This sudden increase in methane densitiy indicates that the liquid phase becomes "swelled" with methane at high pressures. As noted by Raeissi and Peters,[139] the dew curve bend at high pressures is associated with an increase in the isothermal compressibility of the low-boiling compound. Hence, the liquid phase becomes "swelled" as methane becomes increasingly compressible near its critical point. For this reason, the bend observed in these number densities occurs in the same pressure range as where the dew curves show a high-pressure bend, and it gradually becomes less pronounced as the temperature is increasingly farther away from $T_{\mathrm{c,\ CH4}}$. At $T_{\mathrm{r}} = 1.05$, the number density monotonically increases with pressure and the dew curve "S-shape" is no longer observable due to a lack of methane swelling. Although the dew curve retrograde has an effect on the number density of methane in the liquid phase, it seems to have no pronounced impact on its vapor phase counterpart. The vapor phase number density increases monotonically with pressure at all temperatures, with

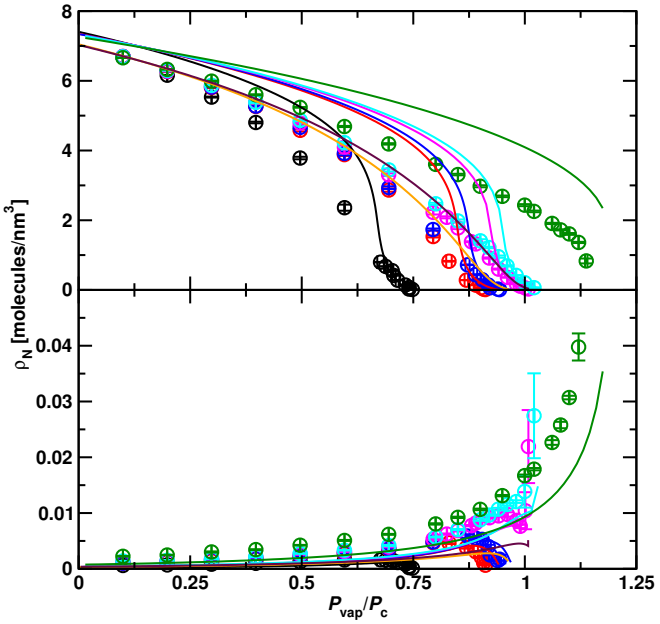

Figure 4.5: Number density of butane in liquid (top) and vapor (bottom) phases as a function of pressure. Notation defined in Figure 4.1.

only a sharper increase at higher pressures. Agreement between GEMC and both EoS is very good in the vapor phase, while in the liquid phase the PC-SAFT curves resemble the GEMC curves better than does PR-EoS, a consequence of PC-SAFTs higher order. In general terms, however, the number density estimates from PR-EoS for both phases agree well with those in GEMC simulations.

Despite the unusual behavior in the liquid phase number density of methane, the overall increase is coupled with a gradual depletion of liquid phase butane, shown in Figure 4.5. As with methane, this trend in liquid phase number density of butane is well described by simulation and both EoS, where PC-SAFT best resembles the GEMC curves. Just as the PR EoS estimates a sharper methane “swelling” in the liquid phase, it also estimates a sharper decrease in the liquid phase number density of butane. Although the average overall composition of butane decreases with pressure, an increase in the vapor phase number density of butane is observed within the same pressure range where the liquid phase “swells” with methane. Therefore, there exists a link between the increases in the liquid phase number density of methane and the vapor phase number density of butane.

The number density increase in the latter quickly falls to zero for subcritical isotherms as the system approaches pure methane composition, and the "double-dome behavior observed for supercritical dew curves slightly above $T_{\mathrm{c,\ CH4}}$ is observed in the number densities as well. A monotonic increase in the vapor phase number density of butane at $T_{\mathrm{r}} = 1.05$ is observed as expected, since this isotherm exhibits typical supercritical phase behavior where butane composition in the vapor phase increases at higher pressures. The trends for butane in the vapor phase are also well described by both EoS, and the GEMC simulations predict them accurately as well despite the increased uncertainty within proximity of critical points. The predicted vapor phase densities of butane are larger for GEMC, which is expected given the dew curve shift shown in Figures 4.2 and 4.3.

4.3.3 Free Energies of Transfer

Due to the direct relationship between number densities and free energy of transfer, DRV behavior is also reflected in the latter. Figure 4.6 shows the calculated free energies

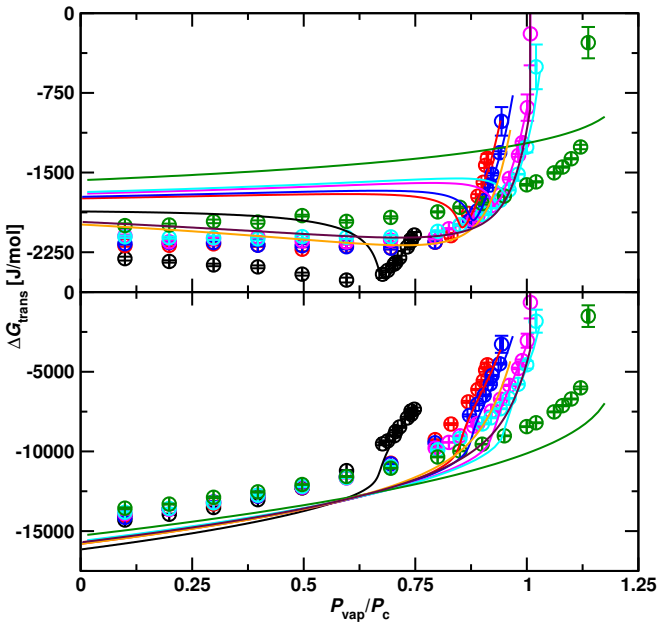

Figure 4.6: Free energies of transfer for methane (top) and butane (bottom) as a function of pressure. Notation defined in Figure 4.1.

of transfer for each component using Equation 4.3. Similar to the number densities, the variations in composition observed in Figures 4.2 and 4.3 are also reflected in the free energies of transfer for both components. For methane, the energy varies slightly from low to moderate pressures, whereas a sharp change in free energy is observed at high pressures. This sudden change in trend occurs within the same pressure range where DRV is observed, and becomes more pronounced as the number densities of methane in each phase become increasingly similar. The sharp decrease in the magniture of $\Delta G_{\mathrm{trans}}$ for methane indicates that there is a lower change in free energy when methane molecules transfer between phases that become increasingly similar (i.e. from an increasingly compressible liquid phase to a relatively dense vapor phase). $\Delta G_{\mathrm{trans}}$ is roughly an order of magnitude larger for butane, indicating that butane molecules that transfer to the vapor phase undergo a large change in free energy. However, the non-linear variations observed in the vapor phase number densities of butane do not yield similar non-linear trends in its free energy of transfer. This is because the number density of butane in the vapor phase is about two orders of magnitude smaller than its liquid phase counterpart and, hence, vapor phase density variations are not sufficiently large to be reflected in the free energies. Therefore, the behavior of the free energy of transfer for butane is dominated by the increasing similarity in the number density of butane in both phases.

Although GEMC simulations and both EoS describe the a similar general trend, the PR EoS estimates a sharper drop in free energy, whereas PC-SAFT results closely resemble those from GEMC simulations. This is expected due to better agreement between PC-SAFT and GEMC simulations for number densities as well. This is also the case for the free energy of butane, where PC-SAFT and GEMC simulations yield smoother changes free energy compared to PR EoS. Overall, both EoS and GEMC simulations predict similar variations in free energies of transfer for both components, where changes associated with DRV are observed.

4.3.4 Structural Analysis

The capability of providing molecular-level information for fluid systems has long been recognized as one of the major advantages of computer simulations. To further understand DRV, center of mass radial distribution functions (RDF) were generated to address molecular-level packing across multiple state points. While RDFs can provide details on the molecular structure of both liquid and vapor phases, emphasis is given here to the liquid

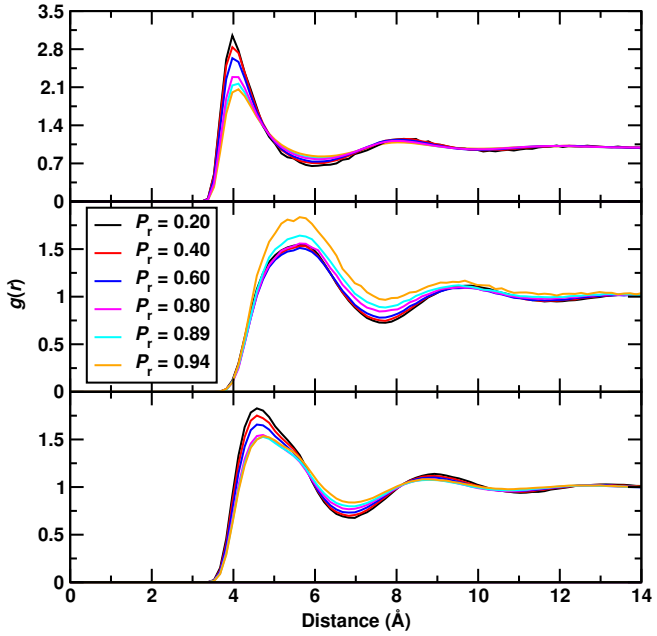

Figure 4.7: Liquid phase CH_4-CH_4 (top), C_4H_{10}-C_4H_{10} (middle), and CH_4-C_4H_{10} (bottom) radial distribution functions at various reduced pressures for mixtures at T_r = 1.005.

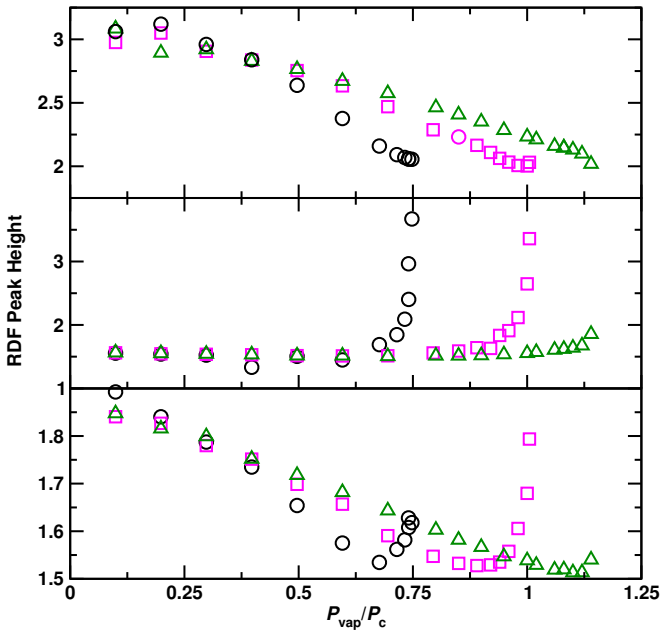

Figure 4.8: Liquid phase CH_4-CH_4 (top), C_4H_{10}-C_4H_{10} (middle), and CH_4-C_4H_{10} (bottom) RDF peak heights of the first solvation shell as a function of reduced pressure. Color scheme defined in Figure 4.1.

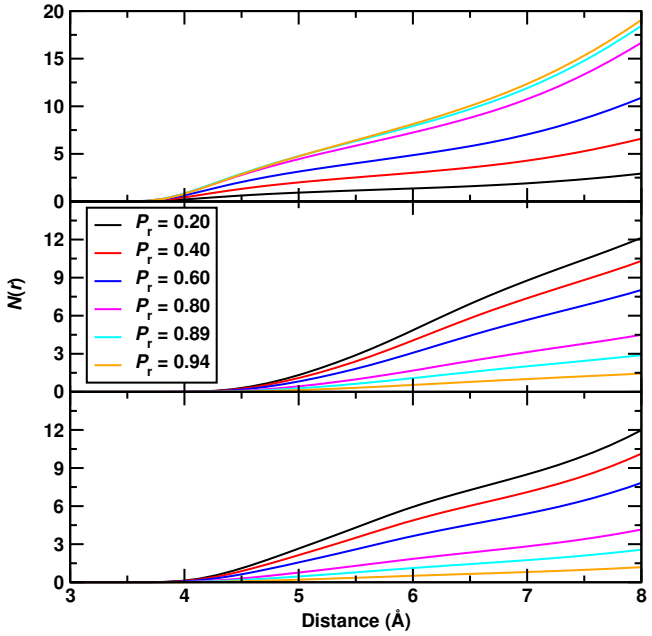

Figure 4.9: Liquid phase CH_4-CH_4 (top), C_4H_{10}-C_4H_{10} (middle), and CH_4-C_4H_{10} (bottom) number integrals of the first solvation shell at various reduced pressures for mixtures at T_r = 1.005.

phase RDFs. Figure 4.7 shows the liquid phase RDFs between similar and different pairs of molecules for various pressures at $T_\mathrm{r} = 1.005$, where variations in peak heights can be observed for different vapor pressures. The evolution of peak heights is linked to density variations due to packing changes that ocurr as the system approaches the critical point. For clarity, the evolution of peak heights in the first solvation shell are shown as a function of pressure in Figure 4.8 for three isotherms. The peak height of CH_4-CH_4 RDFs decrease as the system approaches its saturated vapor pressure, which is consistent with the loss of structure associated with increasing proximity to the critical point of methane. Comparing the peaks for methane between similar and different pairs, it is evident that increasing pressure lowers the peak height in both, but only the RDFs between different pairs show a sharp increase at the high-pressure end, an indication that butane molecules increasingly populate the liquid phase as the vapor phase approaches pure methane composition. This effect is also reflected in C_4H_{10}-C_4H_{10} RDF peaks, which only increase sharply at high

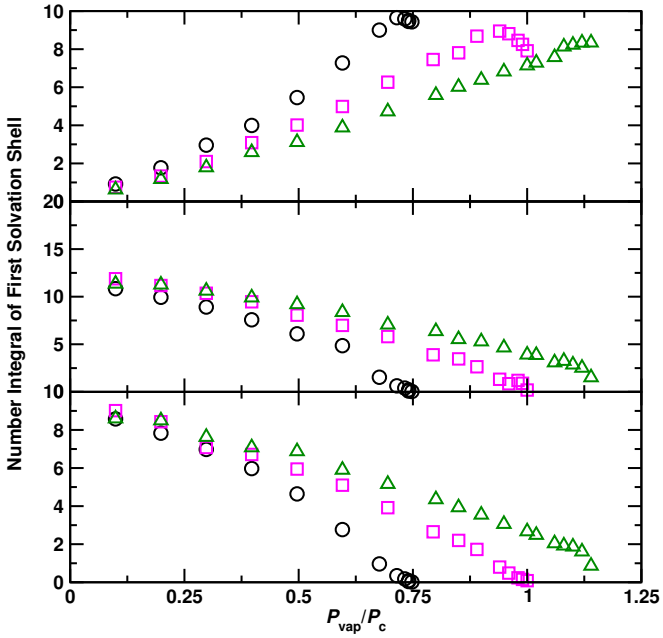

Figure 4.10: Liquid phase CH_4-CH_4 (top), C_4H_{10}-C_4H_{10} (middle), and CH_4-C_4H_{10} (bottom) number integrals of the first solvation shell as a function of reduced pressure. Color scheme defined in Figure 4.1.

pressures, yet with lower magnitude given the low amount of butane molecules in the system. These trends suggest that the structural effects of DRV are observable within the length scale of the the first solvation shell.

In addition to RDF peak evolution, the number integrals were computed at multiple state points. Figure 4.9 shows the number integrals for the RDFs from Figure 4.7, and their evolution as a function of pressure is shown in Figure 4.10 for the first solvation shell. The evolution of the CH_4-CH_4 number integrals closely resembles the shape of the liquid phase number density plots of CH_4. This confirms that the methane "swelling" effect is observable within the first solvation shell. Hence, the local environment around a methane molecule directly influences the shape of the dew curves, where CH_4-CH_4 packing arrangements that pack more methane molecules into the first solvation shell are observed for pressures where the liquid phase becomes "swelled" with methane. Similarly, the CH_4-C_4H_{10} and C_4H_{10}-C_4H_{10} number integrals show a monotonic decrease with increasing pressure,

which is simply due to decreasing amounts of butane in the system. Hence, these number integrals confirm that variations in composition and density are directly correlated with molecular packing, showing a tight packing of the low-boiling compound at high pressures.

4.3.5 Effect of Butane Vapor Pressure

The dew curves computed from GEMC simulations shown in Figures 4.2 and 4.3 are systematically shifted towards higher butane mole fractions in comparison to experimental measurements and EoS predictions, suggesting that the amount of butane in the vapor phase is overestimated by the TraPPE–UA n-butane model. To address this observation, the butane model was modified to yield vapor pressures closer to those measured experimentally at $T = 194.17$ K ($T_{\mathrm{c,\ CH4}}$ for TraPPE-UA). With this new model at hand, the binary phase diagram was then computed at $T_{\mathrm{r}} = 0.995$. ϵ parameters of both CH_2 and CH_3 pseudoatoms were simultaneously increased, effectively lowering the vapor pressure for a fixed temperature. Table 4.2 shows the vapor pressures of the modified butane models from NVT-GEMC simulations. A total of 1,000 n-butane molecules were used for each simulation, which consisted of 8 independent runs with production periods of 200,000 MC cycles.

It is important to note that 194.17 K is well below the normal boiling point of n-butane (272.66 K[113]) and, thus, the vapor pressures are quite low. The predicted vapor pressures are given in Table 4.2. These suggest that an 8% increase in ϵ is required to yield vapor

Table 4.2: Vapor pressures of TraPPE–UA n-butane with modified ϵ parameters at 194.17 K. Adjustments apply to CH_2 and CH_3 sites. Uncertainty (δp_{vap}) computed as standard error of the mean. Experimental value taken from NIST[113]

Percent increase	p_{vap} [bar]	δp_{vap} [bar]
0	0.02688	0.0005043
1	0.02419	0.0005673
2	0.02131	0.0004260
5	0.01254	0.0003546
6	0.01163	0.0004008
8	0.00903	0.0003491
9	0.00771	0.0003118
Experiment	0.00895	–

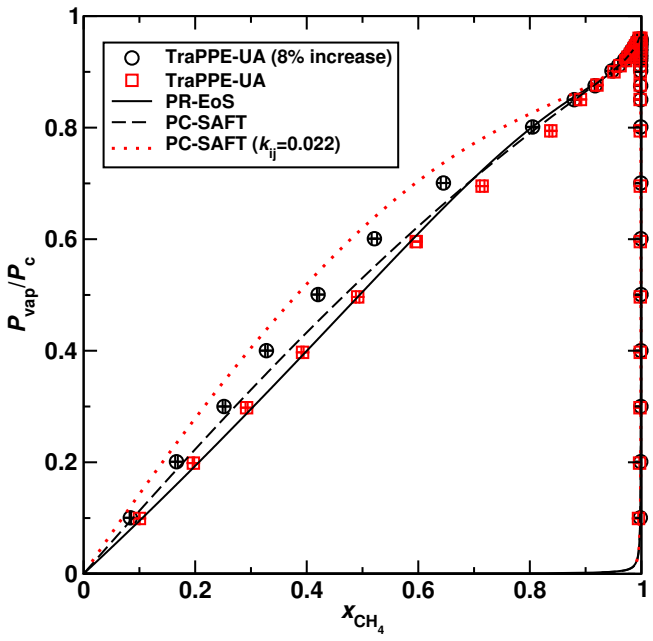

Figure 4.11: Effect of increasing ϵ parameters of butane molecules on phase diagrams at T_{r} = 0.995.

pressures similar to experimental measurements. Therefore, a modified TraPPE–UA n-butane model with 8% larger ϵ values was used to recompute the binary phase diagram. The full $p - x - y$ diagram is shown in Figure 4.11, and the corresponding dew curve is shown in Figure 4.12. In addition to GEMC simulations, binary VLE data was obtained from flash calculations using PC-SAFT with $k_{ij} = 0.022$,[40] therby providing a reliable correlation of experimental VLE data at $T_{\mathrm{r}} = 0.995$. As shown in Figure 4.12, simulations using the modified TraPPE–UA model yield dew curves that agree very well with PC-SAFT correlations. Therefore, by adjusting the vapor pressure of n-butane, GEMC simulations are able to quantitatively predict DRV. Furthermore, increasing ϵ parameters effectively increases the critical point and, therefore, the difference in critical points of the two components is enlarged, making the mixture more asymmetric. Consequently, this leads to bubble points with higher n-butane concentrations, as seen in Figure 4.11. This widening of the phase envelope also agrees very well with PC-SAFT correlations, suggesting that n-butane partitioning determines the overall "shift" in dew and bubble curves.

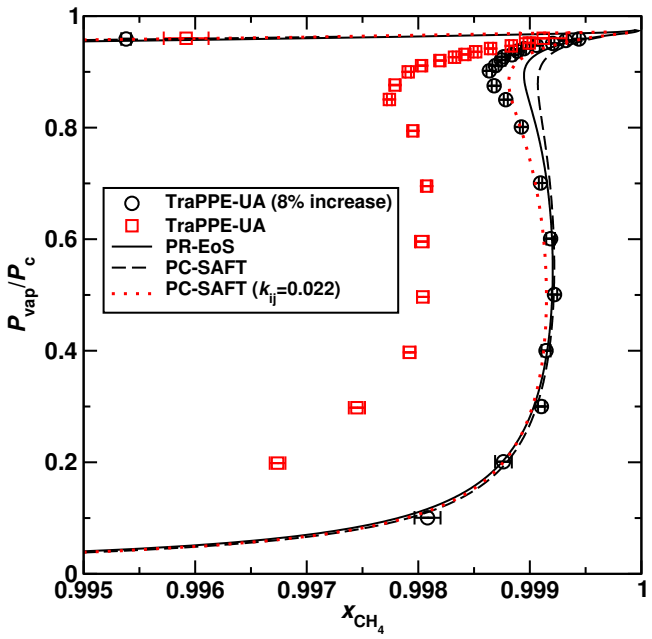

Figure 4.12: Effect of increasing ϵ parameters of butane molecules on dew curves at T_r = 0.995.

4.4 Conclusions

The phenomenon of double retrograde vaporization has been investigated for the binary system methane + n-butane. Two different methods were used in this study: equations of state and Gibbs ensemble Monte Carlo simulations. Both methods yield qualitatively similar phase behavior near the critical point low-boiling compound, where DRV was observed at the same corresponding states. By analyzing the number densities of each component in both coexisting phases, it was shown that DRV is driven by the liquid phase becoming "swelled" with the low-boiling compound, with an analagous increase in the vapor phase number density of n-butane. This effect was reflected in the free energy of transfer for methane, which showed non-linear variations with increasing pressure. Liquid phase RDFs showed that DRV is linked to the local environment around methane molecules, where molecular packing is influenced within the first solvation shell. Finally, the systematic dew curve shift towards higher n-butane mole fractions was investigating by modifying both ϵ parameters on the TraPPE–UA n-butane model. This modification

effectively lowered the amount of n-butane present in the vapor phase and shifted the dew curves towards higher methane concentrations, allowing for quantitative agreement with PC-SAFT correlations (i.e. using a non-zero k_{ij} parameter fitted to experimental VLE measurements). Overall, GEMC simulations were able to predict DRV behavior with very high accuracy, and predictions using PC-SAFT showed better agreement with simulation data in comparison to the PR EoS.

Chapter 5

Molecular Modeling of Retrograde Vaporization in Enhanced Oil and Gas Recovery

5.1 Introduction

Production of natural gas from unconventional sources has increased significantly in the US during the last several years. By 2011, over 68% of all natural gas production came from unconventional sources, such as from shale gas reservoirs.[6] Despite this production increase, understanding complex fluid behavior in these gas reservoirs is required to further improve gas production and processing. For example, methane, the primary component in natural gas, is found in its supercritical state under typical gas reservoir conditions, which could be as high as 450 K and 100 MPa.[132] However, heavy hydrocarbons present in the reservoir are subcritical, forming asymmetric mixtures with methane that can exhibit retrograde condensation behavior. This phase behavior is particularly problematic in rich gas condensate wells, where liquid dropout within transmission lines hinders production due to interruption of gas flow.[131] On the other hand, condensate droplets rich in heavy hydrocarbons can also form within the geologic matrix, becoming difficult to recover due to reduced liquid mobility from capillary forces which can lead to potentially unfeasible recoveries.[133] To prevent hydrocarbon losses, tertiary recovery methods are often used to extract these hydrocarbons and increase recovery factors in gas condensate reservoirs.

Miscible and immiscible gas injection has become a popular enhaced oil recovery

(EOR) method for recovery of hydrocarbons that remain stranded in oil and gas reservoirs. This method is particularly effective when combined with other recovery strategies, such as in water-alternating-gas (WAG) processes.[16] During gas injection, pressurized gases are injected into the reservoir to improve microscopic displacement efficiency by either fully or partially dissolving into, and thereby swelling, the residual oil.[10,15] By lowering the viscosity of residual oil, mobility is improved such that oil droplets can be displaced and flow towards the producing well. Common gases used for injection processes include hydrocarbon gases originally associated with the residual oil, CO_2, and mixtures of these.[15] Injecting CO_2 is an attractive option because a significant fraction remains in the reservoir, and any additional CO_2 that is produced can be pressurized and reinjected for storage.[154] Storing CO_2 during EOR can offset carbon dioxide emissions from consumption of recovered hydrocarbons. Moreover, at a CO_2:oil mass ratio of approximately 3:1, the amount of CO_2 injected matches the amount produced when the recovered hydrocarbons are burnt, suggesting carbon neutral EOR processes could be designed.[155] Understanding phase behavior in oil and gas reservoirs is therefore of primary importance to improve the performance of EOR processes.

Under typical oil and gas reservoir conditions, fluid mixtures may exhibit an interesting yet scarcely studied phenomenon known as double retrograde vaporization (DRV). Mixtures that exhibit DRV are characterized by highly non-linear phase behavior at conditions in the vicinity of the critical point of the low-boiling compound. This phenomenon was first studied by Chen $et\ al.$ in 1974 for binary mixtures of methane with n-butane[141] and n-pentane,[142] where "S-shaped" dew curves were observed at fixed temperatures near the critical point of methane. In contrast to the "C-shaped" p-x-y dew point curves of "single" retrograde vaporization in supercritical fluids, DRV shows triple- or quadruple-valued dew points for specific compositions approaching purity of the volatile component.[139] From the perspective of natural gas production, this phase behavior allows for multiple liquid dropout events to occur as gas condensate mixtures flow towards a producing well, where the flow's pressure gradient can cross multiple dew points. DRV has also been suggested as a means to increase the efficiency of supercritical fluid extraction by optimizing the use of its characteristic solubility extremas.[143] In addition to its practical relevance, further exploring DRV is important to better understand the fundamental properties of infinitely-dilute near-critical fluids.

Accurately predicting complex condensation behavior by means of adequate thermodynamic models is of great importance, especially for preventing operational problems at conditions where experimental measurements are limited or unavailable. While DRV studies in the literature are quite scarce, DRV has been modeled for various mixtures using equations of state (EoS). Raeissi $et\ al.$ have modeled DRV using the Peng-Robinson[27] (PR) EoS for asymmetric mixtures where CO_2, N_2, and light alkanes constitute the low-boiling components,[151,156] showing the prevalence of DRV across mixtures with different chemical substances. DRV has also been modeled with advanced molecular-based EoS, such as those in the Statistical Associating Fluid Theory (SAFT)[34,35,147,148] family. Perturbed-chain SAFT (PC-SAFT)[40] has been shown to be capable of reproducing DRV for various n-alkane mixtures,[152] as well as showing satisfactory performance for modeling phase behavior of multicomponent mixtures representative of reservoir and gas injection fluids.[157] Nonetheless, the predictive capabilities of these thermodynamic models are often limited or unreliable for complex phase behavior. For example, experimental observations have shown that retrograde condensation can yield two distinct liquid phases,[158] yet this three-phase behavior can also be artificially reproduced by using non-classical combining rules. Alfradique and Castier demonstrated this by using the PR EoS for methane/n-pentane binary mixtures,[153] even though n-hexane is the lightest n-alkane to present partial liquid phase immiscibility with methane. Moreover, EoS predictions often rely on fitting binary interaction parameters that require optimization for different temperatures,[159] which limits their applicability.

In this work, configurational-bias Monte Carlo simulations[60,61,66] in the isobaric-isothermal version of the Gibbs ensemble[57,59,67] were carried out to study DRV for mixtures containing different “heavy” and “light” components. The term “heavy” corresponds to compounds of low volatility, whereas “light” corresponds to compounds with low boiling temperatures. In the systems investigated here, either methane or CO_2 constitutes the light components in their respective systems. Mixtures containing methane resemble natural gas in gas condensate reservoirs, whereas mixtures with carbon dioxide resemble CO_2-based injection fluids used in EOR. In contrast to EoS and empirical thermodynamic models, Monte Carlo simulations are a powerful tool for predictive modeling, capable of reliably providing molecular-level details for many complex systems. Hence, the goals of this work were to explore DRV in different mixtures via molecular simulation, predict dewpoint curves and full vapor-liquid coexistence envelopes, and investigate fluid structuring at a molecular level.

This chapter is organized as follows: molecular models and calculation details are described in Section 5.2, results are presented and discussed separately for methane and CO_2 systems in Section 5.3, and Section 5.4 provides concluding remarks.

5.2 Computational Details

5.2.1 Monte Carlo Simulations

Gibbs ensemble Monte Carlo (GEMC) simulations[57,59,67] allow for direct calculations of mixture equilibria for arbitrary numbers of components,[135] making them suitable for modeling a variety of mixtures. The MCCCS-MN program[74] was used to carry out GEMC simulations in the isobaric-isothermal (NpT) ensemble for methane-based and CO_2-based mixtures, where these two compounds constitute the near-critical components in their respective mixtures. All simulations were performed at a reduced temperature of $T_\mathrm{r} = 0.995$ with respect to the critical temperature of either methane or CO_2. A range of pressures were simulated, where the upper bounds were set to the vapor pressures of the low-boiling compounds at $T_\mathrm{r} = 0.995$. Pure component vapor pressures were determined from GEMC simulations in the canonical ensemble (NVT-GEMC) for systems consisting of 5000 particles. For NpT-GEMC simulations, the total system size was fixed to 5500 molecules with at least 5000 methane or CO_2 molecules. The remaining number of molecules was adjusted so as to yield overall compositions within phase coexistence boundaries.

Simulations were averaged over 8 independent runs, each run consisting of production periods of 50,000 MC cycles and 200,000 MC cycles for NpT-GEMC and NVT-GEMC simulations, respectively, where 1 MC cycle = N steps and N denotes the total number of particles in the system. Statistical errors are given as standard errors of the mean. Volume and swap moves were adjusted to yield an acceptance frequency on the order of 1 accepted move of each type per MC cycle[110] to optimize computing efficiency. The remaining fraction of moves were evenly distributed among translation, rotation, and CBMC[60,61,66] conformational moves for flexible and semiflexible molecules. Translation and rotation moves were allowed for CO_2 molecules, whereas only translation moves were allowed for methane molecules.

For methane-based mixtures, binary and ternary systems of methane + (n-butane and/or i-butane) were investigated using the united-atom version of the transferable potentials for phase equilibria (TraPPE–UA) force field.[66,69] This force field makes use of

Lennard-Jones (LJ) and Coulomb potentials for the nonbonded interactions of CH_x pseudo-atoms:

$$U\left(r_{ij}\right) = 4\epsilon_{ij}\left[\left(\frac{\sigma_{ij}}{r_{ij}}\right)^{12} - \left(\frac{\sigma_{ij}}{r_{ij}}\right)^{6}\right] + \frac{q_i q_j}{4\pi\epsilon r_{ij}} \tag{5.1}$$

where r_{ij}, ϵ_{ij}, σ_{ij}, q_i, and q_j are the separation, LJ potential well depth, LJ diameter, and partial charges, respectively. Intramolecular degrees of freedom are governed by a fixed C–C bond length, a harmonic angle bending potential, and a cosine series torsional potential. These united-atom models provide an excellent compromise between accuracy and computational efficiency, which is an important factor to consider given the computing cost of simulating large near-critical systems. All Lennard-Jones potentials were truncated at 1.4 nm. Lorentz-Berthelot combining rules[99] were used for non-bonded interactions between unlike pseudoatoms, and analytical tail corrections were applied.[54] Based on the results of the finite-size scaling study of Potoff and Panagiotopoulos for Lennard-Jonesium,[102] the critical temperature and pressure of TraPPE–UA methane used in this work were $T_c = 194.18$ K and $p_c = 50.36$ bar, corresponding to the infinite system size limit.

To provide a systematic analysis of the influence of heavy components on DRV, a constant molar ratio of n-butane:i-butane equal to 1:3, 1:1, or 3:1 was imposed, where these ratios are defined based on the total number of butane molecules in the system. The total number of molecules of each component was adjusted at every pressure so as to maintain a constant molar ratio of butane isomers in the system, while simultaneously maintaining the overall composition within the coexistence boundaries of the phase envelope. Additionally, binary mixtures of methane with either butane isomer were also simulated.

For CO_2-based mixtures, binary systems containing n-heptane (C7), n-nonane (C9), benzene (BZ), toluene (TL), or ethylbenzene (EB) as heavy components were investigated. The TraPPE force field was used for CO_2,[160] benzene,[161] and alkylbenzenes,[162] as well as TraPPE–UA for C7 and C9.[69] While the all-atom models are used for the ring structure of arene molecules, the non-polar substituents on toluene and ethylbenzene are represented by united-atom CH_x pseudo-atoms. Due to the large number of electrostatic interactions present, computing pairwise interactions in Equation 5.1 for this set of mixtures becomes computationally expensive. Therefore, a group-based cutoff of 1.6 nm was applied without applying the Ewald summation technique,[54] which has been previously applied to handle electrostatic interactions for the TraPPE CO_2 model.[160,163] Similar to simulations for methane mixtures, Lorentz-Berthelot combining rules[99] were used for non-bonded interactions between unlike sites. Because the vapor pressure of CO_2 would decrease without

inclusion of Ewald summation, analytical tail corrections were also excluded to counter this pressure offset. This approach was validated for phase equilibria of neat CO_2 and benzene systems.

Mixtures that exhibit DRV also show highly non-linear behavior in near-critical volumetric properties. Raeissi and Peters analyzed this on the basis of differential molar volumes $(\partial V/\partial x)_{T,p}$, whose non-linear behavior was explained as a transition to critical behavior for infinitely dilute systems.[139] To assess DRV influence on volumetric properties, number densities of volatile and heavy components were analyzed for both vapor and liquid phases. Because GEMC simulations allow for direct determination of partitioning between coexisting liquid and vapor phases,[144] the Gibbs free energy of transfer (ΔG_t) was computed directly from the number densities in each phase using Equation 5.2, where $\rho_{t,\mathrm{liq}}$ and $\rho_{t,\mathrm{vap}}$ are the number densities of molecule type t in liquid and vapor phases, respectively.

$$\Delta G_t = -RT \ln \left(\frac{\rho_{t,\mathrm{liq}}}{\rho_{t,\mathrm{vap}}} \right) \tag{5.2}$$

Partitioning was also investigated by computing K values for heavy components in ternary mixtures, given by

$$K_t = y_t / x_t \tag{5.3}$$

where y_t and x_t are mole fractions of molecule type t in vapor and liquid phases, respectively. In addition, structural features were analyzed by computing center-of-mass radial distribution functions (RDF) and their respective number integrals for the liquid phase, providing a detailed view of the effects of DRV on molecular packing.

5.2.2 Equations of State

In addition to Monte Carlo simulations, DRV was modeled using two well-known equations of state: Peng-Robinson[27] (PR EoS) and the perturbed chain statistical associating flud theory[40] (PC-SAFT). Both models were used for VLE predictions, as well as providing number densities and free energies of transfer for comparison to GEMC simulations.

The original formulation of the PR EoS was used, which in pressure-explicit form is given by:

$$p = \frac{RT}{V-b} - \frac{a\alpha(T)}{V(V+b)+b(V-b)} \tag{5.4}$$

Here, R is the gas constant, while a, b, and $\alpha(T)$ are component-specific constants that account for the attractive intermolecular interactions, hard core volume of the fluid, and the

corresponding state of the system. These were calculated from pure fluid critical properties using:

$$\begin{aligned} a &= 0.45724\frac{R^2T_{\rm c}^2}{P_{\rm c}} \\ b &= 0.07780\frac{RT_{\rm c}}{P_{\rm c}} \\ \alpha(T) &= [1+(0.37464{+}1.54226\omega - 0.26992\omega^2)(1-\sqrt{T_r})]^2 \end{aligned} \tag{5.5}$$

Values for $T_{\rm c}$, $P_{\rm c}$, and acentric factor (ω) are given in Table 5.1 for the components studied in this work. The standard one-fluid van der Waals mixing rules were applied, which include a single temperature independent binary interaction parameter, $k_{\rm ij}$, and are given by:

$$\begin{aligned} a\alpha(T) &= \sum_{i=1}^{c}\sum_{j=1}^{c} x_i x_j \sqrt{(a\alpha)_i (a\alpha)_j}(1-k_{ij}) \\ b &= \sum_{i=1}^{c} x_i b_i \end{aligned} \tag{5.6}$$

By regressing the $k_{\rm ij}$ parameter against reliable VLE data, experimental measurements can be accurately correlated within fitting boundaries, whereas predictive calculations require all $k_{\rm ij}$ parameters be set to zero.

In contrast to cubic EoS, PC-SAFT has theoretical foundations based on Wertheim's first order perturbation theory,[36–39] similar to all SAFT models. Because PC-SAFT applies free energy perturbations to a reference fluid, it is generally expressed as a summation of residual Helmholtz free energy terms, $A^{\rm res}$, that account for different molecular interactions in the system, given by:

$$\begin{aligned} \frac{A^{res}(T,\rho)}{NRT} = \frac{a^{res}(T,\rho)}{RT} &= \frac{a(T,\rho)}{RT} - \frac{a^{ideal}(T,\rho)}{RT} = \frac{a^{ref}(T,\rho)}{RT} + \frac{a^{disp}(T,\rho)}{RT} \\ &= \frac{a^{hs}(T,\rho)}{RT} + \frac{a^{chain}(T,\rho)}{RT} + \frac{a^{disp}(T,\rho)}{RT} + \frac{a^{assoc}(T,\rho)}{RT} \end{aligned} \tag{5.7}$$

where the superscripts $res, ideal, ref, hs, chain, disp,$ and $assoc$ refer to residual, ideal, reference, hard sphere, chain, dispersion, and association terms, respectively. In this work, the original formalism of Gross and Sadowski[40] was used, which requires the use of three parameters for each pure component: the number of segments, m, in the chain molecule, the chain segment diameter, $\sigma_{\rm i}$, and the energy of dispersion interactions between segments, $\epsilon_{\rm i}$. Two more parameters can be used for pure components that exhibit association interactions (i.e. alkanols, water, amines, etc.[164]): the association energy between sites

of like molecules, $\epsilon^{A_iB_i}$, and the volume of association, $\kappa^{A_iB_i}$. These parameters are fitted to experimental vapor pressures and saturated liquid densities from low temperatures up to close to the critical point. Table 5.1 provides PC-SAFT parameter values for the components used in this work. PC-SAFT EoS is extended to mixtures by introducing σ_{mix} and ϵ_{mix}, which are evaluated by the following mixing rules derived from van der Waals one-fluid theory:[146,165]

$$\begin{aligned} \sigma_{\mathrm{mix}}^3 &= \frac{\sum_{i=1}^{c}\sum_{j=1}^{c} x_i x_j m_i m_j \sigma_{\mathrm{ij}}^3}{(\sum_{i=1}^{c} x_i m_i)^2} \\ \epsilon_{\mathrm{mix}}\sigma_{\mathrm{mix}}^3 &= \frac{\sum_{i=1}^{c}\sum_{j=1}^{c} x_i x_j m_i m_j \sigma_{\mathrm{ij}}^3 \epsilon_{\mathrm{ij}}}{(\sum_{i=1}^{c} x_i m_i)^2} \end{aligned} \tag{5.8}$$

Table 5.1: Pure component parameters for PR EoS[31] and PC-SAFT.[40]

	PC-SAFT			PR EoS		
Compound	m	σ [Å]	ϵ/k_{B} [K]	T_{c} [K]	P_{c} [MPa]	ω
Methane	1.0000	3.7039	150.03	190.56	4.599	0.0115
n-Butane	2.3316	3.7086	222.88	425.12	3.796	0.2002
i-Butane	2.2616	3.7574	216.53	407.80	3.648	0.1835
Carbon Dioxide	2.0729	2.7852	169.21	304.21	7.383	0.2240
Heptane	3.4831	3.8049	238.40	540.20	2.740	0.3500
Nonane	4.2079	3.8448	244.51	594.60	2.290	0.4440
Benzene	2.4653	3.6478	287.35	562.20	4.898	0.2100
Toluene	2.8149	3.7169	285.69	591.80	4.106	0.2620
Ethylbenzene	3.0799	3.7974	287.35	617.20	3.606	0.3030

Dispersion interaction parameters were calculated using Lorentz-Berthelot combining rules:

$$\begin{aligned} \sigma_{\mathrm{ij}} &= \frac{1}{2}(\sigma_{\mathrm{i}} + \sigma_{\mathrm{j}}) \\ \epsilon_{\mathrm{ij}} &= \sqrt{\epsilon_{\mathrm{i}}\epsilon_{\mathrm{j}}}\,(1 - k_{\mathrm{ij}}) \end{aligned} \tag{5.9}$$

As with PR EoS, a temperature independent k_{ij} parameter is included in the mixing rules, which can be regressed to correlate experimental VLE data.

5.3 Results and Discussion

5.3.1 VLE in Methane-based Systems

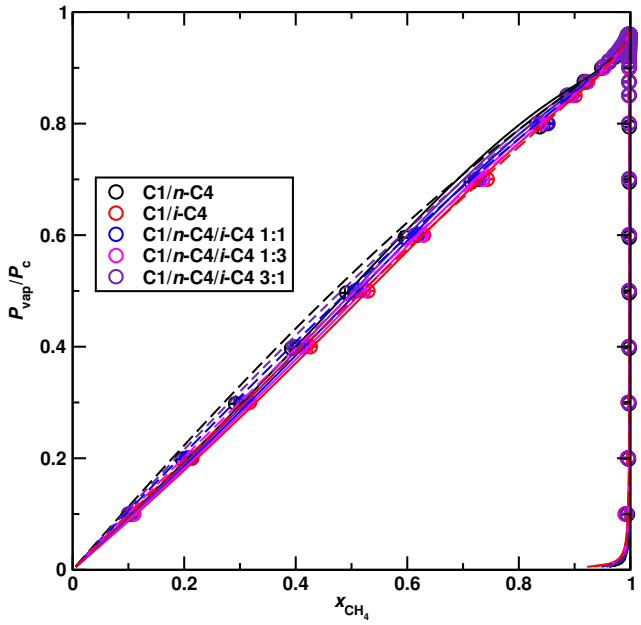

Figure 5.1: Pressure-composition diagram for methane + (n-butane and/or i-butane) mixtures. Circles denote GEMC simulations, solid lines denote PR EoS, and dashed lines denote PC-SAFT. Color scheme is equivalent for both simulation and EoS. n-C4:i-C4 ratios labeled for ternary mixtures.

Given that the TraPPE force field, Peng-Robinson, and PC-SAFT each reproduce different critical points for methane, phase diagrams were analyzed in reduced units to compare VLE prediction at the same corresponding states. The pressure-composition diagrams in Figure 5.1 show that excellent agreement is obtained between both EoS and GEMC when projected in reduced units. This agreement suggests that both methods yield similar VLE behavior at the same corresponding states, where other properties are likewise comparable. Since 194.17 K is well below the critical temperature of both butane isomers, the phase diagram of these mixtures is very similar in width and only varies slightly with overall composition. Given that i-butane is more volatile that n-butane, the concentration of methane increases slightly in the liquid phase for systems with higher i-C4:n-C4 molar

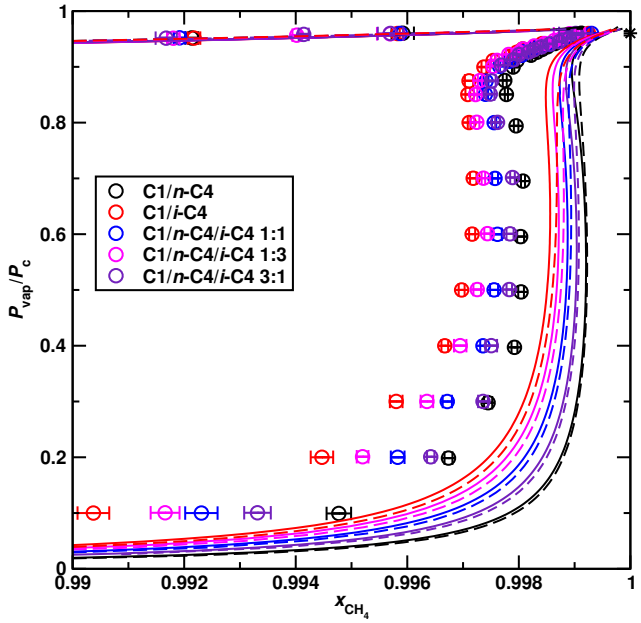

Figure 5.2: Dew curves for methane + (n-butane and/or i-butane) mixtures. Symbols and color defined in Figure 5.1.

ratios at low to moderate pressures.

The difference in critical properties between the low-boiling compound and both butane isomers makes this system quite asymmetric. Therefore, one needs to look at compositions very close to the pure methane axis to observe DRV. The dew curves in Figure 5.2 show that DRV is observed in within a small composition for both binary and ternary mixtures. More importantly, the effect of fixed molar ratio on DRV causes the dew curves to shift systematically in the x-axis with overall composition, where the overall shape of the curve is very similar irrespective of the butane isomer molar ratio. Due of the difference in volatility between both butane molecules, the combined partial pressures of the heavy components determine the extent to which the dew curves are shifted. Hence, dew curves with smaller n-butane:i-butane ratios are shifted to lower methane concentrations, since i-butane is more volatile. The effect of heavy-component vapor pressure on DRV has been discussed previously (see Section 4.3.5), and is in agreement with the results shown in Figure 5.2. In this regard, the ternary mixtures can be considered to exhibit "pseudo-binary" phase behavior, where the distinction is made between the low-boiling compound

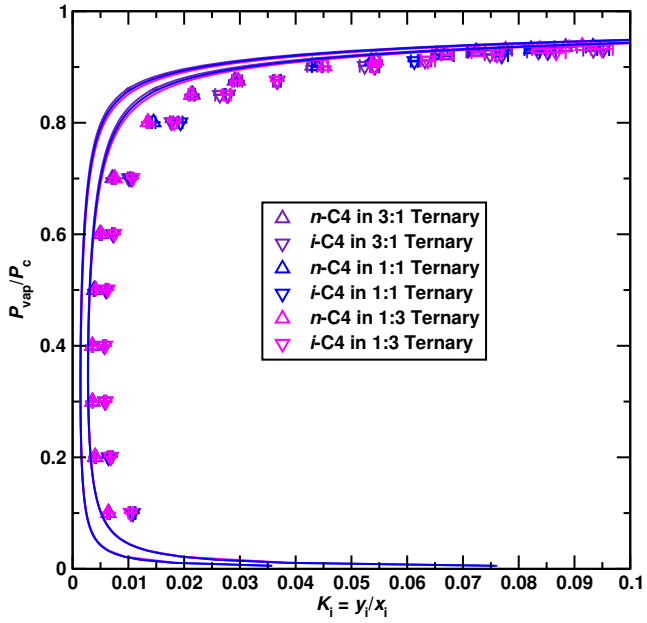

Figure 5.3: K-values for C4 alkanes in methane + (n-butane and/or i-butane) mixtures. Triangles denote GEMC simulations, solid lines denote PR EoS, and dashed lines denote PC-SAFT. EoS and GEMC both yield K-values for n-butane that are lower than those of i-butane.

and the heavy components in the system. It is important to note that both EoS and GEMC simulations predict dew curve shifts with very similar dependence on butane molar ratio. In this regard, there is good qualitative agreement between both methods.

Because DRV causes non-linear variations in composition, it is worthwhile to examine partitioning of heavy components between coexisting phases. Using Equation 5.3, the K-values for methane are orders of magnitude larger than for either butane isomer and approach unity near the critical point due to the relatively large fraction of methane in the vapor phase. Hence, analyzing K-values for butane molecules requires looking at the low K-value range, as shown in Figure 5.3. Although the overall composition varies among the ternary mixtures, the K-values suggest that butane partitioning remains unaffected by the overall composition of the system throughout the entire pressure range, where the K-values of i-butane are consistently higher than those of n-butane. At high

pressures, however, the values for both butane isomers approach unity over a small pressure range as both phases approach pure methane composition, where the butane components are infinitely diluted. The sharp change in trend indicates a transition towards state points where the coexisting phases become increasingly similar in proximity to the critical point of methane. The low K-values suggest the butane partitioning favors the liquid phase at low to moderate pressures, yet near the critical point (at pressures roughly above $p_{\mathrm{r}} = p_{\mathrm{vap}}/p_{\mathrm{c}} = 0.8$), the partition ratio shifts away from the liquid phase as this phase becomes more compressible. This transition is clearly linked to DRV, given that the transition occurs within the pressure range where the dew curves exhibit non-linear behavior. Furthermore, this change in phase behavior seems to be well described by both EoS and GEMC simulations, in accordance to the good agreement found for the p-x-y diagrams.

5.3.2 Number Densities in Methane-based Systems

Previous studies suggest that DRV is correlated with non-linear behavior in the molar volume of the coexisting phases within the critical region. This non-linear behavior can be investigated by analyzing the number densities for each component in the coexisting phases. Figure 5.4 shows the number densities obtained from GEMC simulations and PC-SAFT calculations. These results show that the liquid phase becomes "swelled" with methane for pressures above $p_{\mathrm{r}} = 0.8$ (see upper left panel in Figure 5.4), where the number density increases higher than that of the saturated liquid. This result is in accordance with the explanation provided by Raeissi and Peters,[139] where the molar volume is influenced by the increased compressibility of the low-boiling compound in the liquid phase at near-critical conditions. Moreover, the ratio of heavy components has very little effect on methane "swelling", which agrees with the relatively small effect it shown for the composition of the liquid phase. Similarly, the methane number density in the vapor phase increases monotonically with pressure, where the butane molar ratio has no visible effect.

In contrast to methane, the number densities of the heavy components show stronger dependence on butane ratios in both phases. For clarity, the results from PR EoS are shown separately in Figure 5.5. In the liquid phase, the butane ratio is directly proportional to the number density. For example, the ternary system with a 1:1 butane ratio has equal number densities for both butanes, shown by overlapping blue lines in the lower right panel of Figure 5.5. For binary mixtures, the number densities are determined by the relative volatilities of the heavy components. In these cases, the number density of i-butane is

lower than that of n-butane for the liquid phase, whereas the opposite is true in the vapor phase. Moreover, the liquid phase "swelling" effect is proportional to the heavy component number density in the vapor phase, where non-linear behavior is observed for pressures higher than $p_{\mathrm{r}} = 0.8$. To show the relationship between dew curve shift and the amount of heavy components in the vapor phase, the sum of both number densities is shown as dashed-dotted lines in the lower right panel of Figure 5.5 for ternary mixtures. The sum of number densities clearly shows the same dependence on butane ratio as the dew curves, and each curve has the same general shape regardless of component or butane ratio. This suggests that these systems indeed exhibit "pseudo-binary" DRV behavior, where all heavy components respond similarly to liquid phase "swelling" effect, and their combined number densities are directly proportional to the composition shift of dew curves.

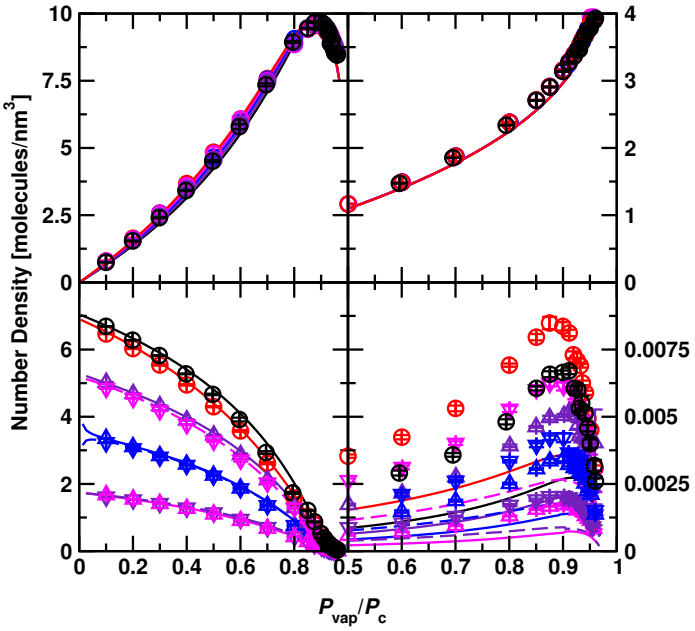

Figure 5.4: Number densities of methane (top) and alkanes (bottom) in liquid (left) and vapor (right) phases. Color scheme represents n-alkane ratios as in Figure 5.1. Symbols denote GEMC simulations and lines denote EoS. For ternary mixtures, triangles denote GEMC data for n-butane (up) and i-butane (down), while lines denote PC-SAFT predictions ($k_{\mathrm{ij}} = 0$) for n-butane (solid) and i-butane (dashed).

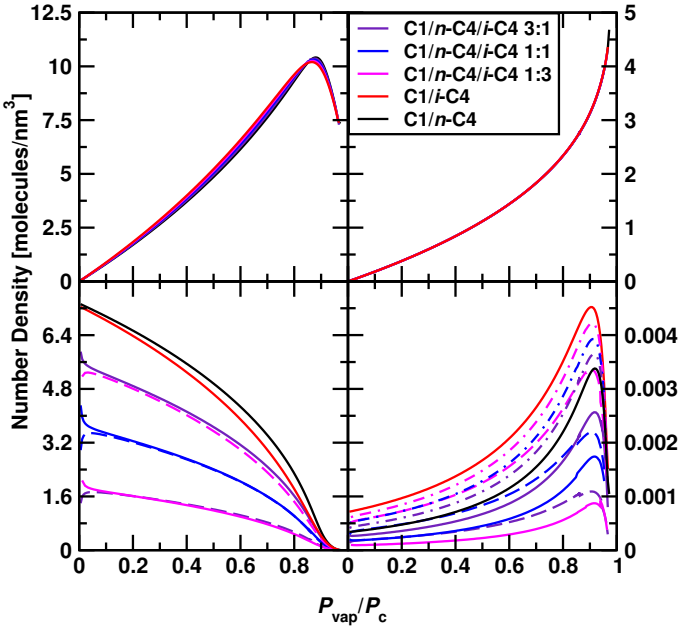

Figure 5.5: Number densities of methane (top) and alkanes (bottom) in liquid (left) and vapor (right) phases from PR EoS predictions ($k_{\mathrm{ij}} = 0$). Color scheme and symbols as in Figure 5.4. Dotted-dashed lines in lower right panel denote sum of number densities of n-butane and i-butane.

5.3.3 Free Energy of Transfer in Methane-based Systems

In addition to the determination of volumetric properties for coexisting phases, GEMC simulations allow for calculation of the Gibbs free energy of transfer across the entire pressure range by means of Equation 5.2. In Figure 5.6, the Gibbs free energies of transfer are shown for each component. At the critical point, this quantity becomes zero and, therefore, the Gibbs free energies of transfer for methane have lower magnitudes relative to those for either butane. Because Equation 5.2 takes in number densities as direct input, the non-linear behavior observed for dew curves becomes reflected in ΔG_t, where the top panel in Figure 5.6 shows a sharp change with pressure around $p_{\mathrm{r}} = 0.8$ for methane. This sharp decrease in ΔG_t (in absolute values) corresponds to the onset of liquid-phase methane "swelling", reflecting the transition towards states with relatively compressible liquid phases. For methane, PR EoS and PC-SAFT both predict systematic variations in

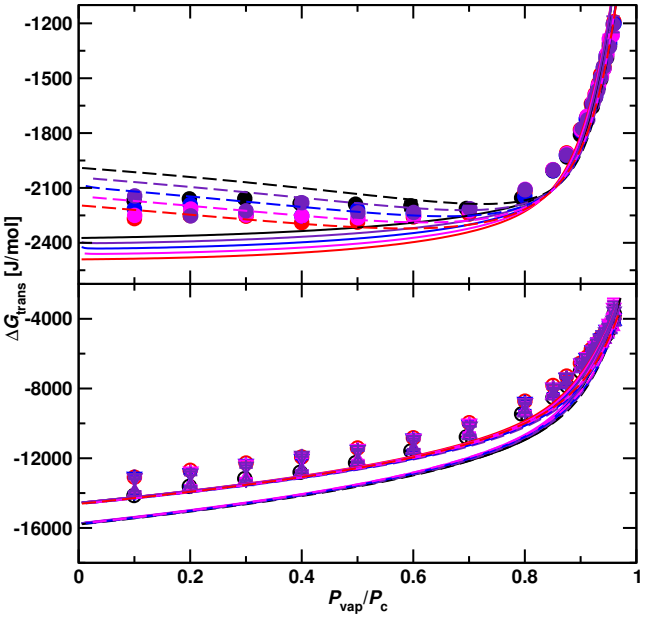

Figure 5.6: Gibbs free energy of transfer for methane (top) and alkanes (bottom). Color scheme defined in Figure 5.1. Symbols denote GEMC simulations, solid lines denote PR EoS, and dashed lines denote PC-SAFT. Free energies for n-butane are lower (more negative) than those of i-butane.

ΔG_t proportional to butane ratios, whereas GEMC simulations show a more subtle dependence. However, at higher pressures the predicted values from simulation and EoS are very similar, where the systems are composed of nearly pure methane.

For the heavy components (lower panel), the butane ratio has no effect on ΔG_t, where the values for n-butane are consistently lower than those of i-butane, and the difference between the two becomes negligible at high pressures due to infinite dilution. This trend is predicted with similar precision by PR EoS and PC-SAFT, whereas the shortcomings of the united-atom models in correctly predicting vapor pressures cause GEMC prediction to yield higher ΔG_t values. This is similar to the predictions for heavy components in the vapor phase. Nonetheless, qualitative agreement is clearly obtained between EoS and simulation results. It is important to note that the choice of simulating VLE with united-atom models is most limited for molecules far below their critical point (i.e. closer to their normal boiling point), where the packing fraction in dense liquid phases is not described as properly

with pseudoatoms as it is with explicit-hydrogen models.[66] However, this effect proved to have little influence on the phase behavior and ΔG_t values for this system because the chain length of either butane is relatively small. Packing limitations can cause significant deviations for longer alkanes.[163]

5.3.4 Structural Analysis of Methane-based Systems

As noted in the previous section, accurately describing molecular packing is important for properly predicting VLE. A well-recognized advantage of molecular simulations is the ability to produce detailed microscopic information directly from fluid configurations. To address the structural features that influence DRV, center of mass radial pair distribution functions (RDF) of liquid phases were computed across a range of pressures. Figure 5.7 shows the RDFs of different pairs of molecules for mixtures with different butane ratios. As shown in all four panels, molecular packing remains largely unaffected by the ratio

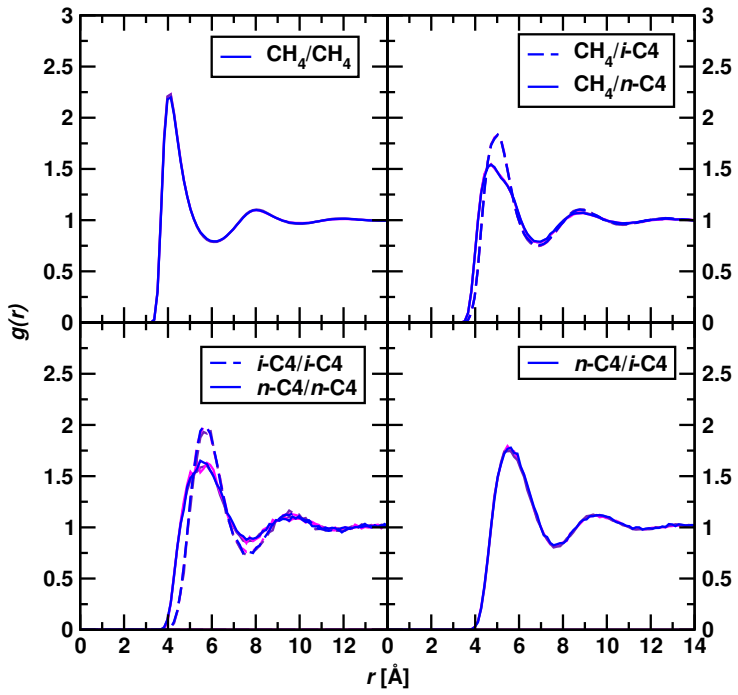

Figure 5.7: Liquid phase radial distribution functions for methane-based mixtures at a pressure of 40 bar. Solid and dashed lines defined for each panel. Color scheme defined in Figure 5.1.

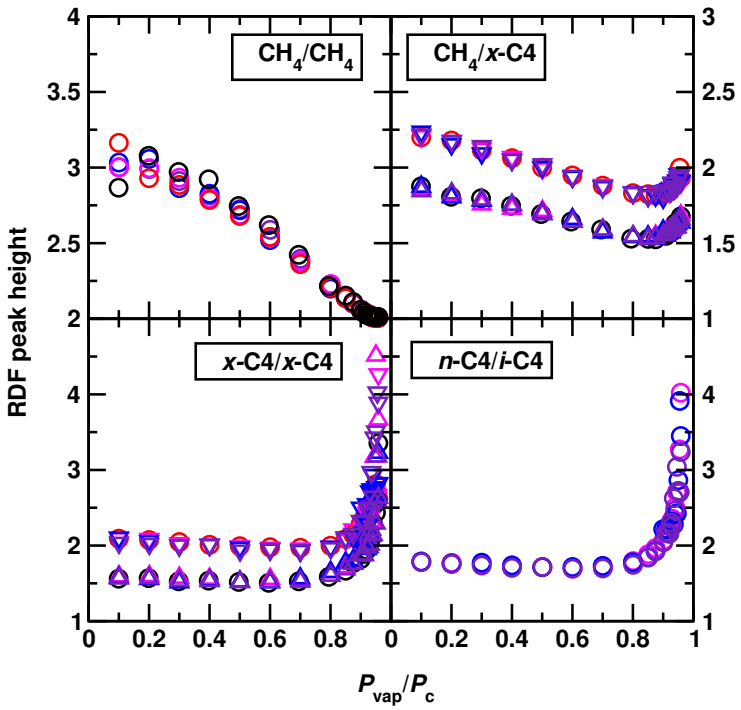

Figure 5.8: Peak heights of liquid phase radial distribution functions as a function of reduced pressure. Color scheme defined in Figure 5.1. Triangles denote peaks for RDFs involving n-butane (up) and i-butane (down).

of butane molecules in the system. For example, n-butane and i-butane pack differently around methane molecules as seen in the top right panel of Figure 5.7, yet this difference is consistent across mixtures with different overall compositions. An interesting observation is that the n-C4/i-C4 RDF peak height seems to be roughly at the midpoint between n-C4/n-C4 and i-C4/i-C4 RDF peaks, and this peak height is maintained for different butane ratios. Therefore, these RDFs indicate that each butane isomer has a packing preference that is not affected by the overall composition, further suggesting that these asymmetric mixtures can be regarded as "pseudo-binary".

To observe the how packing changes across the entire pressure range, the height of RDF peaks from Figure 5.7 are analyzed as a function of reduced pressure, shown in Figure 5.8. These results show that the RDF peak for methane decreases monotonically with pressure, a feature associated with a loss of general structure as the system approaches

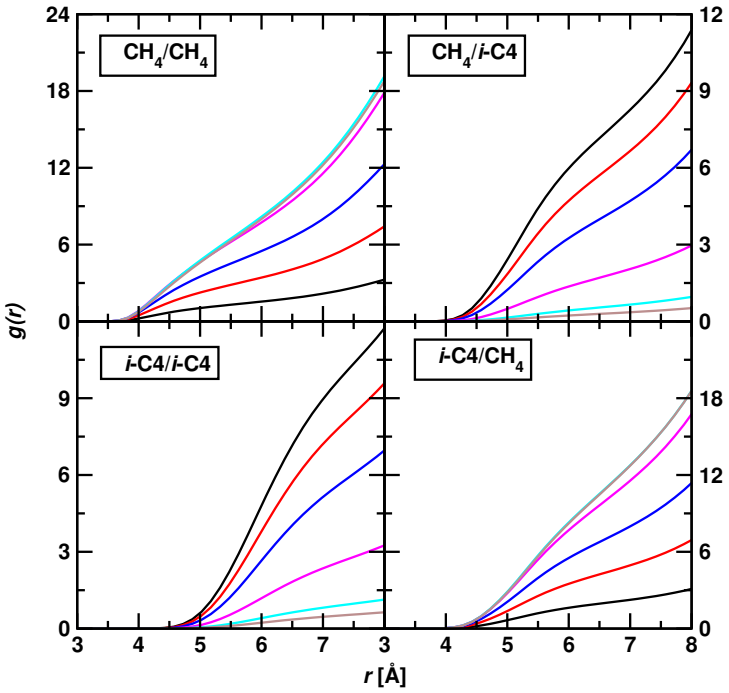

Figure 5.9: Liquid phase number integrals for different molecule pairs in CH_4/i-C4 binary mixtures at various reduced pressures between 0.2 (black lines) and 0.9 (brown lines).

the critical point, which causes the liquid phase to become more compressible. This structural loss is exhibited consistently for for all ternary mixtures and binary systems at low to moderate pressures. At higher pressures, a change in trend is observed, where the peak heights increase again. This change in fluid structuring is linked to the partitioning variations observed in Figure 5.3, where the butane molecules increasingly disfavor the vapor phase over the liquid phase. A similar trend is observed at elevated pressures between like butane pairs, although the peak heights remain nearly constant at low to moderate pressures. As with the RDFs in Figure 5.7, fluid structuring is consistent for both butane isomers in mixtures with different butane ratios. This is clearly observed for the RDF peak height of i-butane pairs at reduced pressures between 0.2 and 0.6, which have equivalent heights in CH_4/i-C4 binary mixtures and in ternary mixtures. The lower right panel of Figure 5.8 shows that the peak heights for unlike butane pairs yield RDF peaks with heights roughly equal to the average of the peak heights for the like butane pair RDFs, particularly at lower to moderate pressures. Overall, these results show how structuring is influenced

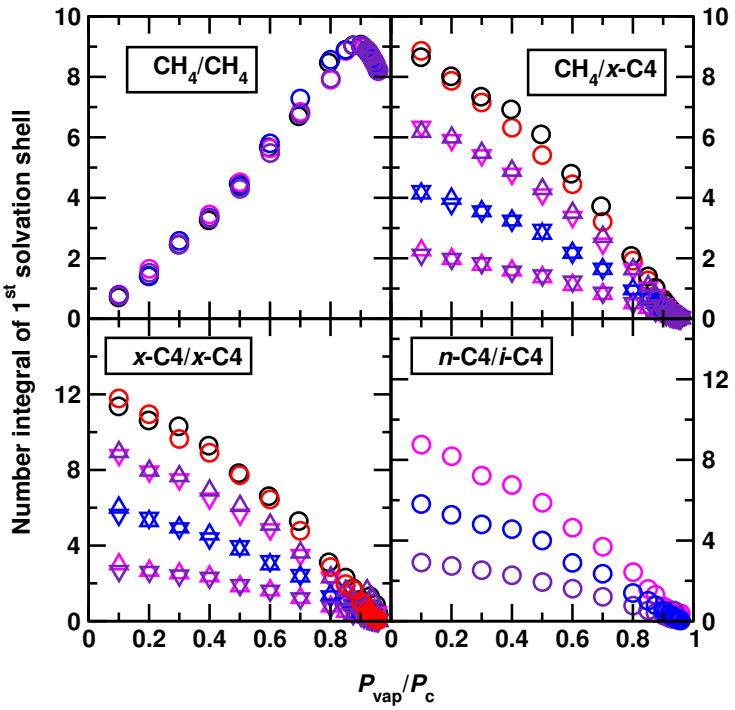

Figure 5.10: Liquid phase number integrals of the first solvation shell as a function reduced pressure for molecule-molecule pairs in mixtures with different butane ratios. Color scheme defined in Figure 5.1. Triangles denote number integrals from RDFs involving n-butane (up) and i-butane (down).

as the system approaches near-critical states.

Number integrals of center of mass RDFs were computed for the first solvation shell (i.e. up to the first minimum in $g(r)$ beyond the peak position) from the molecule-molecule RDFs of different mixtures. Examples of these number integrals are shown in Figure 5.9 for CH_4/i-C4 binary mixtures at various reduced pressure between 0.2 (black lines) and 0.9 (brown lines). For clarity, the value of the number integrals for the first solvation shell were analyzed as a function pressure, and are shown in Figure 5.10. The results for number integrals from RDFs of like pairs (left panels in Figure 5.10) show much resemblance to the results obtained for liquid phase number densities in Figure 5.4, indicating that the effects of methane "swelling" in the liquid phase are observable within the scale of the first solvation shells. In other words, the first solvation shell of methane pairs contains more methane

molecules than methane pairs in saturated liquid methane for a short range of pressures above $p_r = 0.8$. Furthermore, the overall packing behavior in the first solvation shell between methane pairs seems to have no dependence on the ratio of butane molecules in the system, similar to the number densities of methane in the liquid phase. On the other hand, the integrals for pairs involving either butane isomer are directly influenced by the butane ratio of the mixture, similar to the number density of butane isomers in the liquid phase. In this regard, only the molecular packing behavior of the low-boiling compound is influenced by the proximity to its critical point, whereas the structural transitions observed for the molecular packing of heavy compounds are determined directly by their vapor-liquid partitioning.

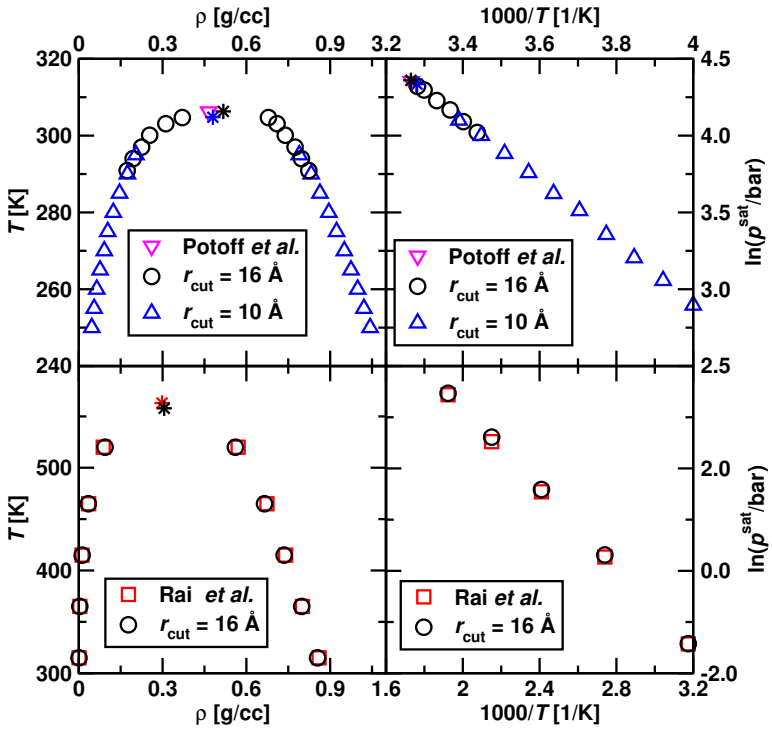

Figure 5.11: Coexistence densities (left) and vapor pressures (right) for CO_2 (top) and benzene (bottom). Experimental data taken from Potoff[160] and Rai.[161]

5.3.5 VLE in CO_2-based Systems

The simulation approach applied to carbon dioxide mixtures uses a group-based cut-off of 1.6 nm and excludes both Ewald summation and analytical tail corrections. This simulation setup was validated by computing vapor-liquid coexistence curves for CO_2 and benzene, where critical temperatures and critical densities were computed using the saturated density scaling law and the law of rectilinear diameters with a scaling exponent $\beta^* = 0.326$. The critical pressure of CO_2 was obtained by extrapolating the Clausius-Clapeyron equation to T_c. Simulations for CO_2 were compared to NVT-GEMC simulations for a system size of 500 molecules using a 1.0 nm cutoff, Ewald summation, and a scaling exponent of $\beta^* = 0.32$, which conform to the original specifications of Potoff and Siepmann.[160] As seen in Figure 5.11, deviations from established models using this group-based approach are minimal, suggesting that phase behavior of both CO_2 and benzene is modeled adequately with this approach. Temperatures close to the critical point of CO_2 were simulated to accurately determine vapor-liquid coexistence near T_c using the 1.6 nm cutoff approach, as well as for determining the vapor pressure of carbon dioxide at $T_r = 0.995$. The critical temperature and pressure for CO_2 using this approach were found to be $T_c = 306.3$ K and $p_c = 78.25$ bar, respectively.

Similar to methane-based systems, VLE was analyzed for CO_2 mixtures using the same corresponding state approach, where vapor pressures were reduced with respect to the critical pressure of CO_2. Pressure-composition diagrams for binary mixtures of CO_2 with alkanes and arenes are shown in Figures 5.12 and 5.13, respectively.

In contrast to the methane mixtures, PR EoS and PC-SAFT do not predict liquid phase compositions accurately for these systems. Both EoS require the use of binary interaction parameters fitted to experimental data for proper correlations. The pressure-composition diagrams computed using EoS with non-zero k_{ij} parameters are denoted in Figures 5.12 and 5.13 by dotted lines. The correlations agree very well with experimental bubble point measurements at similar temperatures,[166,167] which are denoted by triangles. Therefore, while the global pressure-composition diagrams seem to be correlated correctly by both EoS, the predictive capabilities are limited for these binary mixtures. For PC-SAFT, this limitation has been explained by Gross and Sadowski[40] based on the assumption that CO_2 molecules only exhibit dispersive attractions and, hence, the quadrupole moment of CO_2 is not accounted for properly. Similarly, the “attractive + hard repulsion” foundation of PR EoS seems insufficient to properly predict VLE in CO_2/hydrocarbon binary mixtures.

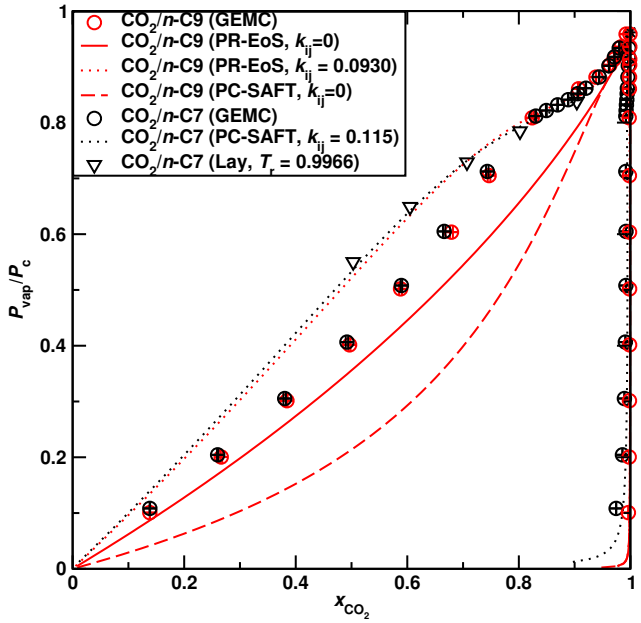

Figure 5.12: Pressure-composition diagram for CO_2 + n-alkane binary mixtures. Circles denote GEMC simulations, solid lines denote PR EoS, and dashed lines denote PC-SAFT. Triangles denote experimental measurements,[166] and dotted lines denote EoS calculations with non-zero binary interaction parameters.

With regards to liquid phase compositions, results from GEMC simulations show better agreement with experimental measurements and with EoS correlations using non-zero k_{ij} parameters. However, there is clearly better agreement for binary mixtures with arenes than for the linear alkanes. This larger deviation for CO_2/n-alkane mixtures is not entirely unexpected given that the simulation conditions are significantly below the critical point of C7 and C9, where the shortcomings of united-atom models are more pronounced due the higher packing fractions in saturated liquid phases.[163] This higher packing fraction leads to an overestimation of the solubility of CO_2 in the liquid phase, and increases with chain length. This effect has been observed in previous studies where CO_2/n-alkane mixtures were simulated using united-atom force fields.[168] Hence, using united-atom descriptions of linear alkanes for modeling such asymmetric mixtures yields better predictions for shorter alkanes, as is the case for the methane mixtures shown in Figure 5.1. From a practical

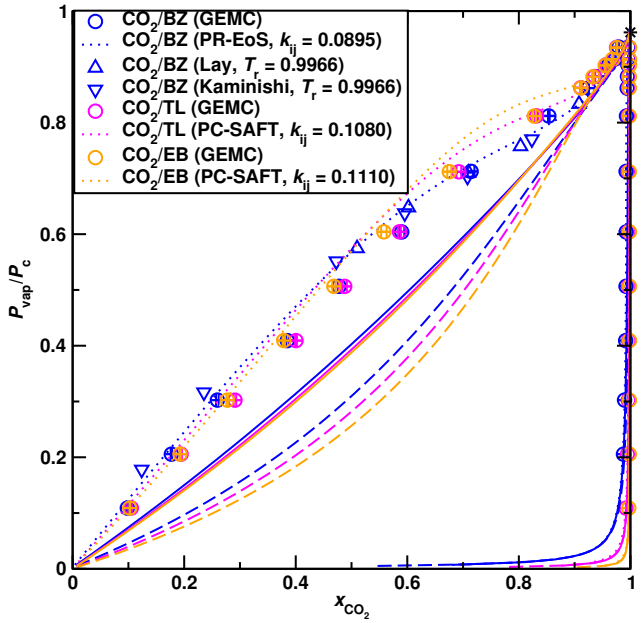

Figure 5.13: Pressure-composition diagram for CO_2 + arene binary mixtures. Circles denote GEMC simulations, solid lines denote PR EoS, and dashed lines denote PC-SAFT. Triangles denote experimental measurements of Lay[166] and Kaminishi.[167] Dotted lines denote EoS calculations with non-zero binary interaction parameters.

perspective, properly predicting CO_2 solubility in dense hydrocarbon phases is very important for CO_2 injection EOR, particularly when oil-phase swelling is desired. Therefore, the results in Figure 5.13 suggest that atomistic models can be used to provide more reliable predictions of liquid phase compositions, although at a higher computing cost.

Similar to liquid phase compositions, the compositions in the vapor phase are not very well predicted by either equation of state, where characteristic "S-shaped" dew curves are expected for systems that exhibit DRV. Figures 5.12 and 5.13 show the results from EoS predictions and correlations, as well as predictions from GEMC simulations. While EoS predictions fall short in predicting the expected "S-shape", calculations using a non-zero k_{ij} parameter properly correlate this effect. For example, the extent to which the dew curves in Figure 5.13 exhibit composition variations at high pressures is expected to increase with the molecular weight of the arene component, which increases the difference in critical properties between CO_2 and arenes. However, EoS predictions do not yield such

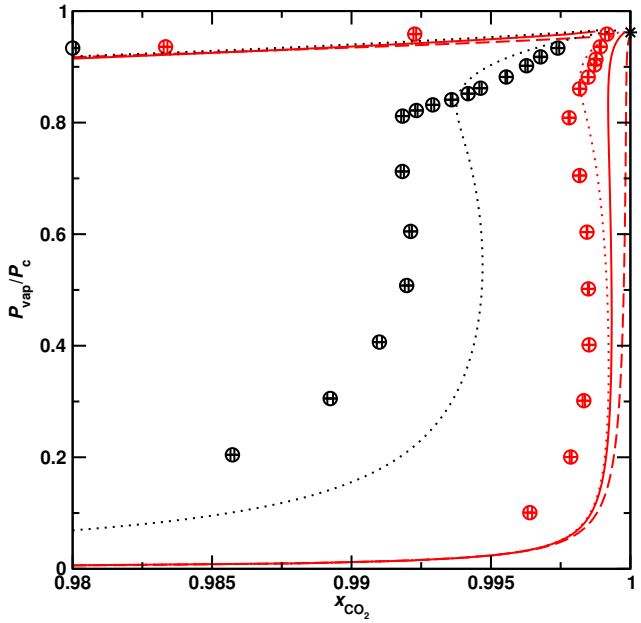

Figure 5.14: Dew curves for CO_2 + n-alkane binary mixtures. Symbols defined in Figure 5.12.

variations for any of the binary mixtures. These results further suggest that using non-zero k_{ij} parameters compensate for CO_2 interactions that are unaccounted for in PR EoS and PC-SAFT predictions, such as quadrupole-quadrupole interactions. Assessing the performance of other EoS with additional contribution terms, such as polar interactions in PC-PSAFT,[46] for predicting the phase behavior of CO_2/hydrocarbon mixtures is beyond the scope of this work and has been previously discussed in the literature.[169–171]

In contrast to PR EoS and PC-SAFT predictions, GEMC simulations predict "S-shaped" dew curves for all five binary mixtures. As with methane-based mixtures, the vapor pressure is overestimated for the linear alkanes, yielding a systematic offset with respect to EoS correlations. Although quantitative agreement is not obtained for n-alkane mixtures, GEMC predictions predict dew curves qualitatively despite overpredicting the solubility of CO_2 in the liquid phase. On the other hand, simulation predictions using explicit-hydrogen models properly predict DRV behavior, where dew curve compositions are in quantitative agreement with EoS correlations. The fact that GEMC simulations predict DRV for mixtures with either type of heavy component (i.e. alkanes or arenes) indicates that properly

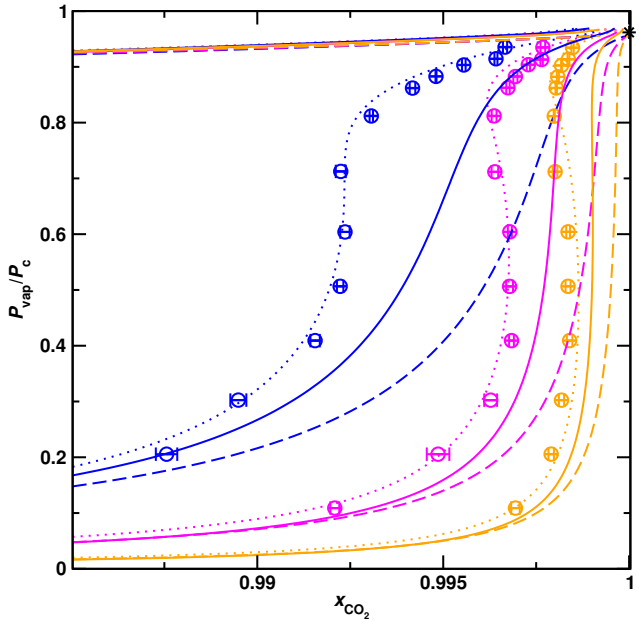

Figure 5.15: Dew curves for CO_2 + arene binary mixtures. Symbols defined in Figure 5.13.

predicting phase behavior for the low-boiling compound allows for qualitative DRV predictions, whereas quantitative predictions require properly describing the phase behavior of both components. In other words, the "S-shape" in dew curves is controlled by the phase behavior of the low-boiling compound in asymmetric mixtures that exhibit DRV. It is important to note that CH_x pseudoatoms are used for the alkyl substituents in toluene and ethylbenzene. Therefore, prediction accuracy may be affected for arenes as the number of CH_x pseudoatom sites increase per benzene ring, where adding united-atom character to the heavy compound contributes to increased CO_2 solubilities in liquid phases.

5.3.6 Number Densities in CO_2-based Systems

Given that volumetric properties have been shown to be linked to DRV behavior, the number densities of each component in liquid and vapor phases were analyzed as a function of reduced pressure for CO_2 mixtures. Figures 5.16 and 5.17 show number density predictions from PC-SAFT, PR EoS, and GEMC simulations, as well the the values calculated from EoS correlations. As was found for methane mixtures, the low-boiling compound

exhibits non-linear behavior for liquid phase number densities at high pressures. This result further confirms that the liquid phase becomes "swelled" by the low-boiling compound at high pressures, and is a general feature of mixtures that exhibit DRV. The isothermal compressibility of the pure component is expected to exhibit a transition towards near-critical behavior at high pressures and, hence, the "swelled" liquid phase becomes increasingly compressible. This non-linear behavior is well predicted by GEMC simulations for both types of heavy components, with greater accuracy found for CO_2/arene mixtures. In comparison to EoS predictions, the number densities of GEMC simulations are in better agreement with EoS correlations, which also show non-linear behavior at high pressures. Both PC-SAFT and PR EoS predictions considerably overestimate CO_2 number densities in the liquid phase. This overestimation is reflected in the liquid phase compositions in the p-x-y diagrams. While the high-pressure decrease in CO_2 liquid phase numer densities is observed for all predictions and correlations, the sharp increase slightly above $p_r = 0.8$ is only observed for calculations that yield proper descriptions of DRV behavior. Hence,

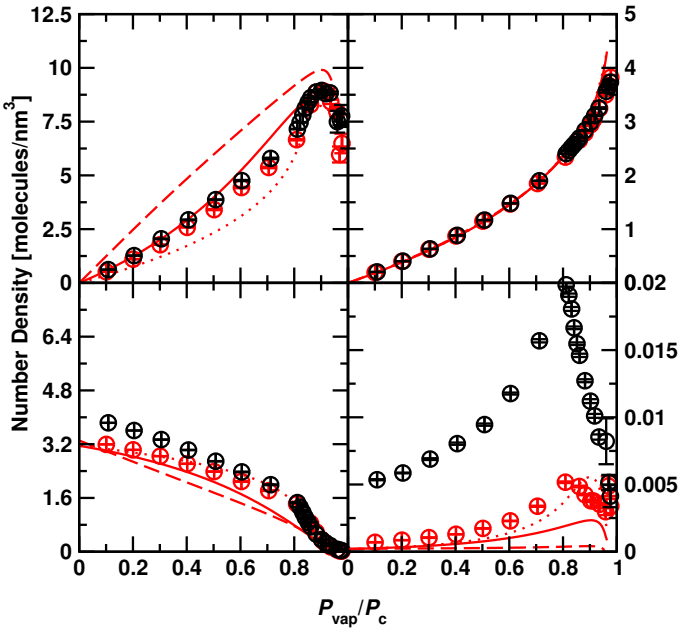

Figure 5.16: Number densities of CO_2 (top) and n-alkanes (bottom) in liquid (left) and vapor (right) phases. Color scheme and symbols defined in Figure 5.12.

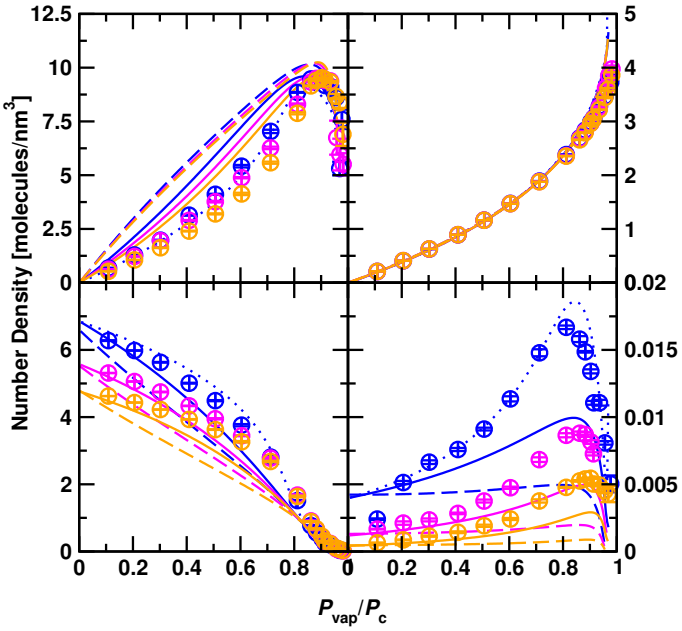

Figure 5.17: Number densities of CO_2 (top) and arenes (bottom) in liquid (left) and vapor (right) phases. Color scheme and symbols defined in Figure 5.13.

predicting this "swelling" behavior is necessary to accurately reproduce the characteristic "S-shape" in dew curves that exhibit DRV.

The number densities of CO_2 in the vapor phase and heavy components in the liquid phase show monotonic behavior across the entire pressure range. Predictions from EoS and GEMC simulations seem to qualitatively agree with EoS correlations, where the most accurate agreement is found for GEMC simulations. On the other hand, highly non-linear behavior is observed for the heavy components in the vapor phase. Similar to the results obtained for butane isomers in methane mixtures, the number densities of n-alkanes and arenes in the vapor phase are determined by their volatilities. For example, the number densities of benzene in the vapor phase that are larger than for the other two arenes, which yields dew curves with lower CO_2 mole fractions. The sharp increase in vapor phase number densities of heavy components is again observed in the same pressure range where CO_2 "swelling" in the liquid phase is observed, suggesting these two are correlated. GEMC simulations predict this sharp increase for mixtures with both types of heavy components,

where again the most accurate descriptions were found for explicit-hydrogen models. In contrast, PC-SAFT and PR EoS predictions underestimate the number densities of heavy components in the vapor phase, and in the case of PC-SAFT do not predict a number density increase at high pressures. Therefore, better descriptions of the number densities of heavy components in the vapor phase and of the low-boiling compound in the liquid phase are necessary to improve the modeling performance of PC-SAFT and PR EoS for these mixtures at near-critical conditions.

5.3.7 Free energy of Transfer in CO_2-based Systems

Following a similar analysis approach as for methane mixtures, Equation 5.2 was used to compute number densities for CO_2 binary mixtures. Figures 5.18 and 5.19 show ΔG_t values obtained from EoS and GEMC simulations across the full range of reduced pressures. In both figures, the top panels show that CO_2 exhibits non-linear ΔG_t behavior at high pressures for EoS correlations and GEMC simulations. In contrast, predictions from PC-SAFT and PR EoS show ΔG_t behavior that is more monotonic towards high pressures. This deviation from EoS correlations is expected given the considerable deviations observed for number densities in Figures 5.16 and 5.17. As with other properties, GEMC simulations provide qualitative predictions for CO_2 in mixtures with n-alkanes, while much more accurate predictions were found for arenes. For the heavy components, both EoS and GEMC predictions are in good qualitative agreement, despite the considerable deviations found for ΔG_t values from PC-SAFT predictions. Predictions from GEMC simulations are in good agreement with the results obtained for methane mixtures, where the non-linear behavior is observed only for ΔG_t values for the low-boiling compound. This result reaffirms that DRV is strongly linked to a change in the phase behavior of the low-boiling compound at near-critical conditions.

5.3.8 Structural Analysis of CO_2-based Systems

As mentioned in Section 5.3.4, molecular packing is strongly linked to non-linear VLE behavior in systems that exhibit DRV. To analyze the structural changes that influence DRV in CO_2/hydrocarbon binary mixtures, center of mass RDFs were computed across the full range of reduced pressures. Selected RDFs for CO_2/benzene mixtures are shown in Figure 5.20 for a reduced pressure range of 0.2 (black lines) and 0.7 (violet lines). Compared to RDFs from methane mixtures, these results show that molecular packing is different for

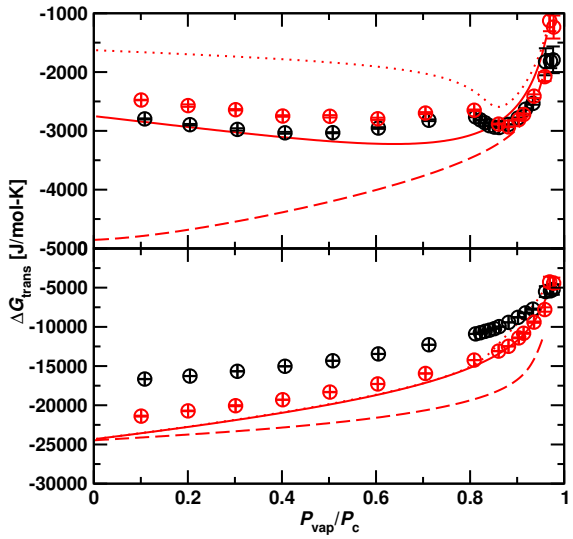

Figure 5.18: Gibbs free energy of transfer for CO_2 (top) and n-alkanes (bottom). Color scheme and symbols defined in Figure 5.12.

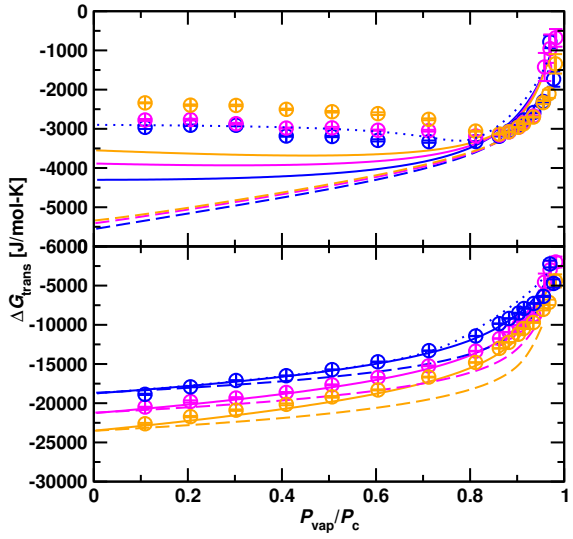

Figure 5.19: Gibbs free energy of transfer for CO_2 (top) and arenes (bottom). Color scheme and symbols defined in Figure 5.13.

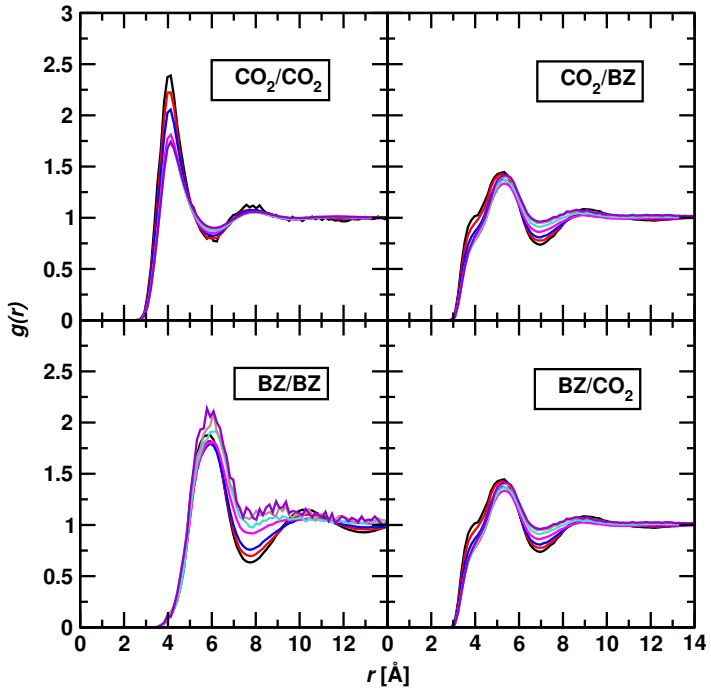

Figure 5.20: Liquid phase radial pair distribution functions for different molecule pairs in CO_2/benzene binary mixtures at various reduced pressures between 0.2 (black lines) and 0.7 (violet lines).

the relatively larger molecules investigated here. Molecular packing for CO_2-CO_2 shows very similar behavior to CH_4-CH_4 RDFs, where the first peak gradually decreases with pressure as the liquid phase becomes more compressible and disordered. On the other hand, RDFs for unlike pairs show a shoulder at closer distances, a feature not observed in RDFs for molecule pairs with the relatively smaller butane molecules in Figure 5.7. This shoulder at smaller distances is a result of the various molecular packing orientations available for benzene molecules,[161] which has also been observed for long-chain linear alkanes.[172]

The heights of RDF peaks from Figure 5.20 were analyzed as a function of reduced pressure, and results are shown in Figure 5.21. The peak height evolution for pairs that include CO_2 molecules all show a gradual decrease from low to moderate pressures, while the peak height for like hydrocarbon pairs remains nearly constant in this pressure range. At high pressures, the sharp increases in peak heights indicate that the molecular structure

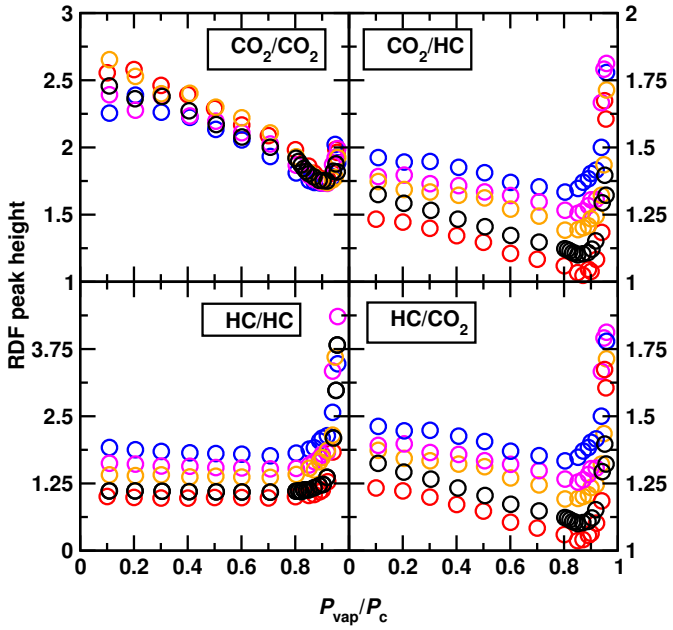

Figure 5.21: Peak heights of liquid phase radial distribution functions for different molecule pairs as a function of reduced pressure. Color scheme defined in Figures 5.12 and 5.13 for binary mixtures with different hydrocarbons (HC).

of the liquid phase is strongly influenced by the transition to critical behavior. Therefore, these results reaffirm that there exists a direct link between phase behavior and molecular structuring for systems that exhibit DRV, where the liquid phase undergoes a structural transition as the critical region is approached. Based on the results from both methane-based and CO_2-based mixtures, these structural transitions are not system specific, but rather a general feature of systems that exhibit DRV.

In addition to RDFs, the number integrals were also analyzed for all CO_2/hydrocarbon binary mixtures. The number integrals for the CO_2/benzene RDFs in Figure 5.20 are shown in Figure 5.22. The results for number integrals show a general trend similar to the results found for methane mixtures: the number integrals for CO_2 around either molecule shows an increase with pressure, whereas their benzene counterpart show a gradual decrease. This result is expected as the composition of both coexisting phases becomes more concentrated in CO_2 with increasing pressure. A closer look is provided in Figure 5.23, where

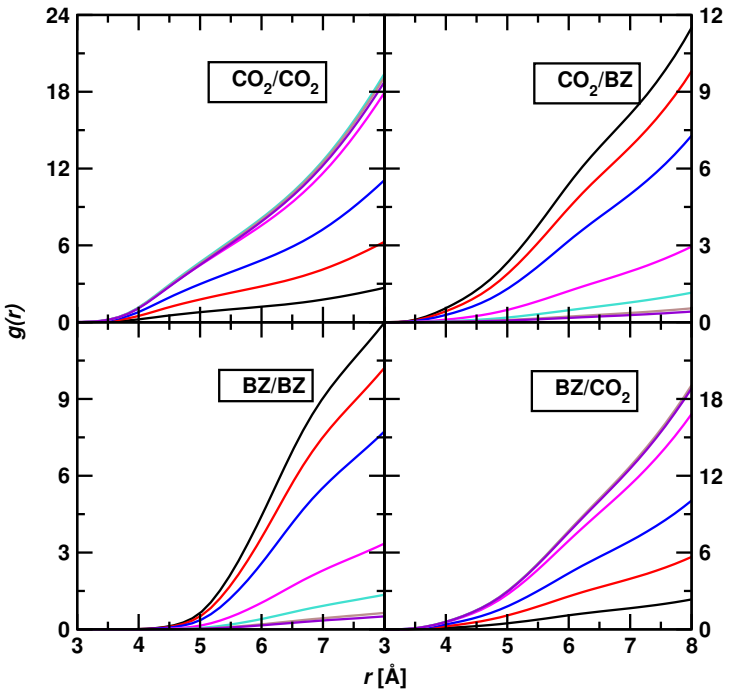

Figure 5.22: Liquid phase number integrals for different molecule pairs in CO_2/benzene binary mixtures at various reduced pressures between 0.2 (black lines) and 0.7 (violet lines).

the value of the number integral for the first solvation shell is shown as a function of reduced pressure. These results are again in close agreement with the results obtained for methane mixtures, where the evolution of number integrals recovers the general trends found for number densities. The “swelling” effect found for the liquid phase number densities of CO_2 is reflected in the number integral of the first solvation shell for pairs with CO_2 around a given molecule. On the other hand, the amount of hydrocarbon in the first solvation shell is found to decrease proportionally with the number densities of its respective hydrocarbon in the liquid phase. These results are also in agreement with the results obtained for methane mixtures, where the structural effects associated with DRV are observed within the first solvation shells of molecule-molecule pairs.

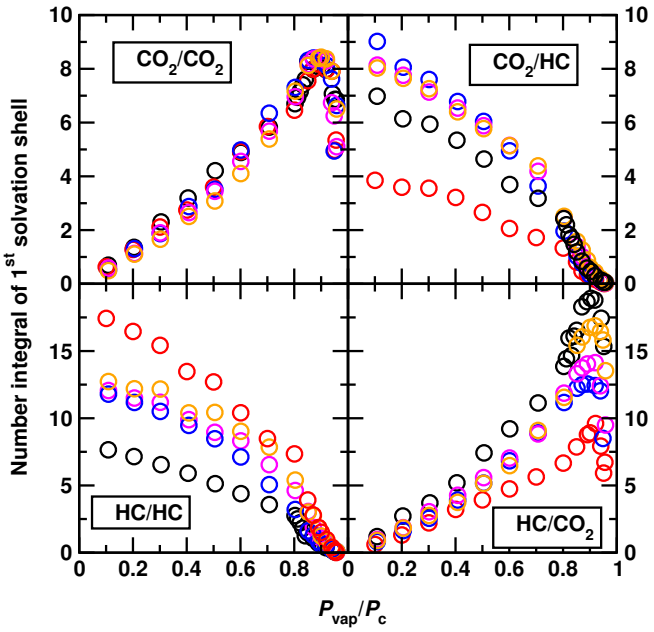

Figure 5.23: Liquid phase number integrals of the first solvation shell for different molecule pairs as a function reduced pressure. Color scheme defined in Figures 5.12 and 5.13 for binary mixtures with different hydrocarbons (HC).

5.4 Conclusions

Double retrograde vaporization has been successfully modeled using equations of state and Gibbs ensemble Monte Carlo simulations for a variety of fluid mixtures relevant to gas condensate reservoirs and enhanced oil recovery. It was found that the Peng Robinson equation of state and PC-SAFT both provide satisfactory predictions of VLE properties for near-critical methane + (n-butane and/or i-butane) mixtures, where DRV dependence on the relative amounts of heavy components was described properly. On the other hand, both EoS showed limited performance in predicting DRV for CO_2/hydrocarbon binary mixtures, where deficiencies in descriptions of CO_2-molecule interactions hinder their predictive capabilities. To account for these deficiencies in CO_2 mixtures, non-zero k_{ij} parameters were required to properly correlate near-critical VLE, and ultimately reproduce DRV.

In contrast to EoS, GEMC simulations using the TraPPE force field were capable of predicting DRV for all mixtures investigated, regardless of the low-boiling compound. Quantitative agreement with EoS correlations were obtained for GEMC simulations with explicit-hydrogen descriptions of arene molecules in CO_2 mixtures, whereas an overestimation of CO_2 solubility in the liquid phase was obtained for binary mixtures with united-atom descriptions of n-alkane molecules. These shortcomings of united-atom force fields did not affect their performance in methane/butane mixtures, primarily because this limitation becomes most pronounced for long-chain alkanes. For methane mixtures, DRV dependence on heavy component composition was correctly predicted, where exact quantitative agreement could be obtained by adjusting the vapor pressures of the heavy components, as described in Section 4.3.5. Additional properties, including number densities, free energies of transfer, and molecular packing were also well described by GEMC simulations. Overall, the results obtained from GEMC simulations confirm that DRV is not a system-specific phenomenon, but instead can be observed for different asymmetric mixtures, and is not limited to binary systems. Furthermore, simulation results showed that the phase behavior of the low-boiling compound and the heavy components differs strongly at near-critical conditions, and these fundamental differences must be accounted for properly in order to provide accurate descriptions of DRV.

Chapter 6

Molecular Modeling of Liquid-Liquid Equilibria in Enhanced Oil Recovery

6.1 Introduction

Capillary forces in waterflooded oil reservoirs cause large amounts of hydrocarbons to be trapped in swept reservoir zones,[17] where the high oil/water interfacial tension (IFT) hinders microscopic oil displacements.[7] For this reason, waterflooding may leave as much as 60% of the original oil in place (OOIP)[173] trapped behind within porous rock spaces, where oil droplets are often surrounded by water films that limit hydrocarbon diffusion .[174] Recovery limits due to water blocking can be overcome using CO_2 injection[10,15,175,176] to lower the viscosity of trapped oils and improve their mobility, yet sufficient quantities are not always available given the remote locations of many oil fields.[174] A promising alternative is enhanced oil recovery (EOR) based on surfactant flooding,[177–179] where surfactants and other liquid chemicals are injected into the oil reservoir to lower oil/water IFT and improve hydrocarbon mobility. Non-ionic surfactants are commonly used in chemical EOR due to their favorable oil dispersant properties and relatively low toxicities.[180] Surfactants belonging to the family of alkyl poly-(ethylene glycol) ethers (C_iE_j) can be tailored to improve the performance of chemical EOR processes by adjusting both the alkyl chain length i and the number of ethylene glycol units j. However, incorporating these compounds into EOR processes requires detailed understanding of fluid properties in surfactant systems.

Phase equilibria in multicomponent mixtures of oil, water, and non-ionic surfactants

plays an important role in the design of chemical EOR processes. Under specific conditions, these mixtures are known to exhibit phase separations that yield either one, two, or three coexisting liquid phases.[181–183] Mixtures of this type that exhibit three-liquid coexistence are characterized by isobaric temperature-composition (T-x) phase prisms containing tie-triangles within a range of temperatures between the upper critical solution temperature (UCST) of the surfactant/oil side and the lower critical solution temperature (LCST) of surfactant/water side.[184–187] The tie-triangles are surrounded by two-liquid coexistence regions on all sides, with those toward the surfactant/water and surfactant/oil sides ending in plait points. For planes of constant oil/water ratio on a T-x phase prism, the boundaries between the three- and two-phase regions and between the one- and two-phase regions are "fish" shaped.[188,189] The point where one finds a direct transition from a three- to one-phase region is known as the "X-point", which is often used to describe the efficiency of a surfactant to solubilize the same amounts of water and oil.[184] Hence, understanding these complex features is important for the development of improved surfactant formulations.

Accurately modeling phase behavior in these multicomponent systems is essential for EOR process design. Empirical and semi-empirical methods, such as group contribution methods and activity coefficient models, are commonly as modeling tools for LLE in the oil and gas industry. Three-liquid LLE has been previously modeled using free energy approaches, such as the Landau-type approach of Kleinert,[184,185,190] as well using equations of state (EoS) in combination with activity models, such as combining UNIQUAC theory[191] with the Peng-Robinson EoS.[192] Models with explicit association schemes, such as SAFT-like models[40,193] have recently gained attention for modeling LLE of multicomponent mixtures, in particular for mixtures of glycol ethers.[194–196] These types of surfactants have gained interest due to their applications in industry, as well as their relatively simple molecular structure, which makes them suitable candidates for the development of new theories with explicit intramolecular association schemes.[197] Given the complexity of non-ionic surfactant mixtures, it is not surprising that empirical and semi-empirical methods perform best for the correlation of experimental measurements but are less successful for the a priori prediction of miscibility gaps. Hence, there is a need to develop thermodynamic models that are suitable for predictive modeling of LLE in complex systems.

In contrast to empirical thermodynamic methods, molecular simulations are known to provide reliable predictions of phase equilibria for a wide range of systems and conditions. More importantly, explicit descriptions of molecular interactions allows for detailed insight into microscopic features with exceptional resolution. However, molecular simulations of

systems that exhibit liquid miscibility gaps and aggregation in one or more liquid phases are very challenging because direct transfers of molecules between liquid phases are rarely successful and changes in the size distribution of aggregates occur very slowly.[198] In addition, the excess free energies governing liquid-liquid equilibria are much smaller than those found for vapor-liquid equilibria, and this places a tremenduous burden on the accuracy of the force field. Hence, the goal of this work is to investigate the microscopic details governing the performance of Gibbs ensemble Monte Carlo simulations for predicting liquid-liquid equilibria (LLE) in oil/water/non-ionic surfactant systems. This simulation method has been shown to predict liquid-phase miscibility gaps for other multicomponent systems,[198–200] yet predicting the coexistence of multiple liquid phases remains a challenge. Multicomponent systems containing water, n-decane (C10), and 2-butoxyethanol (C4E1) were taken as the model systems. Emphasis is given to C4E1/C10 binary mixtures and to their phase behavior when water is introduced to the system. Analysis of simulation trajectories provide information on liquid-phase microheterogeneities and their influence on simulation performance.

6.2 Simulation Details

Binary and ternary systems of water, n-decane, and C4E1 were simulated using the Gibbs ensemble Monte Carlo[57,59,67] (GEMC) simulations in the isobaric-isothermal ensemble. The MCCCS–MN program[74] developed by the Siepmann group was used to carry out all GEMC simulations. Different phases were modeled by using separate simulation boxes, which eliminates the need to explicitly simulate fluid interfaces. The simulation boxes are thermodynamically connected by exchanging particles between the phases using configurational-bias Monte Carlo (CBMC) particle transfer moves.[60,61,66] The system pressure is maintained fixed by independently performing volume moves on each simulation box. Water molecules were represented using the TIP4P model,[73] while the Transferable Potentials for Phase Equilibria (TraPPE) force field[69,201] was used to describe n-decane and C4E1 molecules. Nonbonded parameters for all unlike interactions were determined using Lorentz-Berthelot combining rules.[99] A spherical cutoff of 1.0 nm was used with analytical tail corrections to estimate Lennard-Jones interactions beyond this distance. Coulomb interactions were treated using the Ewald summation technique.[54]

For simulations of one- and two-liquid phase regions, a total of three simulation boxes were used: two boxes simulating liquid phases and one box simulating a vapor phase

which was included as an intermediate for particle transfers in order to improve their acceptance rates. Simulations for C4E1/C10 binary systems were performed using 280 C4E1 molecules, 160 C10 molecules, and 2 molecules of each impurity: C3E1, C1E1, methanol, n-octane, n-hexane, n-butane, and ethane. These impurities were used to enhance the transfer of C4E1 and C10 molecules between simulation boxes with CBMC particle identity switch moves,[202] where biasing potentials were used to ensure that impurities distribute roughly evenly between the three phases.[198,200] The number of C4E1 and C10 molecules were chosen to yield an overall C4E1 mass fraction of nearly 0.6 for the binary system, which is equivalent to a C4E1 mole fraction of about 0.64. Simulations of ternary systems in the two-liquid region were performed using the same number of C4E1, C10, and impurity molecules in addition to 345 water molecules, which yields an overall water mass fraction of about 0.1 while maintaining the same C4E1:C10 ratio as in the binary systems. Addition of water molecules to the C4E1/C10 system allows for a detailed view of the microscopic features influenced by the inclusion of additional hydrogen bonding environments. Simulation results for two-liquid systems were complemented with preliminary results for the three-liquid region using GEMC simulations with a total of 4 simulation boxes, as well as with experimental measurements from Negahban $et\ al.$[203] Both of these additional data sets were determined at a fixed temperature and pressure of 298 K and 1 bar, respectively.

Due to the slow system relaxation in liquid-liquid simulations, sampling efficiency was optimized by adjusting the fraction of MC moves such that on average 1 volume and 1 particle swap move were accepted per MC cycle.[110] The fraction of MC moves allowed for CBMC regrowths, translations, and rotations were evenly distributed for flexible molecules. Averages and trajectories were taken from 8 independent runs for each simulation, where independent simulations for binary systems consisted of 2×10^6 MC cycles, while the simulation length for ternary systems consisted of 1×10^6 MC cycles. Each MC cycle consists of N moves, where N is the total number of particles in the system. All simulations were performed at a constant pressure of 1 bar, where the temperature in simulations of ternary systems was set to 298 K while three temperatures were simulated for binary systems : 298 K, 318 K, and 338 K. In addition to providing compositions of coexisting phases, microheterogeneity and fluid structure was analyzed using radial distribution functions from each liquid box for specific pseudoatom pairs.

6.3 Results and Discussion

6.3.1 Binary Mixtures

Given that the existence of a three-liquid region exists above the UCST of the surfactant/oil side, simulations using two liquid boxes for the C4E1/C10 binary system are expected to show convergence towards a single liquid phase at temperatures equal to or lower than those which exhibit three liquid phases in coexistence. Given that the aim of this work is to assess the three-liquid region at ambient temperature and pressure, trajectories for simulation at $T = 298$ K are given in Figure 6.1 for all 8 independent runs. These results show the progression of this set of simulations after 2×10^6 MC cycles. As seen from the start of the simulations, each box was initialized using C4E1 mole fractions of about 0.8 and 0.45. The choice of initial miscibility gap was based on the location of the plait point near the C4E1/C10 side determined Negahban $et\ al.$[203] for the ternary system at 298 K and 1 bar. The initial compositions were estimated such that the experimental plait point

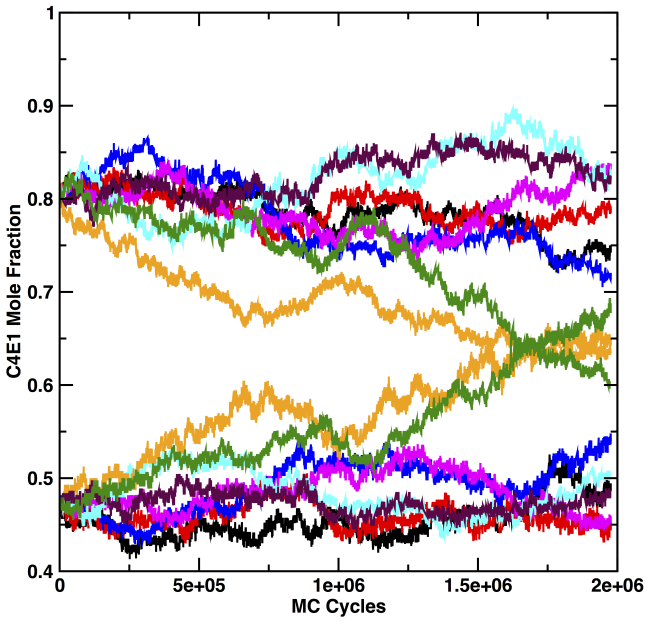

Figure 6.1: Evolution of C4E1 mole fraction in C4E1/C10 binary mixtures at 298 K from 8 independent simulations. Colors denote pairs of liquid boxes for a single independent run.

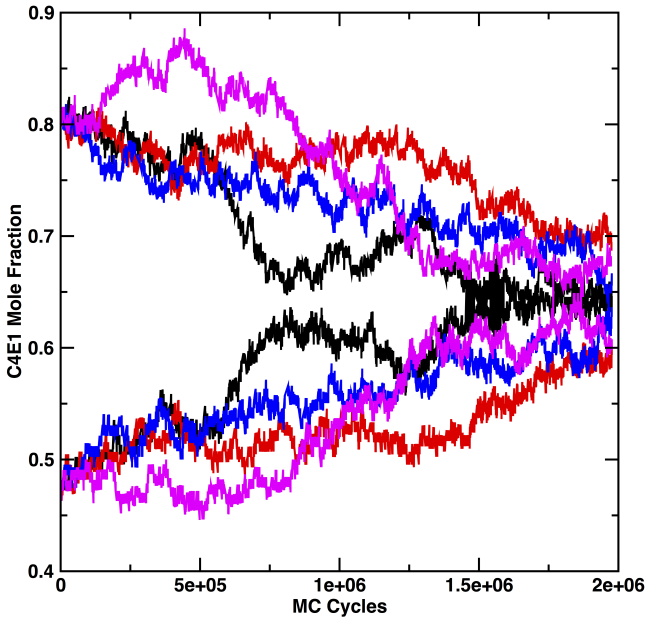

Figure 6.2: Evolution of C4E1 mole fraction in C4E1/C10 binary mixtures at 318 K from 4 independent simulations. Colors denote pairs of liquid boxes for a single independent run.

is in between the initial composition limits with respect to the C4E1/C10 side, which corresponds to a nearly equimolar mixture of C4E1 and C10. The simulation trajectories at 298 K indicate that two of eight independent runs converged to the overall C4E1 composition in both liquid boxes after 1.5×10^6 MC cycles, suggesting both boxes are sampling a single liquid phase. The mole fraction evolution shows convergence between both liquid boxes is very slow, where most of the remaining independent runs show only slight deviations from their initial compositions after 2×10^6 MC cycles, particularly for the box initialized with a higher decane fraction. These results suggest that simulation lengths of 2 million cycles are not sufficiently long to yield a single liquid phase for this binary system when the system is initialized with a considerably large miscibility gap. Therefore, one may easily conclude that a particular force field erroneously predicts a liquid-liquid miscibility gap when averaged over relatively short production periods. Recent studies using GEMC simulations for LLE in systems with similar components have been reported using relatively short production periods in the order of 10^4 to 10^5 MC cycles.[204,205] Therefore, LLE predictions using GEMC simulations for complex systems, such as in alcohol/water/n-alkane

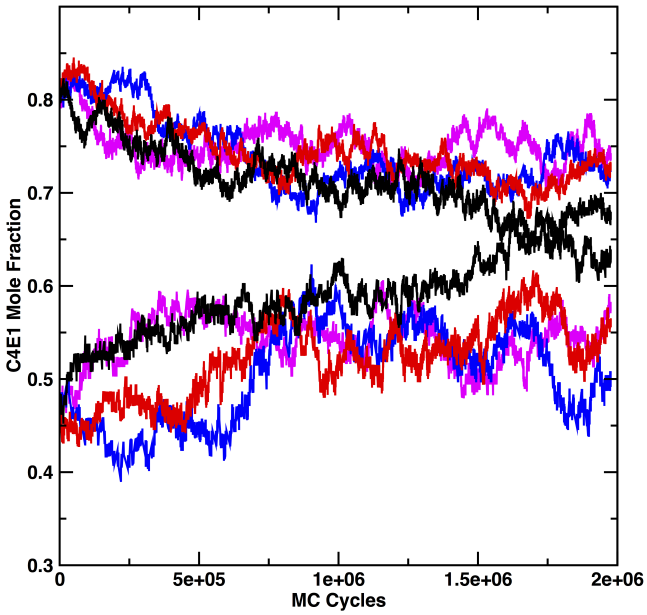

Figure 6.3: Evolution of C4E1 mole fraction in C4E1/C10 binary mixtures at 338 K from 4 independent simulations. Colors denote pairs of liquid boxes for a single independent run.

mixtures,[206] require a relatively large number of MC cycles to ensure proper equilibration.

While simulations of C4E1/C10 mixtures at 298 K equilibrate very slowly, it is reasonable to expect that simulations at higher temperatures will converge at a faster rate, partly due to increased particle transfer acceptance rates as well as being well above the predicted UCST where only one liquid phase exists. Figures 6.2 and 6.3 show simulation trajectories at 318 K and 338 K, respectively. For clarity, trajectories from 4 independent simulations are provided. Trajectory results show that both liquid boxes have a greater overall tendency to converge than for simulations at 298 K. In particular, the composition of the "decane-rich" liquid box shows a faster rate of composition change than for most of the simulations in Figure 6.1, indicating the convergence in this simulation box has a strong influence on the overall convergence. Nonetheless, allowing simulations to run for 2×10^6 MC cycles was still insufficient to observe convergence across all independent runs. Therefore, longer simulations would be required to achieve full convergence to one liquid phase with two liquid boxes of equal compositions. Overall, the trajectories of simulations

for all three temperatures suggest that the TraPPE force field is capable of predicting a single liquid phase for C4E1/C10 binary mixtures provided sufficient MC cycles are allowed. In this regard, the UCST of C4E1/C10 mixtures predicted by the TraPPE force field must be below 298 K, in agreement with experimental measurements.[203]

6.3.2 Ternary Mixtures

Using a similar two-liquid setup as for C4E1/C10 binary mixtures, a tie line for the two-liquid region was computed at $T = 298$ K using an overall water content of 10% by mass. This set of simulations was initialized using compositions obtained from Negahban $et\ al.$[203] Simulation trajectories for 4 independent runs are shown in Figure 6.4. The results indicate that the amount of water in both phases is considerably stable over a span of 1×10^6 MC cycles, suggesting the partitioning of water is not a limiting factor given that one of the liquid boxes has a relatively large decane content. However, the trajectories of compositions

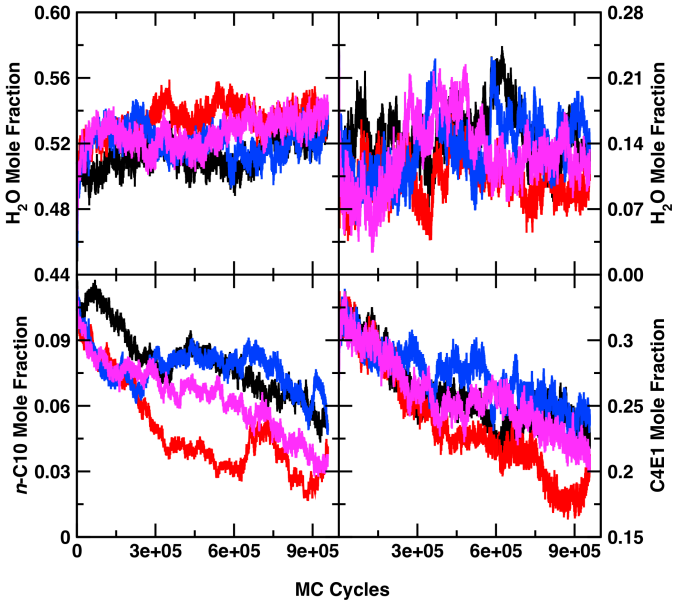

Figure 6.4: Evolution of water (top), C4E1 (bottom right), and n-C10 (bottom left) mole fractions in C4E1 rich (left) and n-C10 rich (right) phases at 298 K. Colors denote separate independent runs.

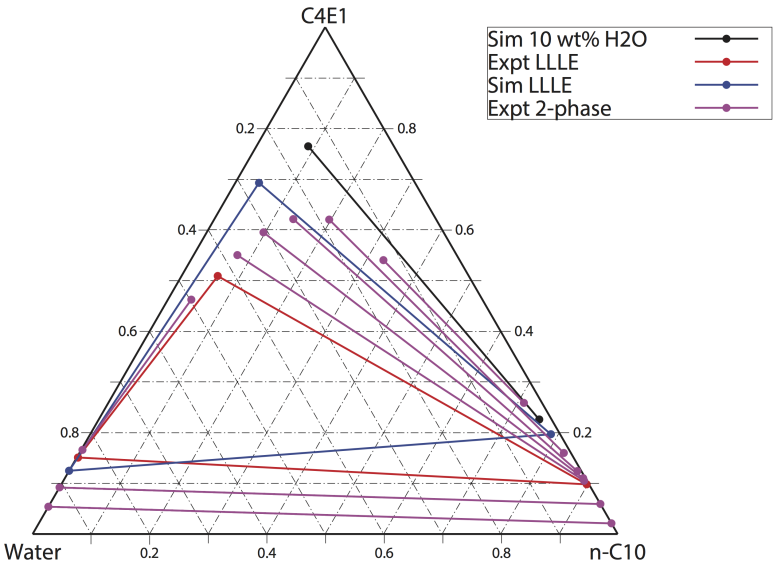

Figure 6.5: Ternary phase diagram at 298 K. Coexisting liquid phases denoted by tie lines (2 phases) and tie triangles (3 phases). Compositions provided as mass fractions.

for minority components in each liquid box suggest that there is a slow yet consistent drift from initial compositions, indicating that more MC cycles are required before these compositions level off at equilibration. This finding is similar to that of C4E1/C10 binary systems, where the composition of C4E1 in the decane-rich phase phase was slow to equilibrate and hindered the overall convergence rate. In this case, the amount of decane in the surfactant-rich phase also shows slow convergence. Nonetheless, the trajectories seem to indicate that these simulations predict a miscibility gap for this specific ternary mixture.

To assess the performance of these simulations in comparison to the global ternary phase diagram, mass fractions for this ternary system were averaged over the final 1×10^5 MC cycles for all 8 independent runs, thereby eliminating composition drifts from the early stages of the simulations. The predicted tie-line is shown in Figure 6.5, in addition to preliminary results for GEMC simulations of the three-liquid region and experimental measurements of Negahban $et\ al.$[203] The results show that the simulated tie-line is much wider than those found in experiments, yet they are in good qualitative agreement when compared to simulation results for the three-liquid region. Given that the predicted tie-triangle is much larger than that of Negahban $et\ al.$, it is not surprising that tie-lines near

the C4E1/C10 side exhibit a similarly wide miscibility gap. Experimental measurements suggest a relatively sharp narrowing of tie-lines towards the C4E1/C10 side, which is expected for simulations as well given the results discussed in Section 6.3.1. This result indicates that GEMC simulations employing TIP4P/TraPPE force fields are capable of describing phase equilibria with multiple liquid phases, where the influence of water content on the number of coexisting phases is qualitatively predicted and in good agreement with rexperimental measurements. It is important to note that providing at least one separate simulation box for each coexisting liquid phase was required, where the three-liquid region required a total of 4 boxes.

6.3.3 Microheterogeneity and Structural Analysis

Given that fluid structure directly influences phase equilibria, analyzing molecular packing in liquid phases allows for investigating the microscopic features that control simulation

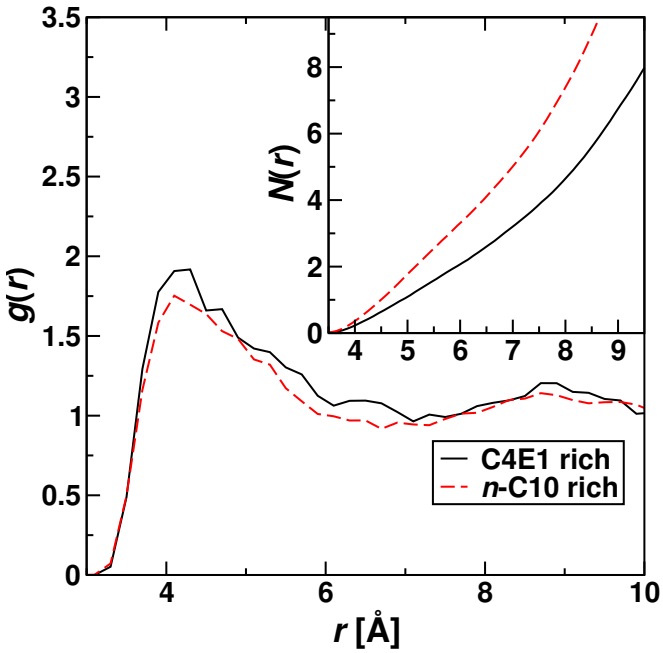

Figure 6.6: CH_3(C10)-CH_3(C10) radial distribution functions in C4E1/n-C10 binary system at 298 K. Number integrals provided in the inset.

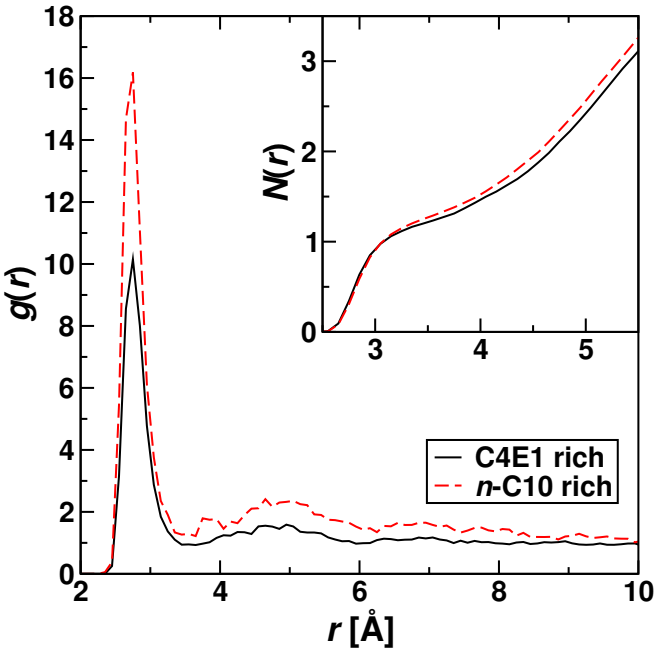

Figure 6.7: O(hydroxyl)-O(hydroxyl) radial distribution functions in C4E1/n-C10 binary system at 298 K. Number integrals provided in the inset.

performance. Trajectories for simulations of C4E1/C10 binary mixtures showed that liquid miscibility was not observed for all independent runs, suggesting that there must be structural differences between separate runs. Because microheterogeneity and aggregate formation is a common feature of surfactant mixtures, site-site radial distribution functions (RDF) were generated for simulations performed at $T = 298$ K to analyze the spatial distribution of specific interaction sites. Figure 6.6 shows the packing behavior of decane molecules in C4E1/C10 binary mixtures provided by RDFs for pairs of CH_3 units in both liquid boxes. These results indicate that decane molecules pack very similarly in both liquid boxes despite yielding slightly different number integrals in each box, where the "C4E1-rich" box shows a lower average of C10 pairs around a central C10 molecule. This is not surprising given that trajectories of several independent runs show miscibility gaps in binary mixtures after 2×10^6 MC cycles, where decane molecules distribute unevenly between phases . These number integrals should become increasingly similar as all independent runs converge towards liquid phase miscibility. The opposite trend is found for RDFs of hydroxyl oxygen pairs in surfactant molecules, which are given in Figure 6.7.

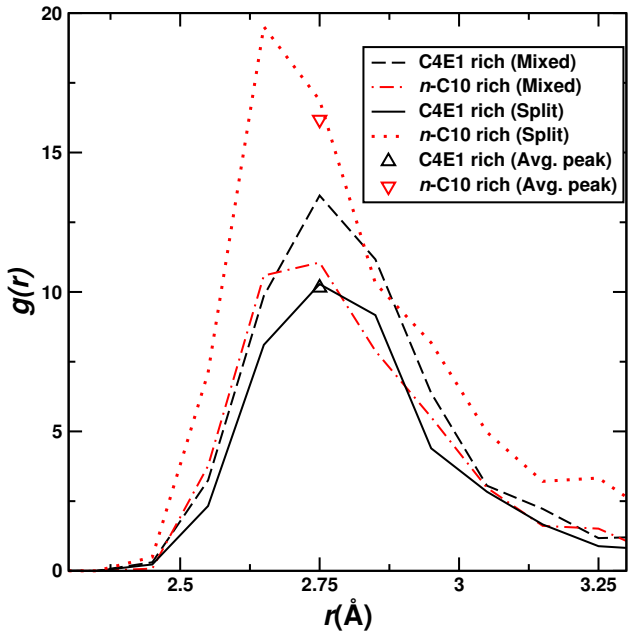

Figure 6.8: O(hydroxyl)-O(hydroxyl) radial distribution functions in C4E1/n-C10 binary system at 298 K for two independent runs with different mixing behavior. Triangles denote RDF peak heights averaged from 8 independent simulations.

The RDF peak height for these pairs indicate that there is clustering of C4E1 molecules in both liquid boxes, yet surfactant molecules appear to show stronger aggregation behavior in "C10-rich" phases. Similar to RDFs of decane pairs, the packing behavior of C4E1 molecules is expected to be equivalent in both boxes for systems that exhibit liquid phase miscibility. The difference in packing behavior between simulations whose liquid phases "mix" and those that exhibit miscibility gaps can be seen by analyzing RDFs for independent simulations. Figure 6.8 shows a close-up view of the oxygen-oxygen RDF peaks from two independent runs with different "mixing" behavior. The peak heights for systems that exhibit miscibility are quite similar, as opposed to the large peak height differences observed for simulation with miscibility gaps. This result indicates that liquid phase miscibility is obtained when both phases exhibit equivalent packing arrangements and therefore the average RDFs should become similar between both boxes as more independent runs exhibit convergence in compositions.

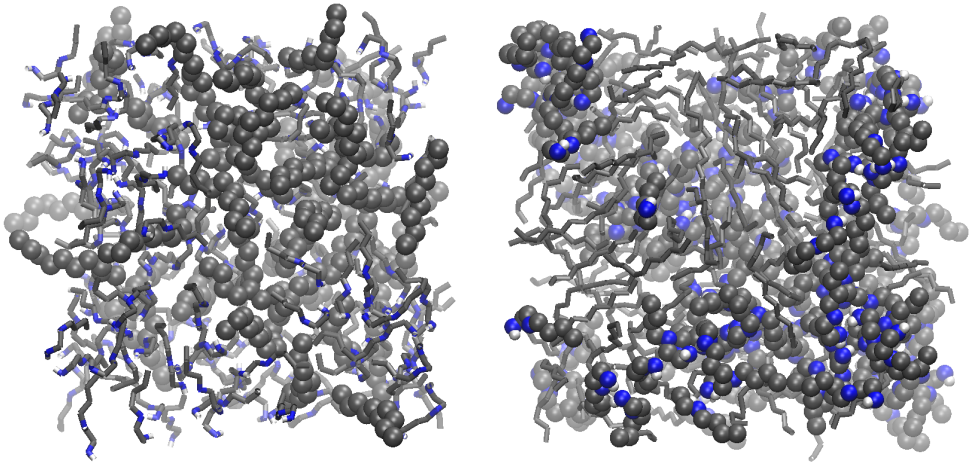

Figure 6.9: Snapshot of C4E1 rich phase (left) and n-C10 rich phase (right) in binary mixtures at 298 K. Colors denote surfactant O atoms (blue), H atoms (white), and CH_x pseudoatoms (gray). Minority components depicted by bead chains.

The strong clustering observed in binary mixtures is a consequence of hydrogen bonding between surfactant molecules, where polar interactions favor the formation of C4E1 aggregates in the absence of favorable hydrogen-bonding environments within decane-rich phases. Therefore, transferring surfactant molecules between liquid phases is mostly limited to regions of favorable hydrogen-bonding environments, suggesting that the persistence of surfactant clusters in decane-rich phases is responsible for the slow mole fraction evolution in this box, as shown in Figure 6.1. Visual inspection of the snapshots provided in Figure 6.9 confirm the differences in packing environments between the two separate liquid boxes. The snapshots reveal that while decane molecules are well dispersed within the C4E1-rich box, surfactant molecules form hydrogen-bonded clusters in the decane-rich box. Free-floating surfactant monomers in the C10-rich phase that are stabilized by intramolecular hydrogen bonding provide available sites for cluster growth, yet this also requires disruption of hydrogen bonded networks elsewhere in the system. Hence, these results suggest that the rate of mole fraction evolution is directly linked to surfactant aggregate formation in C10-rich phases. As temperature is increased, particle transfers and displacements also increase and overcome clustering restrictions, yielding faster equilibration periods.

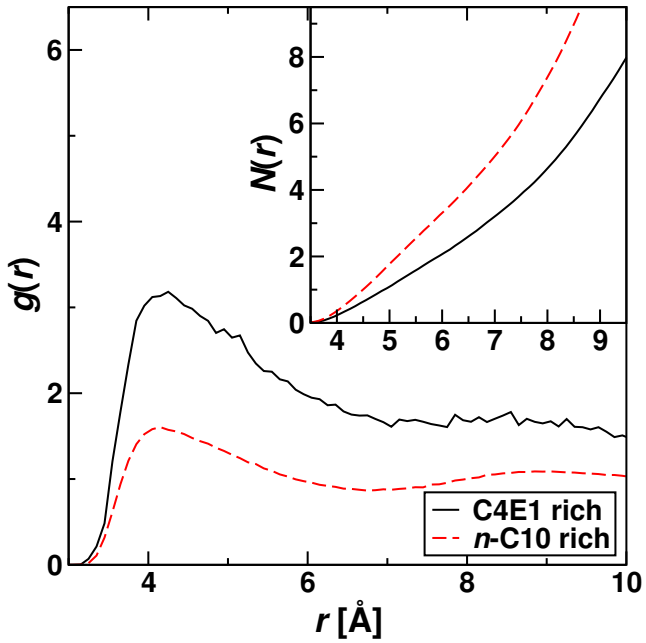

Figure 6.10: CH_3(C10)-CH_3(C10) radial distribution functions in ternary system at 298 K. Number integrals provided in the inset.

Inclusion of water molecules in the system provides additional hydrogen-bonding sites within each phase, yet the equilibration of minority components in each phase is still quite slow. The RDFs for CH_3 unit pairs in Figure 6.10 indicate that packing between C10 molecules is quite different in each phase, where the peak height of in the C4E1-rich phase is relatively large while its number integral is small. This finding suggests that the few decane molecules found in the C4E1-rich phase prefer to pack closer than in the decane rich phase due to the relatively larger amount of polar interactions coming from water and C4E1 molecules. This difference in packing behavior contrasts with the RDFs between CH_3 units in binary systems, consistent with the 2-liquid phase split observed for the ternary system. Despite adding hydrogen-bonding environments to the decane-rich phase by inclusion of water molecules, C4E1 mole fractions were still evolving slowly in this phase throughout the length of the simulation. The RDFs in Figure 6.11 for hydroxyl oxygen pairs show that there is very strong surfactant aggregation in the C10-rich phase in comparison to the surfactant-rich phase, where the peak height is much smaller. This result indicates that the addition of water does not promote faster equilibration periods because surfactant

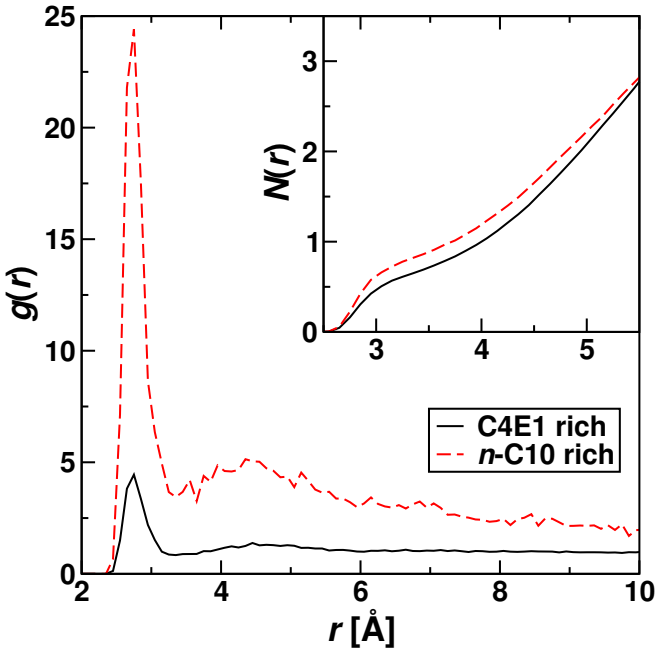

Figure 6.11: O(hydroxyl)-O(hydroxyl) radial distribution functions in ternary system at 298 K. Number integrals provided in the inset.

aggregate formation in the C10-rich phase is still largely persistent, and more so than for binary mixtures due to the relatively wide two-liquid phase split shown in Figure 6.5. Visual inspection of the C10-rich phase in Figure 6.12 reveals that water molecules promote the formation of micelle-like aggregates, where the inner portion is filled with water molecules that are surrounded by the polar head groups of C4E1 molecules. In contrast, aggregates in the C4E1-rich box are not as well defined. Therefore, water and surfactant molecules transferred into the C10-rich phase contribute to the growth and shrinkage of micelle-like aggregates by preferentially transferring into hydrogen-bonding regions. Because growth processes, such as Ostwald ripening,[207,208] may contribute to system equilibration by formation of larger micelles, it may be necessary to increase the total number of molecules to allow the growth of sufficiently large micelle-like aggregates in order to obtain better quantitative agreement with experimental measurements. Nonetheless, the good qualitative agreement obtained with experiment and internal consistency of GEMC simulation results suggests that the combination of TIP4P water with the TraPPE force field provides accurate descriptions of the molecular interactions and packing arrangements found in these

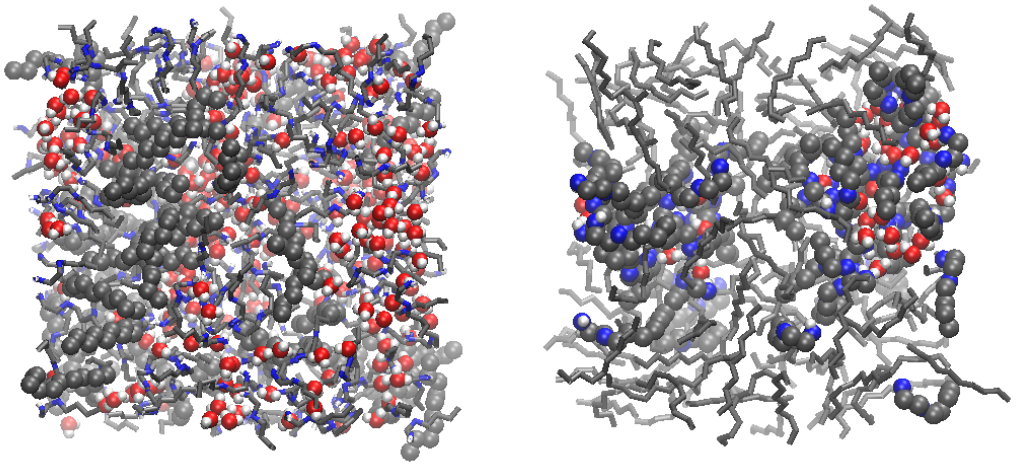

Figure 6.12: Snapshot of C4E1 rich phase (left) and n-C10 rich phase (right) in ternary mixtures at 298 K. Colors denote surfactant O atoms (blue), water O atoms (red), H atoms (white), and CH_x pseudoatoms (gray). Minority components depicted by bead chains.

complex multicomponent systems.

6.4 Conclusions

Isobaric-isothermal GEMC simulations were successfully carried out for binary and ternary liquid mixtures containing water, C4E1, and n-decane, where the interactions of alkanes and surfactants were described by the TraPPE–UA force field, and the TIP4P model was used for water. Using a two-liquid box setup, simulations were shown to predict liquid phase miscibility for C4E1/C10 binary mixtures at temperatures of 298 K, 318 K, and 338 K and at a constant pressure of 1 bar. Simulations of 2×10^6 MC cycles showed to be sufficiently long to allow C4E1 mole fraction convergence between both liquid boxes for several independent runs, whereas the remaining runs showed an increasing tendency towards convergence as temperature was increased farther above the mixture's UCST. Analysis of molecular packing reveals hydrogen-bonding between surfactant molecules in the oil-rich phase is responsible for the slow convergence, where C4E1 molecules showed substantial clustering behavior in the absence of hydrogen-bonding environments. This aggregation behavior was also observed for simulations of two-liquid ternary systems at

298 K, where the C4E1 aggregates in the decane-rich phase provided a favorable amount hydrogen-bonding sites for water molecules being transferred to this phase, contributing to the formation of water-filled micelle-like aggregates. Therefore, equilibration in these systems was found to be hindered by the persistence of hydrogent-bonded clusters in the decane-rich phase. Likewise, the surfactant-rich phase showed slow equilibration in terms of decane composition for ternary systems due to the large presence of polar interactions. Nonetheless, GEMC simulations were capable of qualitatively predicting the global phase diagram for this complex system, yielding systems with one, two, and three coexisting liquid phases similar to the experimental measurements of Negahban $et\ al.$[203] These results provide excellent guidance for simulating multicomponent systems of similar composition using GEMC simulations, where the force field selection, system size, number of simulation boxes, and simulation lengths need to be carefully taken into account in order to provide adequate descriptions of the complex fluid behavior found in liquid-liquid equilibria of water/oil/surfactant mixtures.

References

[1] Kim, S.; Dale, B. E. *Biomass Bioenergy* **2004**, *26*, 361–375.

[2] Reddy, K. G.; Deepak, T. G.; Anjusree, G. S.; Thomas, S.; Vadukumpully, S.; Subramanian, K. R. V.; Nair, S. V.; Nair, A. S. *Phys. Chem. Chem. Phys.* **2014**, *16*, 6838–6858.

[3] Lewis, N. S.; Nocera, D. G. *PNAS* **2006**, *103*, 15729–15735.

[4] *International energy outlook 2013 with projections to 2040*; US Department of Energy, Energy Information Administration: Washington, D.C., 2013.

[5] Sloan, E. D. *Nature* **2003**, *426*, 353–363.

[6] Chew, K. J. *Phil. Trans. R. Soc. A* **2014**, *372*, 20120324.

[7] Muggeridge, A.; Cockin, A.; Webb, K.; Frampton, H.; Collins, I.; Moulds, T.; Salino, P. *Phil. Trans. R. Soc. A* **2014**, *372*, 20120320.

[8] Sandrea, I.; Sandrea, R. *Oil Gas J.* **2007**, *105*, 44–47.

[9] MacDowell, N.; Florin, N.; Buchard, A.; Hallett, J.; Galindo, A.; Jackson, G.; Adjiman, C. S.; Williams, C. K.; Shah, N.; Fennell, P. *Energy Environ. Sci.* **2010**, *3*, 1645–1669.

[10] Damiani, D.; Litynski, J. T.; McIlvried, H. G.; Vikara, D. M.; Srivastava, R. D. *Greenhouse Gas. Sci. Technol.* **2012**, *2*, 9–16.

[11] Figueroa, J. D.; Fout, T.; Plasynski, S.; McIlvried, H.; Srivastava, R. D. *Int. J. Greenh. Gas Control* **2008**, *2*, 9–20.

[12] Artola, P.-A.; Pereira, F. E.; Adjiman, C. S.; Galindo, A.; Müller, E. A.; Jackson, G.; Haslam, A. J. *Fluid Phase Equilib.* **2011**, *306*, 129–136.

[13] Pedrosa, N.; Szczepanski, R.; Zhang, X. *Fluid Phase Equilib.* **2013**, *359*, 24–37.

[14] Stalkup Jr., F. *J. Petrol. Technol.* **1983**, *35*.

[15] Luo, P.; Zhang, Y.; Wang, X.; Huang, S. *Energy Fuels* **2012**, *26*, 2124–2135.

[16] Christensen, J.; Stenby, E.; Skauge, A. *SPE Reserv. Eval. Eng.* **2001**, *4*, 97 – 106.

[17] Zhang, H.; Dong, M.; Zhao, S. *Energy Fuels* **2010**, *24*, 1829–1836.

[18] Ungerer, P.; Lachet, V.; Tavitian, B. *Oil Gas Sci. Technol.* **2006**, *61*, 387–403.

[19] Span, R.; Wagner, W. *Int. J. Thermophys.* **2003**, *24*, 41–109.

[20] Span, R.; Wagner, W. *Int. J. Thermophys.* **2003**, *24*, 1–39.

[21] Span, R.; Wagner, W. *Int. J. Thermophys.* **2003**, *24*, 111–162.

[22] van der Waals, J. S. R., J. D. *On the continuity of the gaseous and liquid states*; Dover Publications: Mineola, N.Y., 2004.

[23] Gubbins, K. E. *Mol. Phys.* **2013**, *111*, 3666–3697.

[24] Walas, S. M. *Phase equilibria in chemical engineering*; Butterworth: Boston, 1985.

[25] Redlich, O.; Kwong, J. N. S. *Chem. Rev.* **1949**, *44*, 233–244.

[26] Soave, G. *Chem. Eng. Sci.* **1972**, *27*, 1197–1203.

[27] Peng, D.-Y.; Robinson, D. B. *Ind. Eng. Chem. Fund.* **1976**, *15*, 59–64.

[28] Valderrama, J. O. *Ind. Eng. Chem. Res.* **2003**, *42*, 1603–1618.

[29] Wei, Y. S.; Sadus, R. J. *AIChE J.* **2000**, *46*, 169–196.

[30] Browarzik, D.; Trusler, J. P. M.; Economou, I. G.; Ely, J.; McCabe, C.; Galindo, A.; Anisimov, M. A.; Kroon, M. C.; Lemmon, E.; Bottini, S.; Brignole, E.; Pereda, S.; Kjelstrup, S.; Bedeaux, D.; Sandler, S. I. In *Applied Thermodynamics of Fluids*; Goodwin, A. R., Sengers, J., Peters, C. J., Eds.; Royal Society of Chemistry: Cambridge, 2010.

[31] Smith, J. M.; Van Ness, H. C.; Abbott, M. M. *Introduction to chemical engineering thermodynamics.*; McGraw-Hill: Boston, 2005.

[32] Rachford, H.; Rice, J. *J. Petrol. Technol.* **1952**, *4*, 19–3.

[33] Economou, I. G. *Ind. Eng. Chem. Res.* **2002**, *41*, 953–962.

[34] Chapman, W. G.; Gubbins, K. E.; Jackson, G.; Radosz, M. *Ind. Eng. Chem. Res.* **1990**, *29*, 1709–1721.

[35] Huang, S. H.; Radosz, M. *Ind. Eng. Chem. Res.* **1990**, *29*, 2284–2294.

[36] Wertheim, M. S. *J. Stat. Phys.* **1984**, *35*, 35–47.

[37] Wertheim, M. S. *J. Stat. Phys.* **1984**, *35*, 19–34.

[38] Wertheim, M. S. *J. Stat. Phys.* **1986**, *42*, 459–476.

[39] Wertheim, M. S. *J. Stat. Phys.* **1986**, *42*, 477–492.

[40] Gross, J.; Sadowski, G. *Ind. Eng. Chem. Res.* **2001**, *40*, 1244–1260.

[41] Llovell, F.; Vega, L. F. *J. Phys. Chem. B* **2006**, *110*, 11427–11437.

[42] Colina, C. M.; Turrens, L. F.; Gubbins, K. E.; Olivera-Fuentes, C.; Vega, L. F. *Ind. Eng. Chem. Res.* **2002**, *41*, 1069–1075.

[43] Blas, F. J.; Vega, L. F. *Mol. Phys.* **1997**, *92*, 135–150.

[44] Kraska, T.; Gubbins, K. E. *Ind. Eng. Chem. Res.* **1996**, *35*, 4738–4746.

[45] Kraska, T.; Gubbins, K. E. *Ind. Eng. Chem. Res.* **1996**, *35*, 4727–4737.

[46] Karakatsani, E. K.; Spyriouni, T.; Economou, I. G. *AIChE J.* **2005**, *51*, 2328–2342.

[47] Karakatsani, E. K.; Economou, I. G. *J. Phys. Chem. B* **2006**, *110*, 9252–9261.

[48] Forte, E.; Llovell, F.; Vega, L. F.; Trusler, J. P. M.; Galindo, A. *J. Chem. Phys.* **2011**, *134*, 154102.

[49] Avendaño, C.; Lafitte, T.; Galindo, A.; Adjiman, C. S.; Jackson, G.; Müller, E. A. *J. Phys. Chem. B* **2011**, *115*, 11154–11169.

[50] Maghari, A.; Hamzehloo, M. *Fluid Phase Equilib.* **2011**, *302*, 195–201.

[51] Maghari, A.; ZiaMajidi, F. *Fluid Phase Equilib.* **2013**, *356*, 109–116.

[52] Bymaster, A.; Chapman, W. G. *J. Phys. Chem. B* **2010**, *114*, 12298–12307.

[53] Siepmann, J. I.; Karaborni, S.; Smit, B. *Nature* **1993**, *365*, 330–332.

[54] Allen, M. P.; Tildesley, D. J. *Computer simulation of liquids*; Clarendon Press ; Oxford University Press: Oxford, England; New York, 1987.

[55] Metropolis, N.; Rosenbluth, A. W.; Rosenbluth, M. N.; Teller, A. H.; Teller, E. *J. Chem. Phys.* **1953**, *21*, 1087–1092.

[56] Panagiotopoulos, A. *Mol. Simul.* **1992**, *9*, 1–23.

[57] Panagiotopoulos, A.; Quirke, N.; Stapleton, M.; Tildesley, D. *Mol. Phys.* **1988**, *63*, 527–545.

[58] Frenkel, D.; Smit, B. *Understanding molecular simulation from algorithms to applications*; Academic Press: San Diego, 2002.

[59] Smit, B.; Desmedt, P.; Frenkel, D. *Mol. Phys.* **1989**, *68*, 931–950.

[60] Frenkel, D.; Mooij, G. C. a. M.; Smit, B. *J. Phys.: Condens. Matter* **1992**, *4*, 3053.

[61] Siepmann, J. I.; Frenkel, D. *Mol. Phys.* **1992**, *75*, 59–70.

[62] Mooij, G. C. a. M.; Frenkel, D.; Smit, B. *J. Phys.: Condens. Matter* **1992**, *4*, L255.

[63] Rosenbluth, M. N.; Rosenbluth, A. W. *J. Chem. Phys.* **1955**, *23*, 356–359.

[64] Laso, M.; Pablo, J. J. d.; Suter, U. W. *J. Chem. Phys.* **1992**, *97*, 2817–2819.

[65] Vlugt, T. J. H.; Martin, M. G.; Smit, B.; Siepmann, J. I.; Krishna, R. *Mol. Phys.* **1998**, *94*, 727–733.

[66] Martin, M. G.; Siepmann, J. I. *J. Phys. Chem. B* **1999**, *103*, 4508–4517.

[67] Panagiotopoulos, A. *Mol. Phys.* **1987**, *61*, 813–826.

[68] McGrath, M. J.; Siepmann, J. I.; Kuo, I.-F. W.; Mundy, C. J.; VandeVondele, J.; Hutter, J.; Mohamed, F.; Krack, M. *J. Phys. Chem. A* **2006**, *110*, 640–646.

[69] Martin, M. G.; Siepmann, J. I. *J. Phys. Chem. B* **1998**, *102*, 2569–2577.

[70] Bourasseau, E.; Haboudou, M.; Boutin, A.; Fuchs, A. H.; Ungerer, P. *J. Chem. Phys.* **2003**, *118*, 3020–3034.

[71] Bourasseau, E.; Ungerer, P.; Boutin, A. *J. Phys. Chem. B* **2002**, *106*, 5483–5491.

[72] Paluch, A. S.; Shen, V. K.; Errington, J. R. *Ind. Eng. Chem. Res.* **2008**, *47*, 4533–4541.

[73] Jorgensen, W. L.; Chandrasekhar, J.; Madura, J. D.; Impey, R. W.; Klein, M. L. *J. Chem. Phys.* **1983**, *79*, 926–935.

[74] Monte Carlo for Complex Chemical Systems - Minnesota, Version 10.1. 2010; `http://www.chem.umn.edu/groups/siepmann/software.html`.

[75] Maerzke, K. A.; Siepmann, J. I. *J. Phys. Chem. B* **2010**, *114*, 4261–4270.

[76] Dinpajooh, M.; Keasler, S. J.; Truhlar, D. G.; Siepmann, J. I. *Theor. Chem. Acc.* **2011**, *130*, 83–93.

[77] Vega, C.; Miguel, E. d. *J. Chem. Phys.* **2007**, *126*, 154707.

[78] Lísal, M.; Smith, W. R.; Nezbeda, I. *Fluid Phase Equilib.* **2001**, *181*, 127–146.

[79] Diamantonis, N. I.; Economou, I. G. *Energy Fuels* **2011**, *25*, 3334–3343.

[80] Aasberg-Petersen, K.; Stenby, E. *Ind. Eng. Chem. Res.* **1991**, *30*, 248–254.

[81] Levelt Sengers, J. M. H. *Physica A* **1975**, *82*, 319–351.

[82] Eckert, C. A.; Knutson, B. L.; Debenedetti, P. G. *Nature* **1996**, *383*, 313–318.

[83] Debenedetti, P. G. *Chem. Eng. Sci.* **1987**, *42*, 2203–2212.

[84] Pfund, D. M.; Zemanian, T. S.; Linehan, J. C.; Fulton, J. L.; Yonker, C. R. *J. Phys. Chem.* **1994**, *98*, 11846–11857.

[85] Llovell, F.; Vega, L. F.; Seiltgens, D.; Mejía, A.; Segura, H. *Fluid Phase Equilib.* **2008**, *264*, 201–210.

[86] Shin, M. S.; Lee, Y.; Kim, H. *J. Chem. Thermodyn.* **2008**, *40*, 688–694.

[87] Hansen, J.-P.; McDonald, I. R. *Theory of simple liquids*; Academic Press: Amsterdam, 2006.

[88] Tang, X.; Gross, J. *Ind. Eng. Chem. Res.* **2010**, *49*, 9436–9444.

[89] Gil-Villegas, A.; Galindo, A.; Whitehead, P. J.; Mills, S. J.; Jackson, G.; Burgess, A. N. *J. Chem. Phys.* **1997**, *106*, 4168–4186.

[90] White, J. A. *Fluid Phase Equilib.* **1992**, *75*, 53–64.

[91] Greogorowicz, J.; O'Connell, J. P.; Peters, C. J. *Fluid Phase Equilib.* **1996**, *116*, 94–101.

[92] Forte, E.; Llovell, F.; Trusler, J. P. M.; Galindo, A. *Fluid Phase Equilib.* **2013**, *337*, 274–287.

[93] Lagache, M.; Ungerer, P.; Boutin, A.; Fuchs, A. H. *Phys. Chem. Chem. Phys.* **2001**, *3*, 4333–4339.

[94] de Villiers, A. J.; Schwarz, C. E.; Burger, A. J.; Kontogeorgis, G. M. *Fluid Phase Equilib.* **2013**, *338*, 1–15.

[95] Hendriks, E.; Kontogeorgis, G. M.; Dohrn, R.; de Hemptinne, J.-C.; Economou, I. G.; Žilnik, L. F.; Vesovic, V. *Ind. Eng. Chem. Res.* **2010**, *49*, 11131–11141.

[96] Ketko, M. H.; Rafferty, J.; Siepmann, J. I.; Potoff, J. J. *Fluid Phase Equilib.* **2008**, *274*, 44–49.

[97] Colina, C.; Olivera-Fuentes, C.; Siperstein, F.; Lísal, M.; Gubbins, K. *Mol. Simul.* **2003**, *29*, 405–412.

[98] Chen, B.; Siepmann, J. I. *J. Phys. Chem. B* **1999**, *103*, 5370–5379.

[99] Maitland, G.; Rigby, M.; Smith, E. B.; Wakeham, W. A. *Intermolecular Forces: Their Origin and Determination*; Oxford University Press: Oxford, 1987.

[100] Smith, J. C.; Karplus, M. *J. Am. Chem. Soc.* **1992**, *114*, 801–812.

[101] Tobias, D. J.; Tu, K.; Klein, M. L. *J. Chim. Phys.-Chim. Biol.* **1997**, *94*, 1482–1502.

[102] Potoff, J. J.; Panagiotopoulos, A. Z. *J. Chem. Phys.* **1998**, *109*, 10914–10920.

[103] Okumura, H.; Yonezawa, F. *J. Chem. Phys.* **2000**, *113*, 9162–9168.

[104] Dodd, L. R.; Sandler, S. I. *Mol. Simul.* **1989**, *2*, 15–32.

[105] Errington, J. R.; Panagiotopoulos, A. Z. *J. Chem. Phys.* **1998**, *109*, 1093–1100.

[106] Vega, L.; Miguel, E. d.; Rull, L. F.; Jackson, G.; McLure, I. A. *J. Chem. Phys.* **1992**, *96*, 2296–2305.

[107] Freasier, B. C.; Woodward, C. E.; Bearman, R. J. *J. Chem. Phys.* **1997**, *106*, 10318–10328.

[108] Daub, C. D.; Camp, P. J.; Patey, G. N. *J. Chem. Phys.* **2004**, *121*, 8956–8959.

[109] Martin, M. G.; Zhuravlev, N. D.; Chen, B.; Carr, P. W.; Siepmann, J. I. *J. Phys. Chem. B* **1999**, *103*, 2977–2980.

[110] Cortés Morales, A. D.; Economou, I. G.; Peters, C. J.; Ilja Siepmann, J. *Mol. Simul.* **2013**, *39*, 1135–1142.

[111] Rowlinson, J. S.; Widom, B. *Molecular theory of capillarity*; Clarendon Press, 1982.

[112] Rowlinson, J. S.; Swinton, F. L. *Liquids and liquid mixtures*; Butterworth Scientific, 1982.

[113] Lemmon, E. W.; McLinden, M. O.; Friend, D. G. In *NIST Chemistry WebBook, NIST Standard Reference Database Number 69*; Linstrom, P. J., Mallard, W. G., Eds.; National Institute of Standards and Technology: Gaithersburg, MD, 2014.

[114] Ungerer, P.; Tavitian, B.; Boutin, A. *Applications of molecular simulation in the oil and gas industry: Monte Carlo methods*; Editions Technip: Paris, France, 2005.

[115] McQuarrie, D. A. *Statistical mechanics*; Harper & Row: New York, 1975.

[116] Bessières, D.; Piñeiro, M. M.; Ferron, G. D.; Plantier, F. *J. Chem. Phys.* **2010**, *133*, 074507.

[117] Vega, C.; McBride, C.; MacDowell, L. G. *J. Chem. Phys.* **2001**, *115*, 4203–4211.

[118] Galindo, A.; Vega, C.; Sanz, E.; MacDowell, L. G.; Miguel, E. d.; Blas, F. J. *J. Chem. Phys.* **2004**, *120*, 3957–3968.

[119] Yigzawe, T. M.; Sadus, R. J. *J. Chem. Phys.* **2013**, *138*, 194502.

[120] Mairhofer, J.; Sadus, R. J. *J. Chem. Phys.* **2013**, *139*, 154503.

[121] Piñeiro, M. M.; Cerdeiriña, C. A.; Medeiros, M. *J. Chem. Phys.* **2008**, *129*, 014511.

[122] Kortekaas, W. G.; Peters, C. J.; de Swaan Arons, J. *Fluid Phase Equilib.* **1997**, *139*, 205–218.

[123] Bolmatov, D.; Brazhkin, V. V.; Trachenko, K. *Nat Commun* **2013**, *4*.

[124] Bolmatov, D.; Brazhkin, V. V.; Fomin, Y. D.; Ryzhov, V. N.; Trachenko, K. *J. Chem. Phys.* **2013**, *139*, 234501.

[125] Ikushima, Y.; Hatakeda, K.; Saito, N.; Arai, M. *J. Chem. Phys.* **1998**, *108*, 5855–5860.

[126] Simeoni, G. G.; Bryk, T.; Gorelli, F. A.; Krisch, M.; Ruocco, G.; Santoro, M.; Scopigno, T. *Nat Phys* **2010**, *6*, 503–507.

[127] Johnson, J.; Zollweg, J.; Gubbins, K. *Mol. Phys.* **1993**, *78*, 591–618.

[128] Song, C. *Catalysis Today* **2002**, *77*, 17–49.

[129] Dresselhaus, M. S.; Thomas, I. L. *Nature* **2001**, *414*, 332–337.

[130] Voulgaris, M. E.; Peters, C. J.; de Swaan Arons, J. *Ind. Eng. Chem. Res.* **1998**, *37*, 1696–1706.

[131] Peters, C. J.; de Loos, T. W.; de Swaan Arons, J. *Fluid Phase Equilib.* **1991**, *70*, 185–197.

[132] Nasrifar, K.; Bolland, O.; Moshfeghian, M. *Energy Fuels* **2005**, *19*, 561–572.

[133] Smith, J.; Dawe, R. A.; Kydd, N. *Energ. Source Part A* **2007**, *29*, 511–527.

[134] Voulgaris, M. E.; Peters, C. J.; Arons, J. d. S. *Int. J. Thermophys.* **1995**, *16*, 629–642.

[135] Neubauer, B.; Tavitian, B.; Boutin, A.; Ungerer, P. *Fluid Phase Equilib.* **1999**, *161*, 45–62.

[136] DeSimone, J. M.; Guan, Z.; Elsbernd, C. S. *Science* **1992**, *257*, 945–947.

[137] Bendale, P. G.; Enick, R. M. *Fluid Phase Equilib.* **1994**, *94*, 227–253.

[138] Beckman, E. J. *J. Supercrit. Fluids* **2004**, *28*, 121–191.

[139] Raeissi, S.; Peters, C. J. *J. Phys. Chem. B* **2004**, *108*, 13771–13776.

[140] Raeissi, S.; Peters, C. J. *Fluid Phase Equilib.* **2001**, *191*, 33–40.

[141] Chen, R. J. J.; Chappelear, P. S.; Kobayashi, R. *J. Chem. Eng. Data* **1974**, *19*, 53–58.

[142] Chen, R. J. J.; Chappelear, P. S.; Kobayashi, R. *J. Chem. Eng. Data* **1974**, *19*, 58–61.

[143] Raeissi, S.; Peters, C. J. *J. Supercrit. Fluids* **2005**, *33*, 115–120.

[144] Martin, M. G.; Siepmann, J. I. *Theor. Chem. Acc.* **1998**, *99*, 347–350.

[145] Prausnitz, J. M.; Lichtenthaler, R. N.; Azevedo, E. G. d. *Molecular thermodynamics of fluid-phase equilibria*; Prentice Hall PTR: Upper Saddle River (N.J.), 1999.

[146] Henderson, D.; Leonard, P. J. *PNAS* **1970**, *67*, 1818–1823.

[147] Chapman, W. G.; Gubbins, K. E.; Jackson, G.; Radosz, M. *Fluid Phase Equilib.* **1989**, *52*, 31–38.

[148] Huang, S. H.; Radosz, M. *Ind. Eng. Chem. Res.* **1991**, *30*, 1994–2005.

[149] Michelsen, M. L. *Fluid Phase Equilib.* **1982**, *9*, 1–19.

[150] Michelsen, M. L. *Fluid Phase Equilib.* **1982**, *9*, 21–40.

[151] Raeissi, S.; Peters, C. J. *J. Chem. Thermodyn.* **2003**, *35*, 573–581.

[152] Aparicio-Martínez, S.; Hall, K. R. *Ind. Eng. Chem. Res.* **2007**, *46*, 273–284.

[153] Alfradique, M. F.; Castier, M. *Fluid Phase Equilib.* **2005**, *230*, 1–8.

[154] Jessen, K.; Kovscek, A. R.; Orr Jr., F. M. *Energy Convers. Manage.* **2005**, *46*, 293–311.

[155] Blunt, M.; Fayers, F. J.; Orr Jr., F. M. *Energy Convers. Manage.* **1993**, *34*, 1197–1204.

[156] Raeissi, S.; Peters, C. J. *J. Supercrit. Fluids* **2002**, *22*, 93–102.

[157] Leekumjorn, S.; Krejbjerg, K. *Fluid Phase Equilib.* **2013**, *359*, 17–23.

[158] Rovetto, L. J.; Peters, C. J.; Brignole, E. A. *J. Supercrit. Fluids* **2005**, *34*, 183–187.

[159] Raeissi, S.; Peters, C. J. *J. Supercrit. Fluids* **2001**, *20*, 221–228.

[160] Potoff, J. J.; Siepmann, J. I. *AIChE J.* **2001**, *47*, 1676–1682.

[161] Rai, N.; Siepmann, J. I. *J. Phys. Chem. B* **2007**, *111*, 10790–10799.

[162] Maerzke, K. A. Monte Carlo Simulations of Fluids: Microheterogeneity and Electric Field Effects. Ph.D. thesis, University of Minnesota, Minneapolis, MN, USA, 2010.

[163] Zhang, L.; Siepmann, J. I. *J. Phys. Chem. B* **2005**, *109*, 2911–2919.

[164] Gross, J.; Sadowski, G. *Ind. Eng. Chem. Res.* **2002**, *41*, 5510–5515.

[165] Henderson, D.; Leonard, P. J. *PNAS* **1971**, *68*, 632–635.

[166] Lay, E. N. *J. Chem. Eng. Data* **2010**, *55*, 223–227.

[167] Kaminishi, G.-I.; Yokoyama, C.; Shinji, T. *Fluid Phase Equilib.* **1987**, *34*, 83–99.

[168] Cui, S. T.; Cochran, H. D.; Cummings, P. T. *J. Phys. Chem. B* **1999**, *103*, 4485–4491.

[169] Oliveira, M. B.; Queimada, A. J.; Kontogeorgis, G. M.; Coutinho, J. A. *J. Supercrit. Fluids* **2011**, *55*, 876–892.

[170] Button, J. K.; Gubbins, K. E. *Fluid Phase Equilib.* **1999**, *158–160*, 175–181.

[171] Cataño-Barrera, A. M.; Figueira, F. L.; Olivera-Fuentes, C.; Colina, C. M. *Fluid Phase Equilib.* **2011**, *311*, 45–53.

[172] Maerzke, K. A.; Siepmann, J. I. *J. Phys. Chem. B* **2011**, *115*, 3452–3465.

[173] Dullien, F. A. L. *Porous Media: Fluid Transport and Pore Structure*; Academic Press, 1991.

[174] Bijeljic, B.; H. Muggeridge, A.; J. Blunt, M. *Chem. Eng. Sci.* **2003**, *58*, 2377–2388.

[175] Chapoy, A.; Mohammadi, A. H.; Chareton, A.; Tohidi, B.; Richon, D. *Ind. Eng. Chem. Res.* **2004**, *43*, 1794–1802.

[176] Godec, M. L.; Kuuskraa, V. A.; Dipietro, P. *Energy Fuels* **2013**, *27*, 4183–4189.

[177] Shaker Shiran, B.; Skauge, A. *Energy Fuels* **2013**, *27*, 1223–1235.

[178] Alagic, E.; Skauge, A. *Energy Fuels* **2010**, *24*, 3551–3559.

[179] Johannessen, A. M.; Spildo, K. *Energy Fuels* **2013**, *27*, 5738–5749.

[180] Lebedeva, N. N.; Mazaev, V. V.; Tret'yakov, N. Y. *Russ. J. Appl. Chem.* **2001**, *74*, 1415–1417.

[181] Browarzik, C.; Browarzik, D.; Winkelmann, J. *Fluid Phase Equilib.* **2007**, *261*, 238–247.

[182] Kahlweit, M.; Lessner, E.; Strey, R. *J. Phys. Chem.* **1983**, *87*, 5032–5040.

[183] Knickerbocker, B. M.; Pesheck, C. V.; Scriven, L. E.; Davis, H. T. *J. Phys. Chem.* **1979**, *83*, 1984–1990.

[184] Rudolph, E. S. J.; Caçao Pedroso, M. A.; Swaan Arons, J. d. *J. Phys. Chem. B* **1997**, *101*, 3914–3918.

[185] Kleinert, H. *J. Chem. Phys.* **1986**, *84*, 964–967.

[186] Kahlweit, M. et al. *J. Colloid Interface Sci.* **1987**, *118*, 436–453.

[187] Lade, O.; Beizai, K.; Sottmann, T.; Strey, R. *Langmuir* **2000**, *16*, 4122–4130.

[188] Kahlweit, M.; Strey, R. *Angew. Chem. Int. Ed. Engl.* **1985**, *24*, 654–668.

[189] Lee, J.-M.; Lim, K.-H. *Colloid Surface A* **2004**, *248*, 57–65.

[190] Kleinert, H. *J. Chem. Phys.* **1986**, *85*, 4148–4152.

[191] Abrams, D. S.; Prausnitz, J. M. *AIChE J.* **1975**, *21*, 116–128.

[192] Rudolph, E. S. J.; Langeveld, J. H.; de Loos, T. W.; de Swaan Arons, J. *Fluid Phase Equilib.* **2000**, *173*, 81–96.

[193] Papaioannou, V.; Lafitte, T.; Avendaño, C.; Adjiman, C. S.; Jackson, G.; Müller, E. A.; Galindo, A. *J. Chem. Phys.* **2014**, *140*, 054107.

[194] Garrido, N. M.; Folas, G. K.; Kontogeorgis, G. M. *Fluid Phase Equilib.* **2008**, *273*, 11–20.

[195] Reschke, T.; Brandenbusch, C.; Sadowski, G. *Fluid Phase Equilib.* **2014**, *368*, 91–103.

[196] Avlund, A. S.; Kontogeorgis, G. M.; Michelsen, M. L. *Ind. Eng. Chem. Res.* **2012**, *51*, 547–555.

[197] Avlund, A. S.; Kontogeorgis, G. M.; Chapman, W. G. *Mol. Phys.* **2011**, *109*, 1759–1769.

[198] Bai, P.; Siepmann, J. I. *Fluid Phase Equilib.* **2011**, *310*, 11–18.

[199] Keasler, S. J.; Bai, P.; Tsapatsis, M.; Siepmann, J. I. *Fluid Phase Equilib.* **2014**, *362*, 118–124.

[200] Chen, B.; Siepmann, J. I. *J. Phys. Chem. B* **2006**, *110*, 3555–3563.

[201] Stubbs, J. M.; Potoff, J. J.; Siepmann, J. I. *J. Phys. Chem. B* **2004**, *108*, 17596–17605.

[202] Martin, M. G.; Siepmann, J. I. *J. Am. Chem. Soc.* **1997**, *119*, 8921–8924.

[203] Negahban, S.; Willhite, G. P.; Walas, S. M.; Michnick, M. J. *Fluid Phase Equilib.* **1986**, *32*, 49–61.

[204] Moodley, S.; Bolton, K.; Ramjugernath, D. *Fluid Phase Equilib.* **2010**, *299*, 24–31.

[205] Moodley, S.; Johansson, E.; Bolton, K.; Ramjugernath, D. *Mol. Simul.* **2010**, *36*, 758–762.

[206] Lasich, M.; Johansson, E. L.; Ramjugernath, D. *Fluid Phase Equilib.* **2014**, *368*, 65–71.

[207] Voorhees, P. W. *J. Stat. Phys.* **1985**, *38*, 231–252.

[208] Taylor, P. *Adv. Colloid Interfac.* **1998**, *75*, 107–163.

Appendix A

Supporting Information for Chapter 3

This appendix provides supporting information for simulations results that were used to verify the behavior of SW and TAN-Linear models described in Chapter 3. The results in Figure A.6 show the dependence of $C_{V,\mathrm{res}}$ predictions on the attractive well range for square well fluids at the same reduced temperature. Additionally, the evolution of order parameters S over the length of a simulation are provided for TAN-Linear models at two different densities, showing that these values oscillate around a value of 0 with respect to the angle between average 1-4 vectors in molecules and x, y, and z axes. This indicates that isotropic behavior is obtained throughout the length of each simulation, and this result is supported by symmetric histograms for angular distributions for all densities. Data for TAN-Linear model obtained from NpT simulations at $T = 467.5$ K.

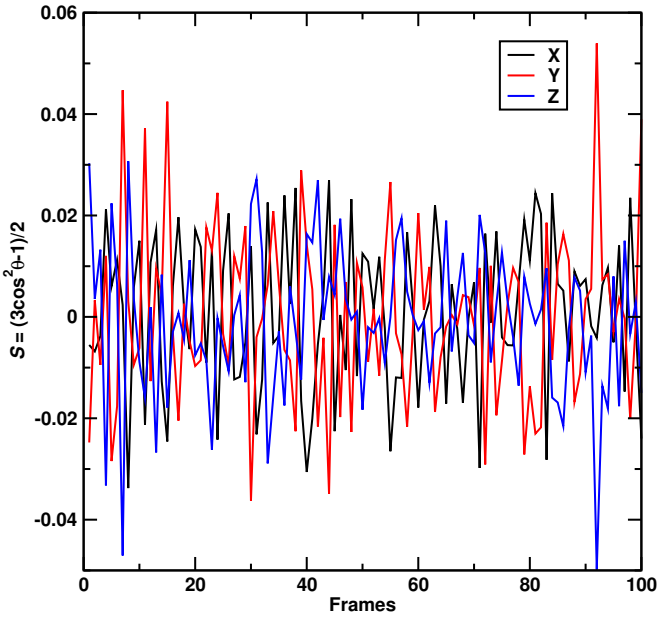

Figure A.1: Evolution of order parameter for TAN-Linear model at $\rho_{\mathrm{r}} = 1.00$.

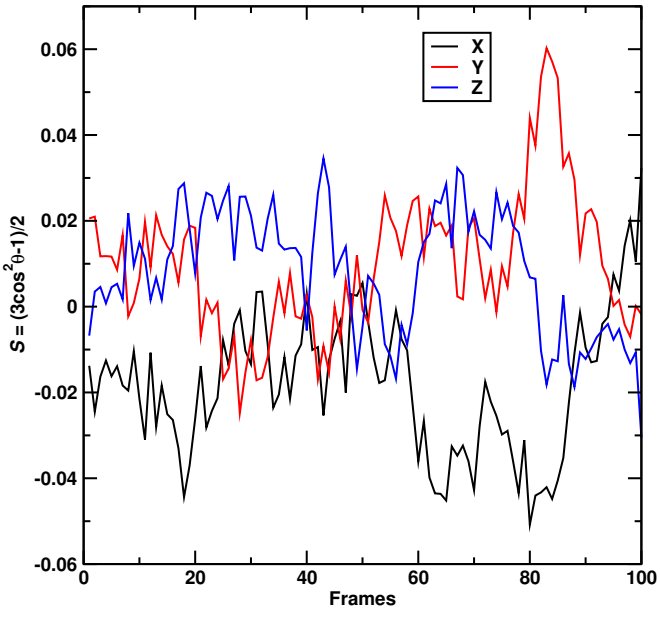

Figure A.2: Evolution of order parameter for TAN-Linear model at $\rho_{\mathrm{r}} = 3.00$.

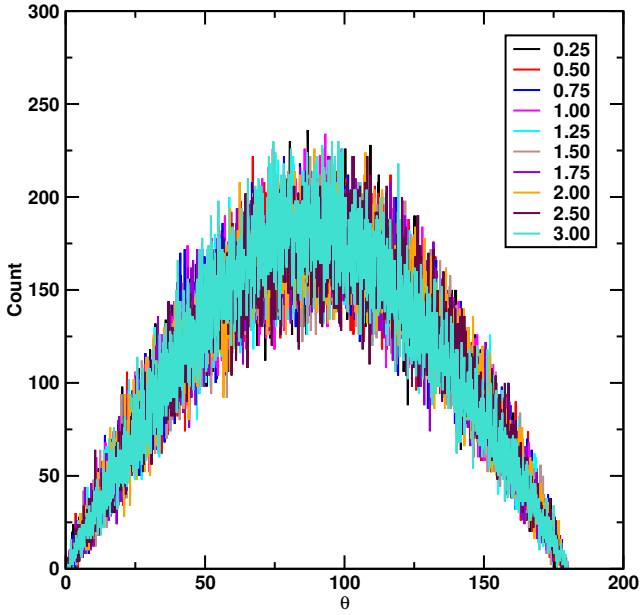

Figure A.3: Angular distribution of 1-4 vectors with respect to the x-axis for TAN-Linear model at densities between $\rho_{\mathrm{r}} = 0.25$ and $\rho_{\mathrm{r}} = 3.00$.

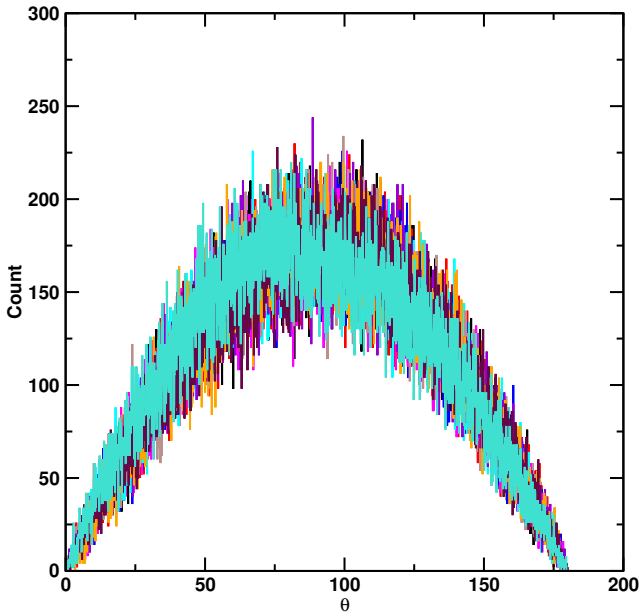

Figure A.4: Angular distribution of 1-4 vectors with respect to the y-axis for TAN-Linear model at densities between $\rho_{\mathrm{r}} = 0.25$ and $\rho_{\mathrm{r}} = 3.00$. Color scheme defined in Figure A.3.

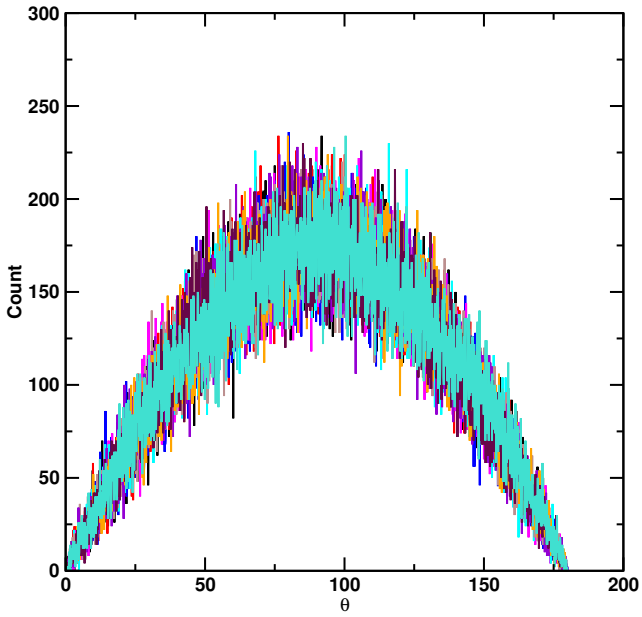

Figure A.5: Angular distribution of 1-4 vectors with respect to the z-axis for TAN-Linear model at densities between $\rho_{\mathrm{r}} = 0.25$ and $\rho_{\mathrm{r}} = 3.00$. Color scheme defined in Figure A.3.

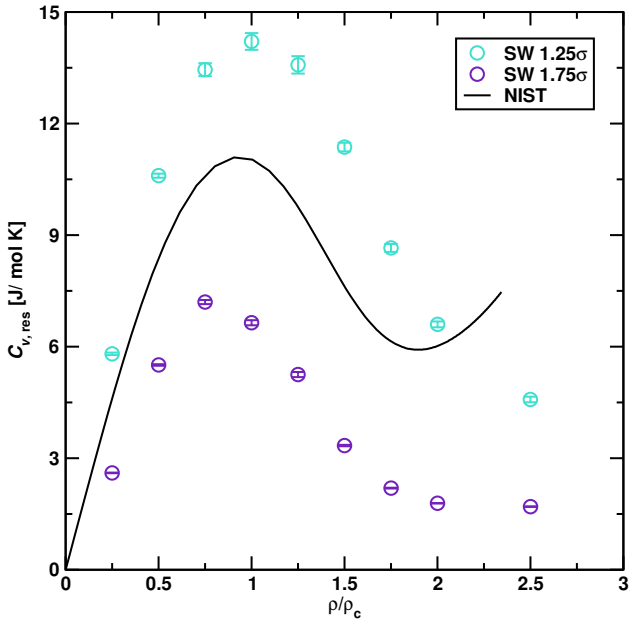

Figure A.6: Residual isochoric heat capacities as a function of reduced density at $T_{\mathrm{r}} = 1.1$ for square well fluids of variable range. For both models, $\sigma = 5.42$ Å and $\epsilon = 532.00$ K.